Resonant interaction of fast particles with Alfvén waves in spherical tokamaks

Matthew Keith Lilley

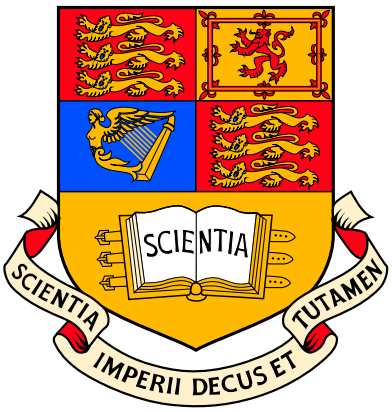

February 2009

Submitted in partial fulfillment of the requirements for the degree of Doctor of Philosophy of Imperial College London.

Department of Physics
Imperial College London
Prince Consort Road
London SW7 2AZ

The role of the author

This thesis combines both theoretical and experimental efforts. The author has extended existing theories, which are clearly cited in this thesis, and has also developed new theories in collaboration with S. E. Sharapov and B. N. Breizman. The experimental studies were performed in collaboration with experimental physicists on the MAST and LAPD machines. The author was responsible, in the MAST case, for proposing and planning the experiments, but not for running the machine or the diagnostics. Analysis of the MAST magnetic data was performed using an existing tool developed by S. D. Pinches. Kinetic simulations were performed using the existing TRANSP Monte Carlo code, which was operated by collaborators at PPPL. For LAPD, the author was responsible for proposing experiments and was also involved in setting up the experimental diagnostics. Subsequent analysis of the data was performed using an existing tool developed by Y. Zhang.

Declaration

I hearby certify that the material of this thesis, which I now submit for the award of Doctor of Philosophy, is entirely my own work unless otherwise cited or acknowledged within the body of the text.

Signed,

Matthew Lilley

19th February 2009

Abstract

The Spherical Tokamak (ST) concept has become one of the main avenues in magnetic nuclear fusion research since STs successfully demonstrated plasma operation at $\beta = 2P\mu_0/B^2 \sim 1$. Next step ST machines aiming at achieving burning plasma conditions in high β plasmas are being planned, such as the Spherical Tokamak Power Plant (STPP) and the Component Testing Facility (CTF). Instabilities of fast particle-driven Alfvén eigenmodes are often observed in present-day STs. Such instabilities, driven by fusion-born alpha particles as well as by fast ions produced with auxiliary heating schemes, in the next step STs may pose a major problem as these instabilities may affect confinement and losses of the fast ions.

A theory of compressional Alfvén eigenmodes (CAE) with frequencies above the deuterium cyclotron frequency, $\omega > \omega_{cD}$, is developed for plasma parameters of a STPP, and modes in the ion-ion hybrid frequency range, $\omega_{cT} < \omega < \omega_{cD}$, are also investigated in order to assess the potential of diagnosing the deuterium-tritium (D-T) ratio. For the 1-D character of a STPP equilibrium with $\beta \sim 1$, a 'hollow cylinder' toroidal plasma model is employed for studying CAEs with arbitrary values of the parallel wave-vector $k_{\|} = \mathbf{k} \cdot \mathbf{B}/\left|\mathbf{B}\right|$. The existence of weakly-damped CAEs, free of mode conversion, is shown to be associated with the 'well' in the magnetic field profile, $B = B\left(R\right)$, that can exist at the magnetic axis.

A significant part of this thesis focusses on the experimentally observed effects of resonant wave-particle interaction between Alfvén waves and fast particles in the Mega Amp Spherical Tokamak (MAST) device at the Culham Laboratory, UK, and in the LArge Plasma Device (LAPD) in the University of California, Los-Angeles, USA. New robust experimental scenarios for exciting CAEs in the MAST spherical

tokamak are developed, and interpretation of the observed CAEs in the frequency range $\omega_{cD}/3 < \omega < \omega_{cD}$ is given in the context of the 1-D ST model and the Doppler shifted cyclotron resonance. The efficiency of the Doppler resonance between co and counter directed fast ions and left and right hand polarised Alfvén waves is further assessed experimentally on the LAPD device, with probe ions injected in the presence of Alfvén waves launched by an external antenna.

The developed theory of CAEs is then applied to a calculation of the linear kinetic drive of CAEs in the MAST experiments. A model representation of the fast ion distribution function, produced by neutral beam injection (NBI), is used by fitting to the TRANSP Monte-Carlo NBI modelling results. The main free energy sources associated with temperature anisotropy and bump-on-tail are estimated analytically, and the CAE stability boundary is qualitatively assessed.

In order to explain the experimentally observed difference between steady-state and pulsating Alfvénic modes, the non-linear theory of fast particle driven modes near marginal stability is extended to include dynamical friction (drag). For the bump-on-tail problem, the drag is shown to always give an explosive amplitude evolution in contrast to diffusion in velocity space in the vicinity of the wave-particle resonance. This is then extended to the case of experimentally observed NBI-driven toroidal Alfvén eigenmodes (TAEs) in the MAST machine. The experimentally observed differences between TAEs driven by fast ions produced with ion cyclotron resonance heating (ICRH) and NBI are then interpreted. The problem of drag dominated collisions for modes excited by fusion-born alpha particles in burning plasmas such as a STPP and ITER is underlined.

Acknowledgements

The path of a PhD is not straightforward. There are many bends in the road and obstacles to pass, and without guidance and support one can easily lose their way. My supervisor, Sergei Sharapov, has been a constant source of encouragement and a great mentor throughout the course of my PhD. Simultaneous interest in fundamental physics and the future of fusion energy has been an inspiration. Steve Cowley, Tim Hender, Mikhail Gryaznevich, Simon Pinches and Michael Coppins have also played an important role in my professional development. Their interest in my research as well as their stimulating discussions have helped to shape me into the physicist I am today. Thanks must also go to the MAST team, without whom my research could not have been performed.

Without communication and collaboration science can never advance. I have had the great opportunity to collaborate internationally with world leaders in the field of fast particles in plasmas over the course of my PhD. Exposure to fundamental physics experiments with Bill Heidbrink has helped to remind me that the theories we develop can and should be be scrutinised experimentally. My time in Austin with Boris Breizman was short, but truly inspirational. Our continual contact over the past year has been both fruitful and extremely educational. It has reignited my passion for theoretical physics and taught me that, although there is still so much left to learn, an understanding is within our grasp.

The influence of my mother and father can never be understated. Without their unquestioning support and unwavering belief in me I could not be where I am today. My sister has been a shining beacon of light for me, continuing to remind me of my goal 'To make a difference' and lighting the way even in the dark. Finally the support

of Nuno Vieira has, without a doubt, kept me true to myself and encouraged me to persue my physics dream even in a climate of financial temptation.

Symbol	Definition
D	Deuterium species label
T	Tritium species label
STPP	Spherical tokamak power plant
ST	Spherical tokamak
ICRH	Ion cyclotorn resonance heating
NBI	Neutral beam injection
EM	Electromagnetic
TAE	Toroidal Alfvén eigenmode
LAPD	Large plasma device
MAST	Mega amp spherical tokamak
SAW/SAE	Shear Alfvén wave/eigenmode
CAW/CAE	Compressional Alfvén wave/eigenmode
FLR	Finite Larmor radius
n_s	Density of species s
T_s	Temperature of species s
τ_E	Energy confinement time
P	Thermal pressure
B	Magnetic field
B_0	Equilibrium magnetic field
δB	Perturbed magnetic field
I_p	Plasma current
β	Plasma beta
ϕ	Toroidal angle
θ	Polodal angle
R	Major radial co-ordinate
R_0	Major radius

Symbol	Definition
r	Minor radial co-ordinate
a	Minor radius
z	Vertical coordinate
q	Safety factor
v_{A}	Alfvén speed
ω	Angular frequency
$k_{\parallel}$	Parallel wave vector
ω_{cs}	Angular cyclotron frequency of species s
ω_{ps}	Angular plasma frequency of species s
E	Perturbed electric field
ε	Dielectric tensor
σ	Conductivity tensor
$v_{\mathrm{T}s}$	Thermal speed of species s
κ_s	Ratio of the density of species s to the electron density
$N_{\parallel}$	Parallel refractive index
$N_{\perp}$	Perpendicular refractive index
ρ_s	Larmor radius of species s
n	Toroidal mode number
F	Distribution function
γ_l	Linear growth rate
γ_d	Linear damping rate
α	Drag collision frequency
ν	Diffusion collision frequency
β	Krook collision frequency

Contents

List of Figures

List of Tables

Chapter 1

Introduction

1.1 Fusion

The fusion of light elements into heavier ones with the subsequent release of energy is one of the avenues being explored for the production of environmentally friendly energy. The abundance of fusion fuel (deuterium from sea water and tritium bred from lithium), capable of lasting millions of years, makes fusion energy an attractive solution to the current 'energy crisis'. Fusion science encompasses many disciplines from basic plasma physics to material science, all of which are important for ensuring the success of future devices such as ITER and DEMO. Economic fusion energy requires fuel temperatures to be about 10^8K (hotter than the centre of the sun). At these temperatures the fuel is a plasma, which can be confined using magnetic fields, and the most promising and developed device to date is the tokamak [1], which holds the plasma in the shape of a torus.

The fusion of deuterium and tritium is the easiest as can be seen from the fusion reaction cross sections shown in Fig 1.1.

$$ {}^{2}_{1}\mathrm{D} + {}^{3}_{1}\mathrm{T} \rightarrow {}^{4}_{2}\mathrm{He} + {}^{1}_{0}\mathrm{n} \tag{1.1} $$

The highest probability of fusion occurs for plasma temperatures of around $T = 10 - 20$keV and at these temperatures the requirement for ignition, i.e energy loss balanced by heating from the fusion-born α particles with and energy of 3.5MeV,

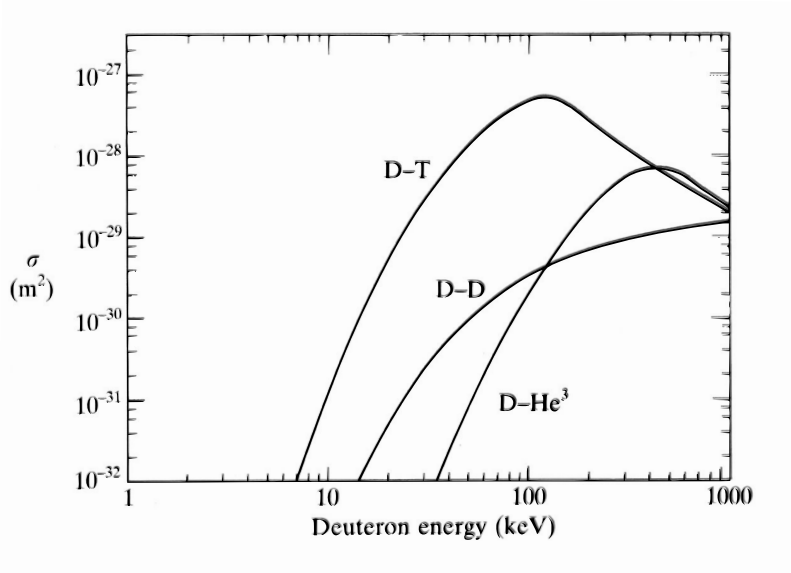

Figure 1.1: *Cross-section for important fusion reactions [1]. The higher the curve the more desirable the reaction is for a fusion reactor.*

can be expressed as [1]

$$n_i T_i \tau_E \geq 5 \times 10^{21} m^{-3} \text{keVs} \sim 10\text{atms} \tag{1.2}$$

where n_i is the ion density, T_i is the ion temperature and τ_E is the energy confinement time (energy in the plasma / loss rate).

1.1.1 Magnetic confinement

For a plasma confined in a magnetic field there is a limit to the amount of pressure P that can be sustained for a given magnetic field B, i.e a limit on the plasma $\beta = 2P\mu_0/B^2$ [2]. In the magnetic fusion case the ignition criterion can be re-expressed as

$$\beta \tau_E B^2 \geq 4\text{T}^2\text{s}. \tag{1.3}$$

It can then be seen that ignition can be achieved in the following ways

- Increasing the limit of β, by optimising the magnetic topology of the system so that a higher pressure can be supported for the same magnetic field.
- Increasing the confinement time τ_E keeping the energy inside the plasma for longer.

- Increasing the magnetic field B, allowing a higher pressure to be achieved for the same value of β.

The spherical tokamak is designed to take advantage of the first of these optimisation regimes. The second concept will be pursued in ITER, where increasing τ_E necessitates a larger plasma volume and hence a larger reactor. The final route for magnetic confinement fusion is being pursued in ALCATOR C-MOD.

A tokamak device confines a plasma in a closed toroidal configuration using magnetic fields to restrict the flow of charged particles towards the material walls. In order to obtain an equilibrium, the magnetic field is composed of a toroidal (ϕ) part B_ϕ, that is provided by coils wrapped around the torus, and a poloidal (θ) part B_θ, that is created by driving a current through the plasma. A schematic of the tokamak geometry is displayed in Fig 1.2.

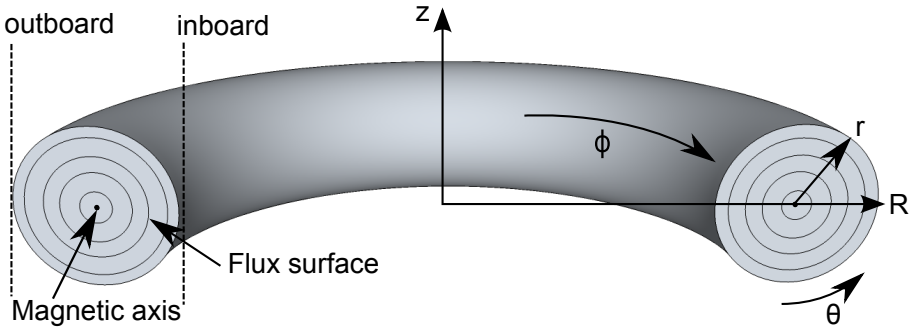

Figure 1.2: *Schematic of the geometry of a tokamak. ϕ is the toroidal direction, θ is the poloidal direction.*

Helical magnetic field lines result from the combined magnetic fields B_ϕ and B_θ and the degree of helicity is measured by the 'safety factor' q

$$q = \frac{1}{2\pi} \oint \frac{1}{R} \frac{B_\phi}{B_\theta} dl,$$

where the integral is taken over a closed loop in the poloidal plane ($\phi = \text{const.}$). q essentially gives the number of toroidal passes the field line makes before returning to the same poloidal position. Rational values of q describe field lines that eventually join back on themselves and are closed.

1.1.2 The spherical tokamak

A spherical tokamak (ST) is a low aspect ratio (or tight aspect ratio) tokamak as shown in Fig 1.3.

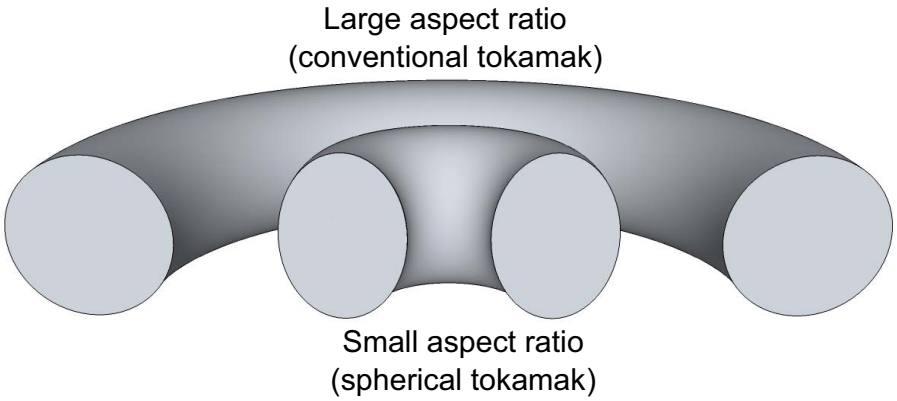

Figure 1.3: *Comparison of the geometries of conventional and spherical tokamaks*

The primary motivation for the ST concept was its predicted high β limit [3]. Results from START [4], MAST [5], NSTX [6] and other spherical tokamaks have demonstrated many advantages of the tight-aspect ratio concept,

- Higher β can be achieved without destabilising the plasma, a record volume averaged β of 40% was achieved on START at Culham [4].
- A ST has a more compact design, and so with a smaller surface area there is a higher flux of neutrons through the surface of the tokamak. As such a ST is a good candidate for a CTF (Component Test Facility) for neutron fluence testing.
- ST plasmas are naturally elongated, which means they can support a higher current allowing increased confinement [1].
- The ratio of the magnetic field at the inboard to outboard side of the plasma is higher in a ST than a conventional tokamak. This increases the amount of 'good curvature' of the field lines, which provides stability against magneto-hydrodynamics (MHD) modes [1].

The successful demonstration of the advantages of the tight-aspect ratio configuration has given rise to the Spherical Tokamak Power Plant (STPP) concept [7] (Fig 1.4) and to the question of how the current STs can provide knowledge that will be relevant for future burning STs.

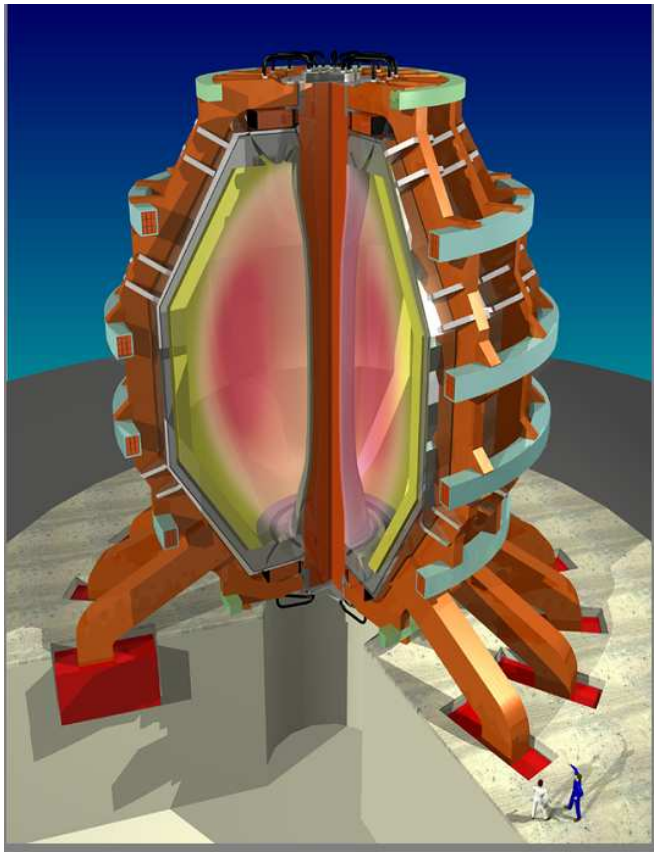

Figure 1.4: *Perspective view of a spherical tokamak power plant (STPP) design [8]*

1.2 Fast particle driven instabilities

Energetic (also called fast) particles are abundant in modern tokamak devices [9]. The efficiency of ohmic heating from the plasma current reduces at high temper-

atures [1] and so auxiliary heating schemes, such as neutral beam injection (NBI) and ion cyclotron resonance heating (ICRH), are required to achieve ignition. The non-thermal ions produced by NBI and ICRH, as well as those born in fusion reactions, can however resonantly interact with normal electromagnetic (EM) modes of the plasma, exciting so called fast particle driven instabilities. EM instabilities are often excited in present day STs, driven by fast ions produced by NBI with $v_{\mathrm{NBI}} > v_{\mathrm{A}}$ (here v_{NBI} is the velocity of the beam, $v_{\mathrm{A}} = B_0/\sqrt{\mu_0 m_i n_i}$ is the Alfvén speed, B_0 and $m_i n_i$ are the equilibrium magnetic field and plasma mass density respectively) [10, 11].

In a STPP there will be a significant population of alpha particles, born in deuterium - tritium (D-T) fusion reactions at an energy of 3.52MeV, which could drive EM instabilities. Because of the high β in a STPP, these fast particle driven EM instabilities will differ significantly from fusion power plants derived from conventional tokamaks with typical inverse aspect ratio $a/R \approx 0.3$ and $\beta \approx 1 - 5\%$, in which instabilities in the Alfvén frequency range (e.g. Toroidal Alfvén Eigenmodes - TAEs with $\omega = v_{\mathrm{A}}/2Rq$) are considered to be most dangerous. More specifically for $\beta \approx 1$ (valid in the plasma core of a STPP) EM instabilities in the Alfvén frequency range will be strongly damped by interaction with thermal ions via Landau resonance $\left(v_A \approx v_{\|i}\right)$, where $v_{\|i} = \mathbf{v_i} \cdot \mathbf{B_0}/|\mathbf{B_0}|$ is the parallel velocity of the thermal ions. On the other hand instabilities of higher frequency ω comparable to the ion cyclotron frequency ω_{ci}, excited via cyclotron resonances, $\omega = k_{\|} v_{\|\alpha} - l\omega_{c\alpha}$ (here $k_{\|} = \mathbf{k} \cdot \mathbf{B_0}/|\mathbf{B_0}|$ and l is an integer), will be relevant. These instabilities may involve compressional Alfvén eigenmodes [12], shear Alfvén eigenmodes with finite ratio ω/ω_{ci}, and ion-ion hybrid eigenmodes [13]. They may be driven by free energy sources associated with gradients in velocity space of the α particle distribution function, and cause non-classical relaxation of the α particles in velocity space.

The diagnostic potential of fast particle driven instabilities has also been noted [14]. The perturbed magnetic field is measured externally and internal plasma conditions are inferred, so called MHD spectroscopy. For power plant scenarios this remote sensing capability will be crucial, as active probing will be made impossible due to the extreme conditions of a burning plasma.

1.3 Thesis overview

CHAPTER 2 The response of a plasma to perturbations is that of a dielectric medium which, in a magnetised plasma, is characterised by a dielectric tensor ε. A plasma responds resonantly to specific perturbations, so called normal modes or eigenmodes, which refer to solutions of a wave equation satisfying boundary conditions in the geometry of interest. In the case of an infinite homogeneous plasma the eigenmodes take the form of plane waves, however in an inhomogeneous plasma in toroidal geometry, such as that of a ST, the solutions usually take the form of a discrete spectrum. In general a set of three coupled partial differential equations of second order must be solved for the perturbed electric field $\mathbf{E}$ (Eq 1.4), which is a difficult task to analyse both analytically and numerically for an arbitrary plasma cross section and plasma parameters.

$$\nabla \times \nabla \times \mathbf{E} = \frac{\omega^2}{c^2}\varepsilon\mathbf{E} \tag{1.4}$$

Previous work investigated modes driven via the drift resonance condition $\omega - k_\perp v_{Db} - \omega_{cb} = 0$, where $\omega_{Db} \equiv k_\perp v_{Db}$ is the drift frequency of the fast ions. In this case the role of a significant $k_\parallel$ was unimportant, which allowed a 2-D wave model to be employed for studying compressional Alfvén eigenmdes [15]. For the high frequency eigenmodes, $\omega \sim \omega_{ci}$, of interest to this thesis, the Doppler shifted cyclotron resonances $\omega - k_\parallel v_{\parallel b} \mp \omega_{cb} = 0$ play an important role and so the effects of both non-zero ω/ω_{ci} and non-zero $k_\parallel$ are crucial, which complicates the analysis. It is possible however to reduce the complexity of the problem in some cases, namely high β plasmas and highly elliptical plasmas, and it is with this in mind that we employ a 1-D wave equation for the study of waves in the high β plasma of a Spherical Tokamak Power Plant (STPP) and the highly elliptical MAST tokamak plasma.

For a STPP operating in deuterium-tritium (D-T) a discrete spectrum of EM modes with frequencies above the deuterium ion cyclotron frequency $\omega > \omega_{cD}$ (compressional Alfvén eigenmodes) and with frequencies between the tritium and deuterium cyclotron frequencies $\omega_{cT} < \omega < \omega_{cD}$ (ion-ion hybrid eigenmodes) is found. The wave propagation in a multiple ion species plasma is significantly different from that of a single ion species plasma and investigation into this fact leads to the pro-

posal of using the discrete spectrum as a diagnostic for the D-T mixture ratio, which should not deviate from 50:50 in a power plant scenario. This research was published in Physics of Plasmas [16]

CHATPER 3 Since many aspects of plasma instabilities depend on the existence and character of wave particle resonances, the subject warrants a more complete experimental investigation. Of particular interest for this thesis is the role that the electric field polarisation and wave propagation direction have in the wave particle interaction. A device of particular significance in the field of fundamental wave particle interactions is the LArge Plasma Device (LAPD) [17] at the University of California, Los Angeles (UCLA). LAPD is a large cylindrical device with a turnover time of 1s between pulses. This high rep rate enables LAPD to acquire large data sets over which averaging can be performed to obtain very robust measurements. The resonant interaction of Alfvén waves with energetic particles via the Doppler shifted cyclotron resonances (Eq 1.5 and Fig 1.5) is investigated in the simplified cylindrical geometry of LAPD.

$$\omega - k_{\|} v_{\|b} \mp \omega_{cb} = 0 \tag{1.5}$$

Experimental confirmation that right hand polarised EM waves do not interact

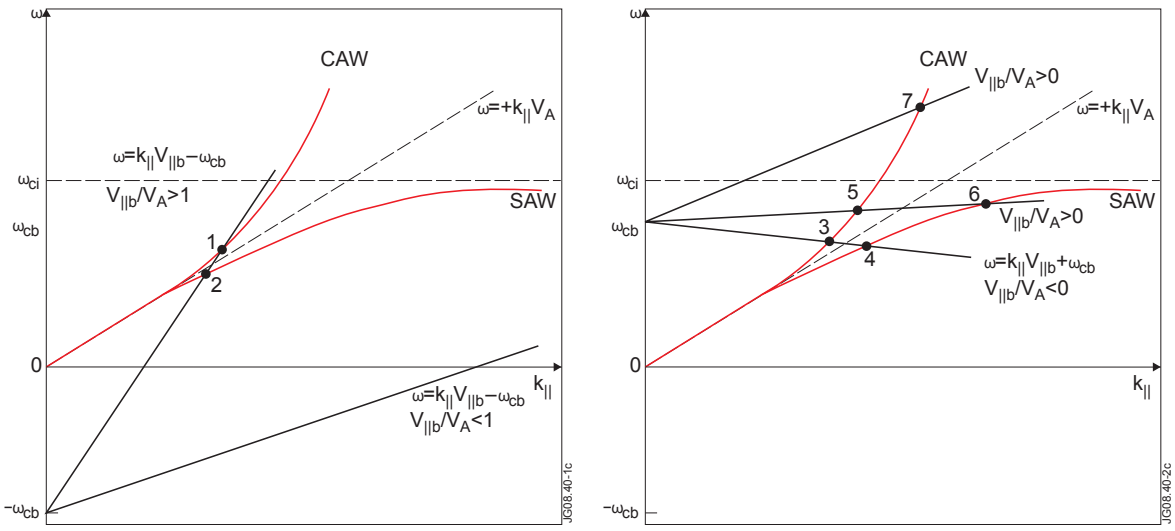

Figure 1.5: *Dispersion relation for Alfvén waves in an infinite homogeneous plasma with the anomalous Doppler (left) and Doppler (right) shifted cyclotron resonance condition superposed.*

significantly with left hand gyrating ions via this wave particle resonance is found. It is also confirmed that counter propagating left hand polarised waves and ions can interact via this resonance, a fact that has significance in current ST machines like MAST, where energetic particles are observed to excite counter propagating waves at frequencies comparable to the ion cyclotron frequency. This research has been presented at the American Physical Society Conference and has been submitted as an invited paper to Physics of Plasmas (Dec 2008).

CHAPTER 4 High frequency modes driven by NBI ions have been previously observed on NSTX and MAST, and were interpreted to be CAEs [12]. The Beam driven modes were occasionally observed on MAST [18], however a complete investigation was not performed. One of the aims of this this work was to develop a robust experimental scenario for studying high frequency modes on MAST. High frequency modes with frequencies up to $\approx \omega_{cD}$ are excited close to the stability threshold on MAST in the presence of highly energetic ions injected through the NBI system (Fig 1.6).

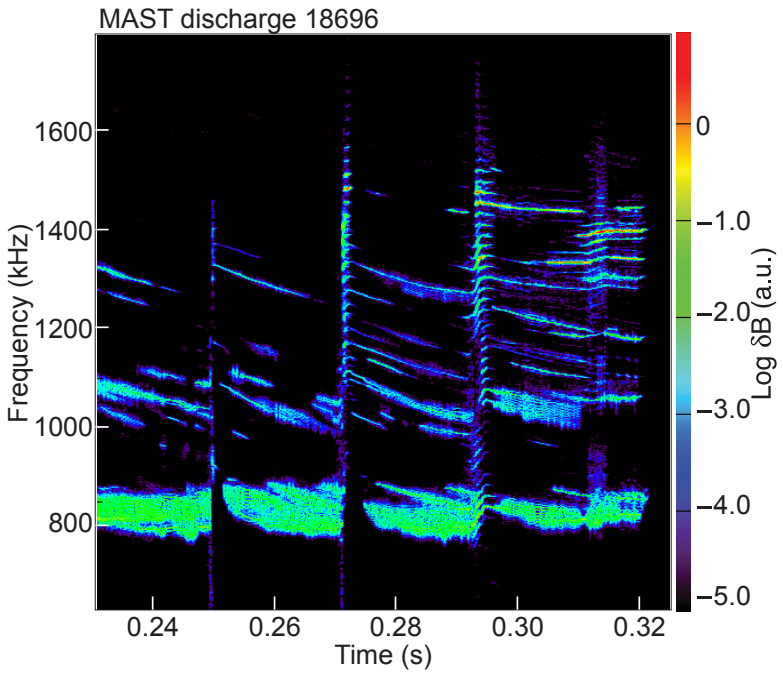

Figure 1.6: *New MAST experimental scenario for studying high frequency modes.*

The modes are almost always seen to propagate counter to the injected ions. The inaccessibility of the anomalous Doppler shifted cyclotron resonance, responsible

for co-propagating modes interacting with super Alfvénic ions in MAST, has been proposed as an explanation for this behaviour. The 1-D model used for the STPP case is applied to MAST plasmas and confirms the compressional nature of the modes and attempts to explain the wide variety of the high frequency activity observed. The experimental work was published in Nuclear Fusion [19].

CHAPTER 5 The excitation of normal modes of a system requires a source of free energy to 'drive' the modes and a resonance to enable the energy to 'flow' into the wave. In the case of modes excited by energetic particles, this free energy arises due to the non thermal component of the distribution function F, provided by the fast particles. For the high frequency compressional instabilities observed on MAST, which are excited via the Doppler shifted cyclotron resonance, the relevant free energy source comes from the gradients of the distribution function in velocity space [20]. A kinetic treatment of the linear drive of these instabilities is therefore required.

Simulations of the fast particle distribution function reveal bump like structures in velocity space corresponding to 3 beam injections energies $E, E/2, E/3$ (Fig 1.7).

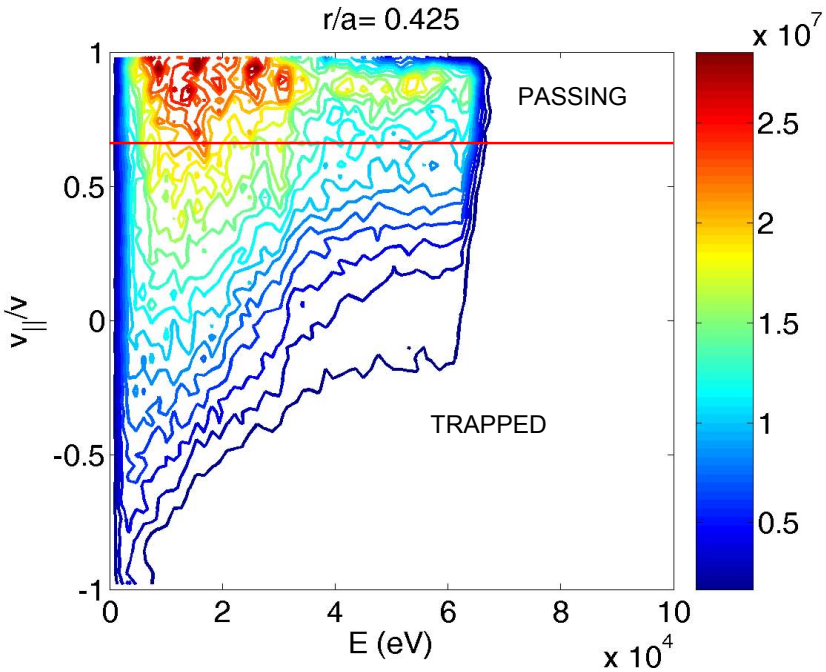

Figure 1.7: *Contours of F_{NBI} as a function of energy and pitch angle averaged over the poloidal angle. The red line shows the trapped passing boundary*

The distribution function is modelled using a Gaussian profile which reveals temperature anisotropy and beam speed are the factors determining the drive. Calculation of the drive for an experimentally observed mode reveals high levels of sensitivity to the assumed distribution function, suggesting high resolution simulations are required for modelling these instabilities. This research was presented as a conference paper at the European Physics Society Conference [21]

CHAPTER 6 It is often seen that modes driven close to the stability threshold by fast particles from NBI exhibit a hard non-linear regime resulting in rapid frequency sweeping behaviour [22]. However those excited via ICRH accelerated ions have a tenancy to show saturated, amplitude modulation and chaotic behaviours [23, 24]. These regimes have been predicted in a previous marginal stability theory [25, 26] that incorporated the effect of velocity space diffusion and Krook collisions on the mode evolution. The interplay between the effect of the wave, that tries to distort the distribution function, and the effect of collisions, that act to restore the unstable distribution function, leads to the four non-linear regimes in Fig 1.8.

This chapter presenters a profound physical insight that when dynamical friction is the dominant collisional process only the explosive behaviour is possible. It is shown that, in MAST experiments with NBI, dynamical friction can indeed dominate over diffusion near the wave particle resonance. By noting that modes driven by ICRH are always dominated by a quasi-linear diffusive process, exceeding Coulomb diffusion by an order of magnitude [23], it is conjectured that dynamical friction is responsible for the experimentally observed differences between NBI and ICRH driven TAEs. This research has been submitted to Physics Review Letters (Dec 2008)

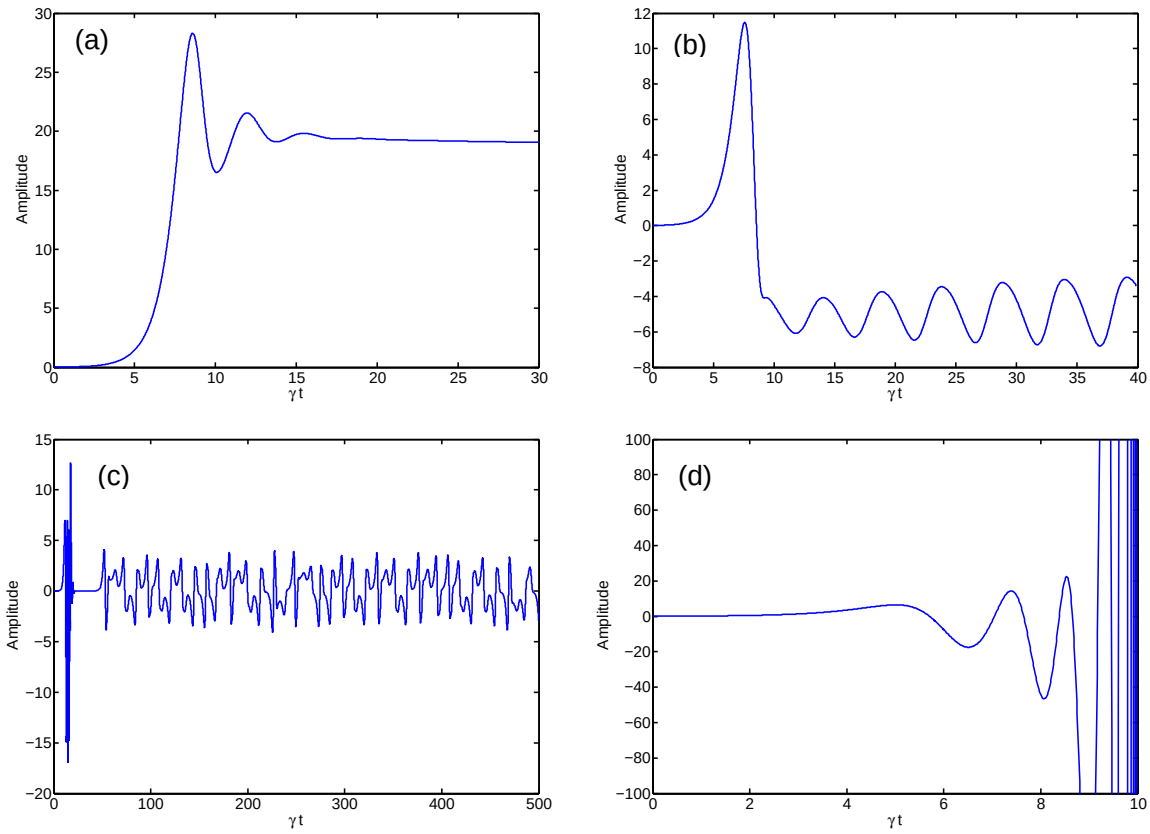

Figure 1.8: *Different regimes of marginally unstable amplitude evolution for velocity space diffusion collisions (a) steady state, (b) amplitude modulation (pitch fork splitting), (c) chaotic, (d) explosive*

Chapter 2

1-D Eigenmode model with $k_{||} \neq 0$

The term eigenmode in the context of waves in plasmas refers to solutions of a wave equation satisfying boundary conditions in the geometry of interest. In the case of an infinite homogeneous plasma the eigenmodes take the form of plane waves, however in an inhomogeneous plasma in toroidal geometry, such as that of a ST, the solutions usually take the form of a discrete spectrum. In general a set of three coupled partial differential equations of second order must be solved, which is a difficult task to analyse both analytically and numerically for an arbitrary plasma cross section and plasma parameters. For the high frequency eigenmodes, $\omega \sim \omega_{ci}$, of interest to this thesis, the Doppler shifted cyclotron resonances play an important role and so the effects of both non-zero ω/ω_{ci} and non-zero $k_{||}$ are crucial. It is possible however to reduce the complexity of the problem in some cases, namely high β plasmas and highly elliptical plasmas, and it is with this in mind that we employ a 1-D wave equation for the study of waves in the high β plasma of a Spherical Tokamak Power Plant (STPP) and the highly elliptical MAST tokamak plasma (see Chapter 4).

2.1 The Wave Equation and the Dielectric Tensor

Faraday's and Ampère's laws, along with the assumption of harmonic wave fields and currents, (ie $\mathbf{X} = \mathbf{X_0} e^{-i\omega t}$ where $\mathbf{X}$ can be perturbations of current $\mathbf{J}$ or electric

or magnetic field, **E** or **B**) lead to the general wave equation [27]

$$\nabla \times \nabla \times \mathbf{E} = \frac{\omega^2}{c^2}\varepsilon\mathbf{E}, \tag{2.1}$$

where $\varepsilon = I + i\sigma/\epsilon_0\omega$ is the dielectric tensor and σ is the electrical conductivity tensor. The 'cold plasma' approximation, where the frequency ω of the wave is much greater than the electron ion collision frequency ν_{ei}, and the phase velocity ω/k is much greater than the thermal speed of the ions v_{Ti} and electrons v_{Te}

$$\nu_{ei} \ll \omega, \quad v_{Te}, v_{Ti} \ll \frac{\omega}{k},$$

(such a description is also valid for $v_{Ti} \ll \omega/k \ll v_{Te}$ [27]) gives the following set of equations describing plasma dynamics

$$\mathbf{J} = \sum_s q_s n_s \mathbf{v}_s \tag{2.2a}$$

$$\frac{d\mathbf{v}_s}{dt} = \frac{q_s}{m_s}\left(\mathbf{E} + \mathbf{v}_s \times \mathbf{B}_0\right), \tag{2.2b}$$

with ε taking the form [27]

$$\varepsilon = \begin{pmatrix} \varepsilon_1 & i\varepsilon_2 & 0 \\ -i\varepsilon_2 & \varepsilon_1 & 0 \\ 0 & 0 & \varepsilon_3 \end{pmatrix} \tag{2.3}$$

where

$$\begin{aligned} \varepsilon_1 &= 1 - \sum_s \frac{\omega_{ps}^2}{\omega^2 - \omega_{cs}^2} \\ \varepsilon_2 &= -\sum_s \frac{\omega_{cs}}{\omega}\frac{\omega_{ps}^2}{\omega^2 - \omega_{cs}^2} \\ \varepsilon_3 &= 1 - \sum_s \frac{\omega_{ps}^2}{\omega^2}. \end{aligned} \tag{2.4}$$

Orthogonal coordinates with the equilibrium magnetic field aligned with the third ordinate ($\mathbf{e_z}$ in Cartesian geometry) are used and the summation is over species s.

2.2 Alfvén waves

2.2.1 Infinite homogeneous case

In an infinite homogeneous plasma $\nabla \rightarrow i\mathbf{k}$, where $\mathbf{k}$ is the wave vector. In this case Eq 2.1 is reduced to an algebraic equation

$$UN^4 + VN^2 + W = 0 \tag{2.5}$$

where $N = ck/\omega$ is the refractive index,

$$U = \varepsilon_1 \sin^2\theta + \varepsilon_3 \cos^2\theta \tag{2.6}$$

$$V = \left(\varepsilon_2^2 - \varepsilon_1^2\right)\sin^2\theta - \varepsilon_1\varepsilon_3\left(1 + \cos^2\theta\right) \tag{2.7}$$

$$W = \varepsilon_3\left(\varepsilon_1^2 - \varepsilon_2^2\right) \tag{2.8}$$

and θ is the angle with respect to the equilibrium magnetic field ($\mathbf{e_z}$ in this case) and without loss of generality $\mathbf{k} = \left(k_\perp, 0, k_\parallel\right)$. In the low frequency limit, $\omega \ll \omega_{pe,i}, \omega_{ce,i}$, $\varepsilon_3 \rightarrow \infty$ and $\varepsilon_2 \rightarrow 0$ due to quasi-neutrality. The dispersion relation then yields two branches, the shear Alfvén wave (SAW), and the compressional Alfvén wave (CAW), [28]

$$\omega = k_\parallel v_\mathrm{A} \qquad \text{SAW} \tag{2.9}$$

$$\omega = k v_\mathrm{A} \qquad \text{CAW.} \tag{2.10}$$

These branches are also observed in magnetohydrodynamics (MHD), which is a single fluid theory [29]. The shear wave produces perturbations in the magnetic field perpendicular to the equilibrium field (hence shear) but does not produce density perturbations (much like a wave on a string) and the compressional branch produces perturbations in the magnetic field and density (hence compressional). At frequencies comparable to the ion cyclotron frequency the effect of ε_2 on the Alfvén waves must be included (in the language of MHD the Hall effect must be included). For parallel propagating waves the dispersion relations take the form

$$N_\parallel^2 = 1 + \frac{\omega_{pi}^2}{\omega_{ci}\left(\omega - \omega_{ci}\right)} \quad \text{SAWs} \tag{2.11}$$

$$N_\parallel^2 = 1 + \frac{\omega_{pi}^2}{\omega_{ci}\left(\omega + \omega_{ci}\right)} \quad \text{CAWs} \tag{2.12}$$

which is illustrated in Fig 2.1. The shear branch becomes heavily damped in the limit $\omega \rightarrow \omega_{ci}$ due to the associated small wavelength [20]. For $\omega \sim \omega_{ci}$ the compressional branch is therefore expected to be the most relevant Alfvén branch.

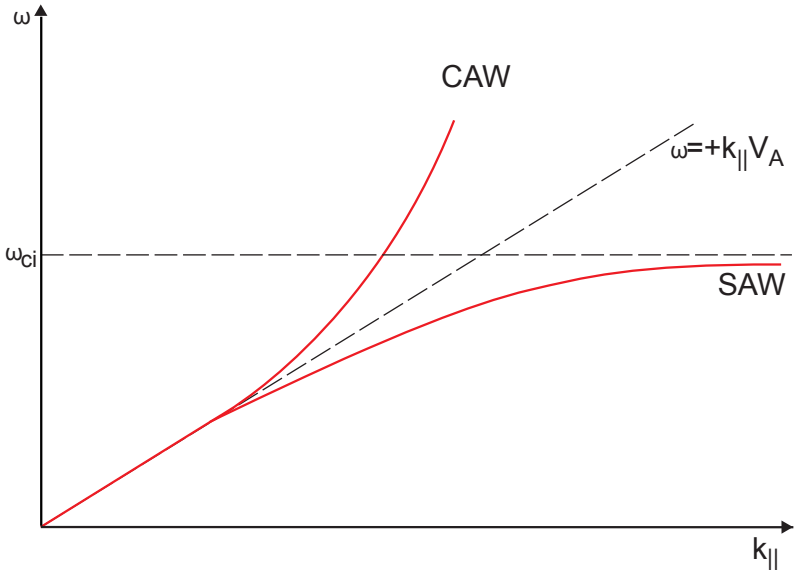

Figure 2.1: *Dispersion relation for the Alfvén waves with finite frequency correction.*

2.2.2 Bounded inhomogeneous case

For an arbitrary propagation angle the high frequency Alfvén waves can be described, via the perpendicular refractive index, as

$$N_{\perp}^2 = \frac{\left(\varepsilon_1 - N_{\|}^2\right)^2 - \varepsilon_2^2}{\varepsilon_1 - N_{\|}^2} \tag{2.13}$$

in the limit that the inhomogeneities occur on a much larger scale than the wavelength of the wave. In an inhomogeneous plasma ε_1 is a function of position and when the singularity $\varepsilon_1 = N_{\|}^2$ occurs for a wave with given ω and $k_{\|}$ the wave is 'mode converted' into the kinetic Alfvén wave when $\omega < \omega_{ci}$ and into an ion Berstein wave when $\omega > \omega_{ci}$. In the low frequency limit this singularity is identical to the shear Alfvén dispersion relation $\omega = k_{\|} v_{\mathrm{A}}$, and so the mode conversion can be viewed as a confluence of the compressional and shear waves. Physically the approach to $\varepsilon_1 = N_{\|}^2$ is accompanied by decrease in the perpendicular wavelength until the ion

Larmor radius is reached, at which point the cold plasma theory brakes down. At this scale kinetic damping mechanisms act to dissipate the wave [30].

For multiple ion species (e.g 1 and 2), the ion-ion hybrid wave replaces the compressional wave for frequencies $\omega_{ci1} < \omega < \omega_{ci2}$. In this case the motion of both sets of ions contributes significantly to the wave properties. The condition $\varepsilon_1 = N_{\|}^2$ then denotes the ion-ion hybrid resonance, which is important for ion heating [31].

For a bounded plasma with inhomogeneities occurring on the same scale as the wavelength of the wave, the full wave Eq 2.1 must be solved as an eigenvalue problem for the mode frequency (ω) and mode structure $\mathbf{E}(x, y, z)$.

2.3 The hollow cylinder approximation and the Eigenvalue Equation

To reduce the complexity of Eq 2.1 the geometry of a hollow cylinder [32] is adopted as shown in Fig 2.2. Here the toroidal aspect of the tokamak is retained whilst the poloidal dimension has been extended to infinity. In this way only the radial variation of the equilibrium parameters $\mathbf{B}(R)$ and $n(R)$ remains so that the dielectric tensor elements are reduced to $\varepsilon_1 = \varepsilon_1(R, \omega)$, $\varepsilon_2 = \varepsilon_2(R, \omega)$ and $\varepsilon_3 = \varepsilon_3(R, \omega)$. Recalling that the tokamak is already assumed to be axisymmetric, the problem is thus reduced to one dimension.

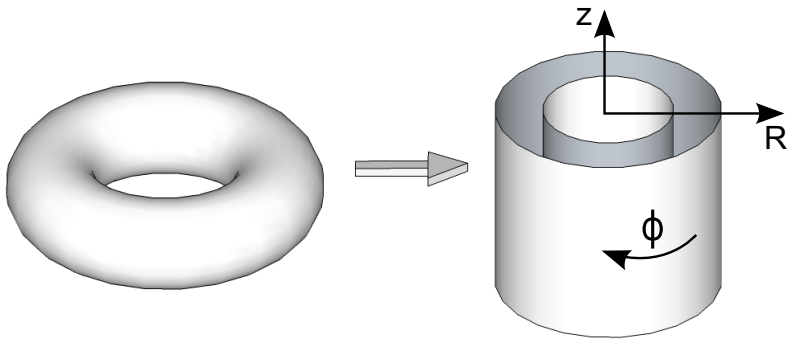

Figure 2.2: *A schematic of the hollow cylinder geometry*

By considering Eqs 2.1 and 2.3 for the hollow cylinder geometry, the following right handed set of coordinates should be used: (R, z, ϕ). Equation 2.1 is now considered

as an eigenvalue equation to be solved for an eigen-frequency ω. To simplify the analysis the equilibrium field is assumed to be purely toroidal in nature.

Firstly infinite electrical conductivity parallel to the magnetic field, ie $\varepsilon_3 \to \infty$ is assumed. The 'cold plasma' model then implies that the third component of Equation 2.1 is

$$E_\phi \equiv E_\parallel = 0 \tag{2.14}$$

(note by $\parallel$ we mean parallel to the equilibrium magnetic field $E_\parallel = \mathbf{E} \cdot \mathbf{B}_0/|\mathbf{B}_0|$). The two projections of Equation 2.1 perpendicular to $\mathbf{B_0}$ can then be written as [33]

$$-\left(\frac{\partial^2}{\partial z^2} + F\right) E_R + \left(\frac{\partial^2}{\partial R \partial z} - H\right) E_z = 0 \tag{2.15a}$$

$$\left(\frac{\partial^2}{\partial R \partial z} + \frac{1}{R}\frac{\partial}{\partial z} + H\right) E_R - \left(\frac{\partial^2}{\partial R^2} + \frac{1}{R}\frac{\partial}{\partial R} + F\right) E_z = 0 \tag{2.15b}$$

with $F = (\omega^2/c^2)\left(\varepsilon_1 - N_\parallel^2\right)$, $H = i\,(\omega^2/c^2)\,\varepsilon_2$. The hollow cylinder approximation naturally leads to the use of the assumption that the equilibrium plasma variables vary slowly in the vertical direction compared to the perturbations, i.e $\partial \ln B/\partial z \ll \partial \ln E_{R,z}/\partial z$. Eq 2.15 then becomes

$$\left(\frac{\partial^2}{\partial z^2} + \frac{1}{R}\frac{\partial}{\partial R} R \frac{\partial}{\partial R} + \frac{F^2 + H^2}{F} + \frac{H}{RF}\frac{\partial}{\partial z}\right) E_z = 0, \tag{2.16}$$

where $N_\parallel$ is assumed not be a function of position in the plasma. In the limit of $N_\parallel \to 0$ the results from Ref [33] are reproduced. The hollow cylinder approximation allows further simplification of Eq (2.16) by using

$$E_z\,(R, z) \simeq \hat{E}_z\,(R)\, e^{ik_z z}, \tag{2.17}$$

so that the vertical motion is that of a plane wave $\left(\frac{\partial}{\partial z} \to ik_z\right)$. Finally by taking E_z to be of the following form

$$\hat{E}_z = \Psi\,(R)\, R^{-1/2}, \tag{2.18}$$

one obtains (from Eq 2.16) an equation with only second order derivatives of Ψ:

$$\begin{aligned} \left(\frac{\partial^2}{\partial R^2} \right. &- \left. V\right) \Psi = 0 \\ V = k_z^2 + \frac{k_z}{R}\frac{\varepsilon_2}{\varepsilon_1 - N_\parallel^2} &- \frac{\omega^2}{c^2}\left[\varepsilon_1 - N_\parallel^2 - \frac{\varepsilon_2^2}{\varepsilon_1 - N_\parallel^2}\right] \\ &- \frac{1}{4R^2} \end{aligned} \tag{2.19}$$

where V is associated with a potential of the Schrödinger-like Eq 2.19. If one takes the Wentzel-Kramers-Brillouin (WKB, small wavelength or geometric optics) limit, then $k_R^2 = -V$ (where k_R is the radial component of the wave vector related to the perpendicular refractive index in Eq 2.13) and a discrete spectrum of modes is found to be localised in a region $R_1 < R < R_2$ between two cut-offs ($k_R(R_1) = k_R(R_1) = 0$) generated by the radial inhomoengeities. In this case the quantisation condition [34]

$$\int_{R_1}^{R_2} k_R(R)\, dR = \pi\left(l + \frac{1}{2}\right), \quad l = 0, 1, 2\ldots \tag{2.20}$$

describes the resulting spectrum. Radially localised eigenmodes can therefore be expected to exist (even in the non WKB limit) if we have at least one point in the plasma where $V = 0$. From this logic one can foresee from Eq 2.19 that radially localised eigenmodes are unlikely to exist with very large vertical wave vectors k_z.

It can also be seen in Eq 2.19 that V exhibits a singularity when $\varepsilon_1 = N_\parallel^2$. This singularity is associated with a mode conversion described in section 2.2.2, which is an important factor in Alfvén wave damping. The radial structure of these mode conversion layers will be discussed further in section 2.5.1. Here we note that the weakly damped eigenmodes considered in this thesis have $\varepsilon_1 \neq N_\parallel^2$ in the localisation region. Eq 2.19 gives information on the frequency and structure of any eigenmodes supported by the plasma consistent with the approximations.

2.4 Applicability of the 1-D model

For EM waves in the frequency range $\omega \sim \omega_{ci}$, the hollow cylinder model is only applicable if the plasma equilibrium is sufficiently 1-D. For a tokamak plasma the geometry of the magnetic flux surfaces shows the dimensionality of the equilibrium and for large aspect ratio low β plasmas the magnetic flux surfaces take the approximate form of concentric circles as shown in Fig 2.3. In the case of 2-D plasma equilibria the density (and hence ω_{pi} and therefore $\varepsilon_{1,2,3}$) varies over the vertical direction as much as in the radial direction. High β plasmas ($\beta \sim 1$) however have

a 1-D equilibrium in the core of the plasma [35] (i.e the flux surfaces are accurately modelled by straight vertical lines), and so provides a slowly varying density in the vertical direction i.e $\varepsilon = \varepsilon(R)$ in the plasma core as illustrated by Fig 2.4.

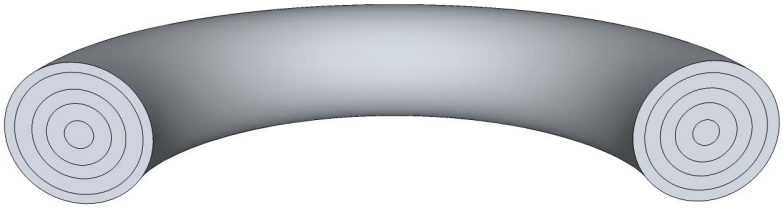

Figure 2.3: *A schematic of a large aspect ratio tokamak with circular flux surfaces*

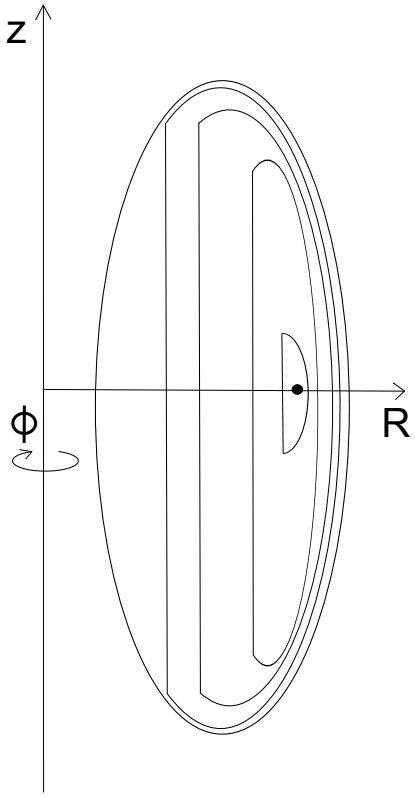

Figure 2.4: *Shows a typical high $\beta \sim 1$ elliptical plasma with D shaped flux surfaces. There exists a 'core' region of the plasma where these flux surfaces are 1-D, and there exists a narrow 'boundary layer' where the curvature is important (the black dot represents the 'magnetic axis') [35].*

The same can also be said for a highly elliptical plasma shown in Fig 2.4. In this case the equilibrium is forced into a 1-D configuration by geometry alone. Both of these regimes fall into the operational parameter ranges of spherical tokamaks,

whose plasmas are naturally elongated and will operate a much higher β values than conventional low aspect ratio tokamaks. The 1-D model is therefore ideally suited to burning plasmas in STs, which exhibit a 1-D equilibrium.

2.5 Application of the 1-D model to the STPP

A STPP equilibrium (Fig 2.5) is computed with the 'SCENE' code [36]. It exhibits a 1-D equilibrium as described in section 2.4 and a magnetic well in the total field $|\mathbf{B_0}|$ (Fig 2.6). In the frequency range of interest, $\omega \ll \omega_{pi}, \omega_{pe}$, the dielectric tensor elements $\varepsilon_1, \varepsilon_2$ for deuterium-tritium (D-T) plasma take the following form for the 1-D equilibrium geometry of the STPP plasma core

$$\begin{aligned}
\varepsilon_1(R,\omega) &\approx \varepsilon_{1D}(R,\omega) + \varepsilon_{1T}(R,\omega) \\
\varepsilon_2(R,\omega) &\approx \frac{\omega}{\omega_{cD}(R,\omega)}\varepsilon_{1D}(R,\omega) + \frac{\omega}{\omega_{cT}(R,\omega)}\varepsilon_{1T}(R,\omega) \\
\varepsilon_{1D}(R,\omega) &= -\frac{\omega_{pD}^2(R,\omega)}{\omega^2 - \omega_{cD}^2(R,\omega)} \\
\varepsilon_{1T}(R,\omega) &= -\frac{\omega_{pT}^2(R,\omega)}{\omega^2 - \omega_{cT}^2(R,\omega)}.
\end{aligned} \tag{2.21}$$

where D and T label the deuterium and tritium species respectively. Due to the two ion terms in Eq (2.21) the behaviour of ε_1 in D-T differs from that of a single ion species plasma, especially in the frequency range $\omega_{cT} < \omega < \omega_{cD}$, where ion-ion hybrid waves can exist and the $\varepsilon_1 = 0$ [31] can occur in the core of the plasma. For the STPP modelling the equilibrium plasma density is taken not to vary with radius. This approximation is consistent with high performance high confinement (H-mode) plasmas expected in a power plant scenario, where the core density is approximately constant. The localisation of eigenmodes in this case arises due to the existence of the well in the equilibrium magnetic field as seen in Fig 2.6.

To solve Eq 2.19 V is expanded around $R = \widetilde{R}$, where $\widetilde{R}$ corresponds to a radius at which V achieves a local minimum, and terms up to quadratic order are kept. Eq 2.19 then reduces to

$$\frac{\partial^2\Psi}{\partial R^2} - \left\{ V\left(\widetilde{R}\right) + \frac{1}{2}\left(R - \widetilde{R}\right)^2 \left.\frac{\partial^2 V}{\partial R^2}\right|_{(\widetilde{R})} \right\} \Psi = 0. \tag{2.22}$$

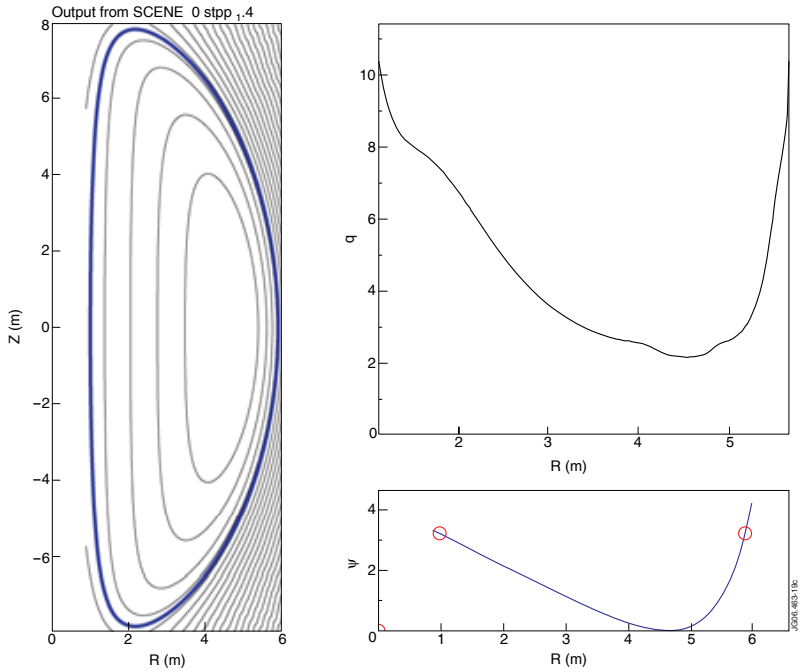

Figure 2.5: *Illustrates the 1D nature of the flux surfaces in the core of the plasma, along with the safety factor q and flux function ψ as functions of major radius R in the mid-plane (from the 'SCENE' code [36]).*

Eq 2.22 uses the harmonic oscillator approximation to the potential V, and is the form used by Gorelenkova [33] to solve the eigenvalue equation. By using well known solutions to the Schrödinger equation with a harmonic potential [34], one can manipulate Eq 2.22 into the correct form and find solutions for the eigenfrequency ω. However, from Fig 2.6 one can clearly see the asymmetric nature of the magnetic field, and hence the potential V. We therefore seek an analytical method which captures this asymmetry, such as the following Schrödinger equation, which utilises an asymmetric potential [34]

$$\Psi'' + \left(b - ce^{2dx} + 2ce^{dx}\right)\Psi = 0, \tag{2.23}$$

where $x = R - \widetilde{R}$ and b, c and d are to be determined so that Eq 2.22 can be written in the form of Eq 2.23. Firstly by rewriting the potential V (by bringing the constant part out) as

$$V = k_z^2 + \widetilde{V}$$

$$\widetilde{V} = \frac{k_z}{R}\frac{\varepsilon_2}{\varepsilon_1 - N_{\|}^2} - \frac{\omega^2}{c^2}\left[\varepsilon_1 - N_{\|}^2 - \frac{\varepsilon_2^2}{\varepsilon_1 - N_{\|}^2}\right] - \frac{1}{4R^2},$$

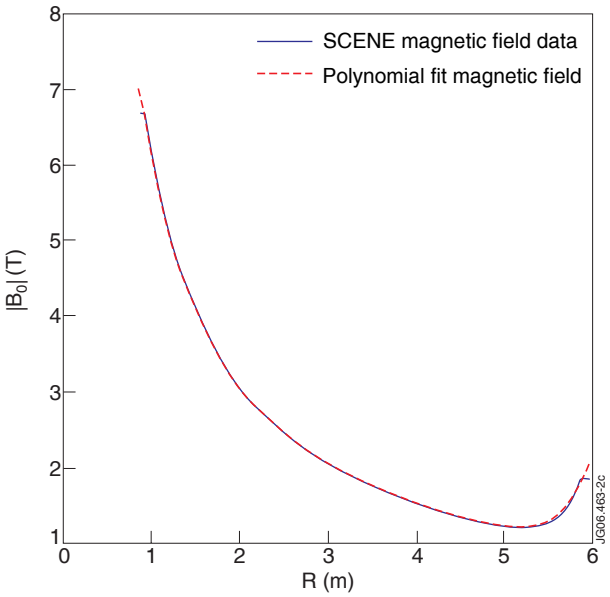

Figure 2.6: *Total equilibrium magnetic field profile to be used in our analysis (8^{th} order polynomial, dashed), and the original 'SCENE' data (solid)*

Eq 2.22 can then be rewritten as

$$\frac{\partial^2 \Psi}{\partial R^2} - \left\{ k_z^2 + \widetilde{V}\left(\widetilde{R}\right) + \frac{1}{2}\left(R - \widetilde{R}\right)^2 \left.\frac{\partial^2 \widetilde{V}}{\partial R^2}\right|_{\left(\widetilde{R}\right)} \right\} \Psi = 0, \tag{2.24}$$

Secondly notice that, from Eq 2.23, a Taylor expansion of $U = ce^{2dx} - 2ce^{dx}$ about $R = \widetilde{R}$ up to second order yields

$$U \approx -c + cd^2 \left(R - \widetilde{R}\right)^2. \tag{2.25}$$

Finally, by comparing Eqs 2.23 2.24 and 2.25, Eq (2.22) can be written in the form of Eq 2.23 by defining the following

$$b = -k_z^2, \quad -\widetilde{V} = c, \quad d = \left(\frac{-\frac{1}{2} \left.\frac{\partial^2 \widetilde{V}}{\partial R^2}\right|_{\widetilde{R}}}{\widetilde{V}\left(\widetilde{R}\right)} \right)^{\frac{1}{2}}. \tag{2.26}$$

The eigenvalues of Eq 2.23 have the following solution [34]

$$-b = c\left[1 + \frac{d}{\sqrt{c}}\left(p + \frac{1}{2}\right)\right]^2 \tag{2.27}$$

and the eigenfunctions have the following form [34]

$$\Psi = \mathscr{C} e^{-\frac{\xi}{2}} \xi^g w\left(\xi\right) \tag{2.28}$$

p	f_1	f_2	f_3
0	1.02	1.31	2.37
1	1.14	1.37	2.17
2	-	1.58	1.84

Table 2.1: *Frequencies, normalised to the minimum cyclotron frequency of tritium* $f_{cT}\left(\widetilde{R}\right) = 6.13MHz$ *calculated using the Taylor expansion method with an asymmetric potential for* $N_{\|} = 100$ *and* $\kappa_T = 0.5$*. Note the minimum cyclotron frequency of Deuterium is* $f_{cD}\left(\widetilde{R}\right) = 9.2MHz$

where

$$\xi = \frac{2\sqrt{c}}{d} e^{d\left(R-\widetilde{R}\right)}, \quad g = \frac{\sqrt{c}}{d} - p - \frac{1}{2}, \quad (p = 0, 1, 2...)$$

$w(\xi)$ is the confluent hypergeometric function: $w = F(-p, 2g+1, \xi)$, and positive g has to be taken so that $\sqrt{c}/d > p + 1/2$, $\mathscr{C}$ is an arbitrary constant. The eigenfrequencies are then found by solving the following equation for ω

$$k_z^2 = -\widetilde{V}\left(\widetilde{R}\right)\left[1 + \frac{1}{\left|\widetilde{V}\left(\widetilde{R}\right)\right|}\left(\frac{1}{2}\left.\frac{\partial^2 \widetilde{V}}{\partial R^2}\right|_{\widetilde{R}}\right)^{\frac{1}{2}}\left(p + \frac{1}{2}\right)\right]^2. \tag{2.29}$$

Taking $k_z = 16.7\text{m}^{-1}$ (as in Reference [33]), using the optimum power plant D-T mixture of $\kappa_T = 0.5$ and using $N_{\|} = 100$, multiple frequencies are found for each value of p, three in total (labelled from f_1 to f_3) that are consistent with the mathematical applicability regime displayed in Fig 2.7. Table 2.1 shows frequencies that have been calculated using the above approach, assuming that $\widetilde{R} = 5.19\text{m}$, which is a robust approximation over a wide range of frequencies. All frequencies f_1 and frequencies f_2 (for $p = 0, 1$) correspond to ion-ion hybrid eigenmodes with $\omega_{cT} < \omega < \omega_{cD}$, while f_2 (for $p = 2$) and all of frequencies f_3 correspond to compressional Alfvén eigenmodes with $\omega > \omega_{cD}$.

A comparison of the asymmetric and harmonic approximations is made in Figs 2.8 and 2.9 by comparing the full potential to the approximated ones described in Eqs 2.22 (harmonic) and 2.24 (asymmetric) (note the asymmetric potential is plotted by taking Eq 2.24 and approximating the $\widetilde{V}$ parts by U consistent with Eq 2.25). Fig 2.8 appears to suggest the asymmetric method is a better approximation than

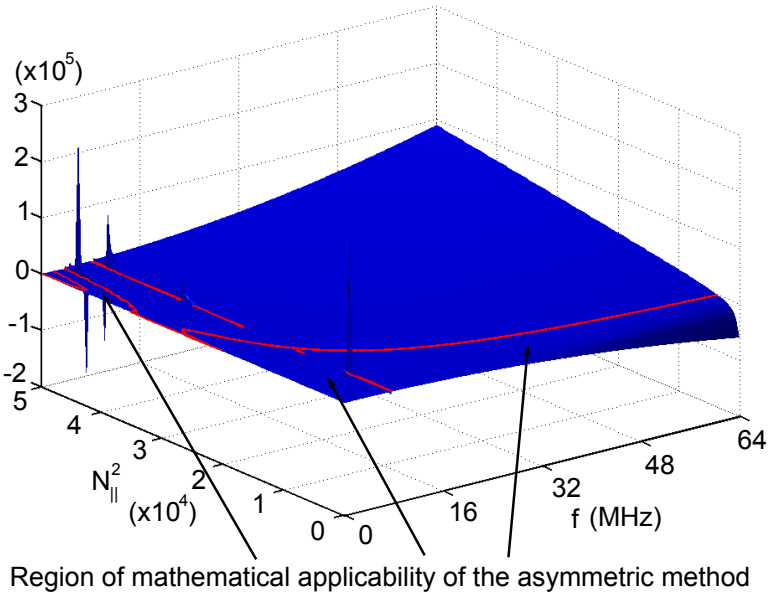

Figure 2.7: *Plot of* $\widetilde{V}\left(\widetilde{R}\right)$ *as a function of* f *and* $N_{\|}^2$ *for* $\kappa_T = 0.5$. *The line on the surface indicates the zeros of the function, and hence shows the boundaries of regions where we can and cannot apply the asymmetric method. The spikes in this figure result from the* $\varepsilon_1 = N_{\|}^2$ *condition.*

the harmonic one. However, when mode conversion layers are present in the core of the plasma as shown in Fig 2.9, the harmonic potential is a better fit to the full potential on the inboard side, and the asymmetric is a better fit to the full potential at the outboard side. The main difference between the asymmetric method and the harmonic one, is that the eigenfunction (and hence the perturbed electric field) need not be centred at the minimum of the potential well and can in fact be skewed. Figs, 2.10 and 2.11 show the potential and $p = 0$ eigenfunctions for the asymmetric method corresponding to Figs 2.8 and 2.9. As can be seen from References [37, 38], the proximity of the mode conversion layer to the eigenfunction provides a damping mechanism, since for the $\omega > \omega_{cT}$ case the ion Bernstein waves resulting from the mode conversion at $\varepsilon_1 = N_{\|}^2$ are heavily damped. The distance between the mode localisation region and the mode conversion layer is thus an important parameter in determining the rate of mode damping, which can be calculated in accordance with References [37, 38]. Fig 2.10 shows an example of a weakly damped mode, whereas Fig 2.11 shows a mode that is expected to be heavily damped due to the mode conversion. From Fig 2.11 it also can be seen that the eigenfunction penetrates into

the inner mode conversion layer more so than the outer one due to the asymmetry in the eigenfunction. This asymmetric feature therefore suggests a preference for energy deposition into the plasma.

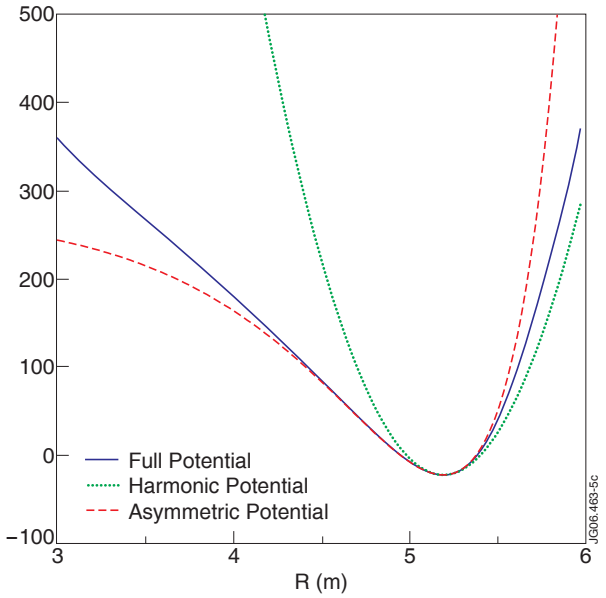

Figure 2.8: *The full potential along with the corresponding harmonic and asymmetric approximations for* $\kappa_T = 0.5$, $N_{\|} = 100$ *and* $f/f_{cT} = 1.02$

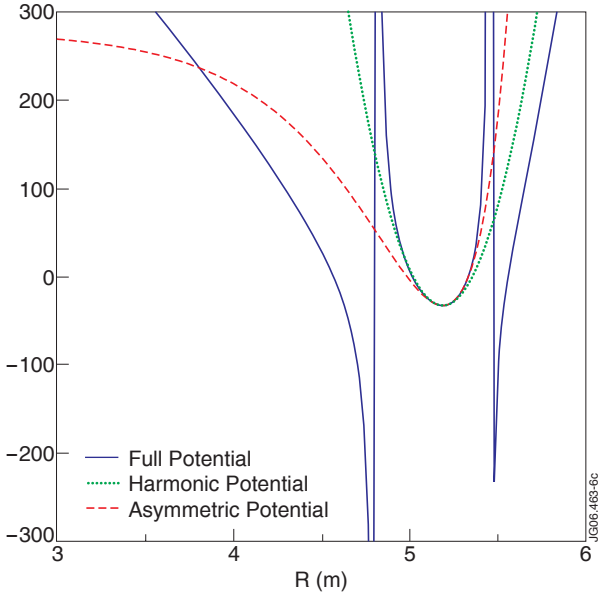

Figure 2.9: *The full potential along with the corresponding harmonic and asymmetric approximations for* $\kappa_T = 0.5$, $N_{\|} = 100$ *and* $f/f_{cT} = 1.31$. *Note the spikes in this figure are a result of the mode conversion layer* $\varepsilon_1 = N_{\|}^2$

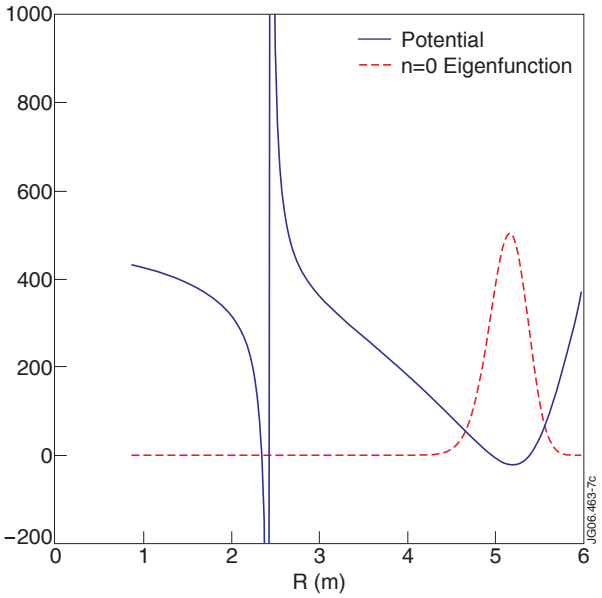

Figure 2.10: *The full potential along with the z component of the electric field corresponding to the $p = 0$ eigenfunction (plotted in arbitrary units) for $\kappa_T = 0.5$, $N_{\|} = 100$ and $f/f_{cT} = 1.02$. Note the spikes in this figure are a result of the mode conversion layer $\varepsilon_1 = N_{\|}^2$*

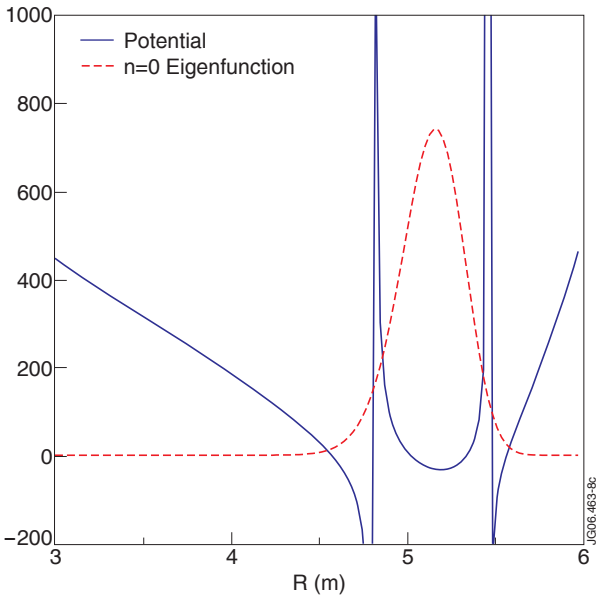

Figure 2.11: *The full potential along with the z component of the electric field corresponding to the $p = 0$ eigenfunction (plotted in arbitrary units) for $\kappa_T = 0.5$, $N_{\|} = 100$ and $f/f_{cT} = 1.31$. Note the spikes in this figure are a result of the mode conversion layer $\varepsilon_1 = N_{\|}^2$*

2.5.1 Radial Structure of Mode Conversion Layers $\varepsilon_1(R) = N_{\|}^2$

In a single ion species plasma, such as deuterium, with a uniform density, ε_1 takes the following approximate form

$$\varepsilon_1(R,\omega) \approx -\frac{\omega_{pD}^2}{\omega^2 - \omega_{cD}^2(R)}, \tag{2.30}$$

due to $B = B(R)$. The mode conversion from the fast compressional Alfvén wave with $\omega > \omega_{c_D}$ to the ion Berstein wave occurs at the $\varepsilon_1(R) = N_{\|}^2$ surface when thermal effects are included [27] and constitutes one of the main damping mechanisms for fast compressional Alfvén waves. For a single ion species plasma Eq (2.30) shows that the plasma can be divided into sections where mode conversion can occur ($\varepsilon_1 > 0 \implies \omega < \omega_{cD}$) and where it cannot. For a two ion species plasma, such as D-T, ε_1 is given by the sum of two terms in Eq 2.21 and so the situation is more complicated depending on the mode frequency ω. Seven different frequency regimes are identified as Fig 2.12 shows. Here the radial position of the mode conversion layers are found in a STPP for different frequency regimes with 50:50 D-T mix.

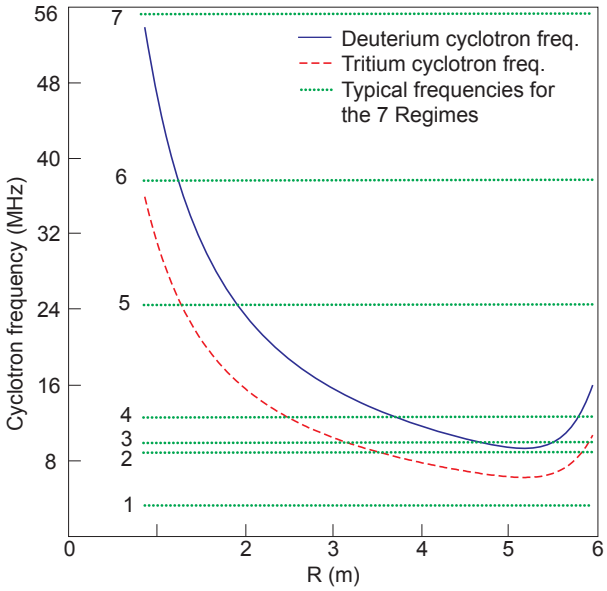

Figure 2.12: *Cyclotron frequencies calculated using the magnetic field from Figure 2.6 and typical frequencies for Regimes 1 to 7*

REGIME 1 $\omega < \omega_{cD}, \omega_{cT}$, which implies that $\varepsilon_1(R) > 0$ and so $\varepsilon_1(R) = N_{\|}^2$ mode conversion may be possible depending on the value of $N_{\|}$. Fig 2.13 shows an example of $\varepsilon_1(R)$ for a frequency in this regime; note that $N_{\|}$ will have to be of the order of 100 for the mode conversion surface to occur in the core of the plasma. It should also be noted that ε_1 does not go to zero at the inboard side of the torus, so there is a $N_{\|}$ threshold for the mode conversion to occur.

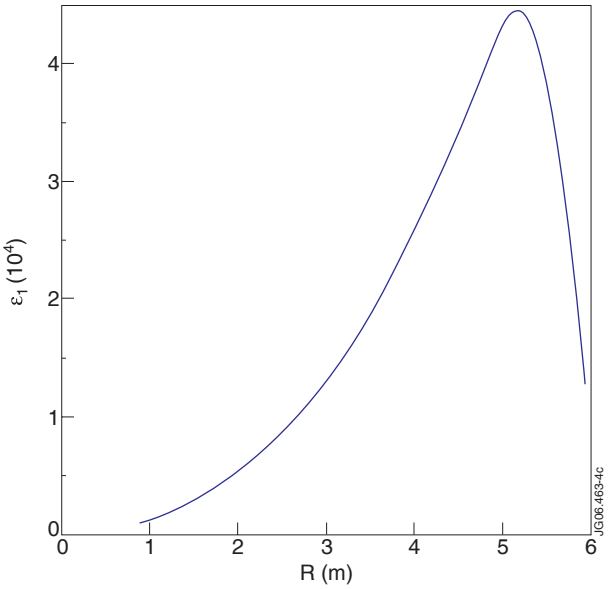

Figure 2.13: ε_1 *for* $\kappa_T = 0.5$ *and* $f/f_{cT} = 0.52$

REGIME 2 $\omega_{cT}^{\min} < \omega < \omega_{cD}^{\min}$, where the minimum values $\omega_{cT}^{\min}$ and $\omega_{cD}^{\min}$ are close to the magnetic axis (see Fig 2.5). Depending on $\left|\omega - \omega_{cD}^{\min}\right|$ mode conversion may or may not occur. Referring to Fig 2.12, to the far left (e.g $R < 3m$) $\omega < \omega_{cD}, \omega_{cT}$ and so $\varepsilon_1(R) > 0$ and, as in Regime 1, mode conversion may be possible depending on $N_{\|}$. As we approach $\omega \to \omega_{cT}$, the dielectric element $\varepsilon_1 \to +\infty$. Just to the right of this singularity in $\varepsilon_1(R)$, where $\omega > \omega_{cT}$, one observes $\varepsilon_1 < 0$. Since $\omega < \omega_{cD}$ in this region, the deuterium term provides a positive contribution to ε_1, however unless $\left|\omega - \omega_{cD}^{\min}\right|$ is small, mode conversion will not occur. Fig 2.14 shows an example of where mode conversion is possible; note that there is no $N_{\|}$ threshold needed for mode conversion, since ε_1 is continuous through zero around the magnetic axis. Fig 2.15 shows an enlarged section of Fig 2.14.

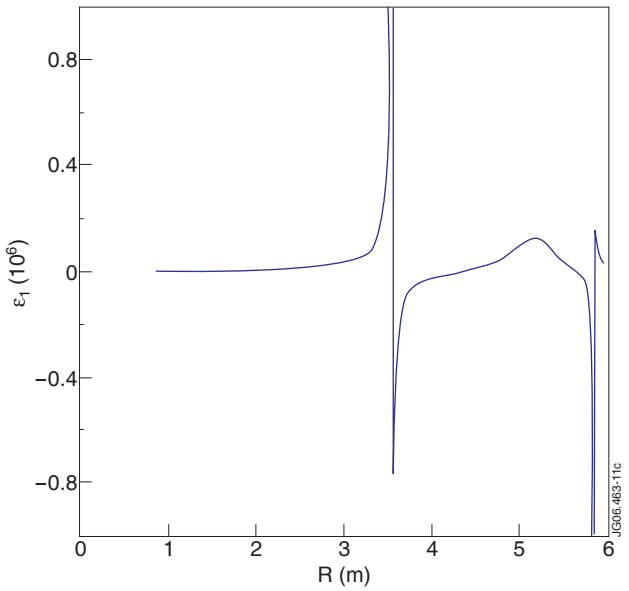

Figure 2.14: ε_1 *for* $\kappa_T = 0.5$ *and* $f/f_{cT} = 1.44$

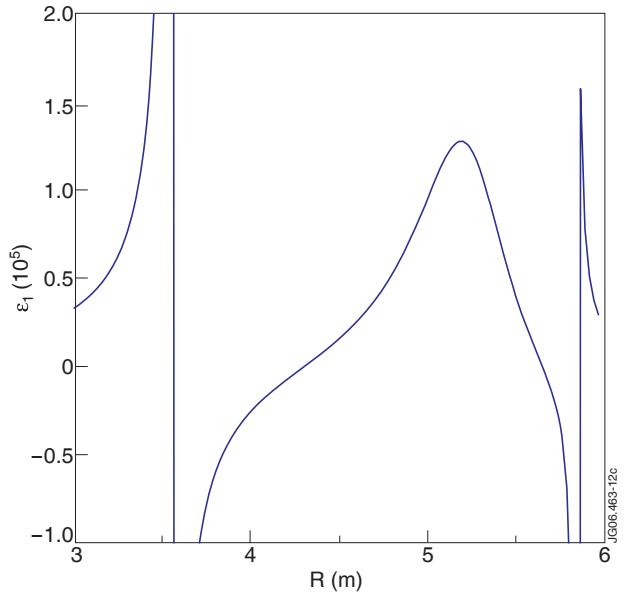

Figure 2.15: *An enlarged section of Fig 2.14*

REGIME 3 Referring to Fig 2.12, the far left displays the same behaviour as Regime 2 and Fig 2.16 shows an example of this regime. As before $\varepsilon_1 < 0$ as we pass through $\omega = \omega_{cT}$, however ε_1 is guaranteed to change sign as the positive contribution from ε_{1D} becomes larger as $\omega \to \omega_{cD}$. Thus ε_1 will smoothly increase through zero, so that mode conversion will occur, with no $N_{\|}$ threshold. As the deuterium singularity is traversed, $\omega > \omega_{cD}, \omega_{cT}$ and so there is a region where $\varepsilon_1 < 0$ and so

no mode conversion. Finally, the outboard side of the plasma shows the reversed trend, so that there will be one more definite mode conversion, and a conditional one depending on the value of $N_{\|}$.

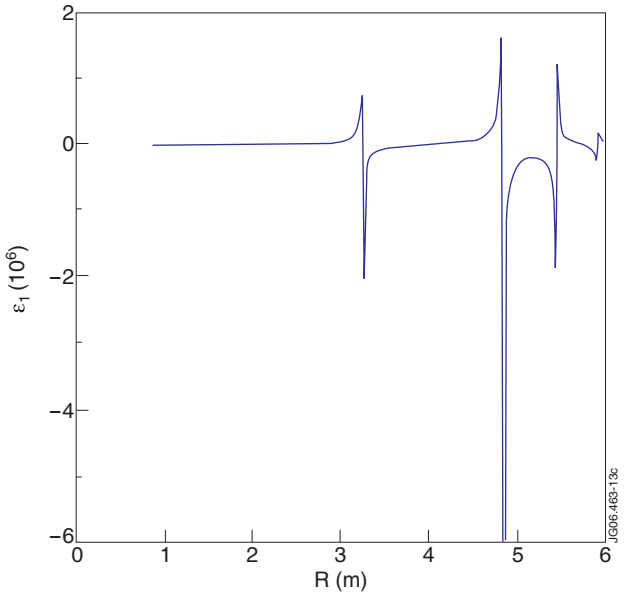

Figure 2.16: ε_1 *for* $\kappa_T = 0.5$ *and* $f/f_{cT} = 1.55$

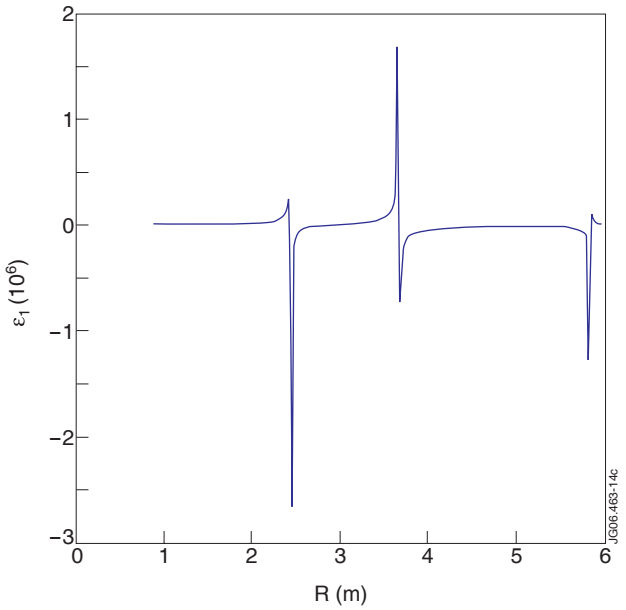

Figure 2.17: ε_1 *for* $\kappa_T = 0.5$ *and* $f/f_{cT} = 2.07$

REGIME 4 This regime is almost identical to Regime 3, the difference being there is no guaranteed mode conversion at the outboard side any more, Fig 2.17 shows

an example of this regime, when mode conversion at the outboard can occur. The absence of the outboard mode conversion can be due to $\omega > \omega_{cT}$ at the outboard side, so that there is no tritium singularity. The implication is that one may have mode conversion, however it depends on the value of $N_{\|}$ (there is now a threshold again).

REGIME 5 The mode conversion behaviour has already been described; the mode conversion is always present when $\omega_{cT} < \omega < \omega_{cD}$ and may be present at the inboard side. Note no mode conversion can occur at the outboard side any more, since $\omega > \omega_{cD}, \omega_{cT}$. Fig 2.18 shows an example of this regime.

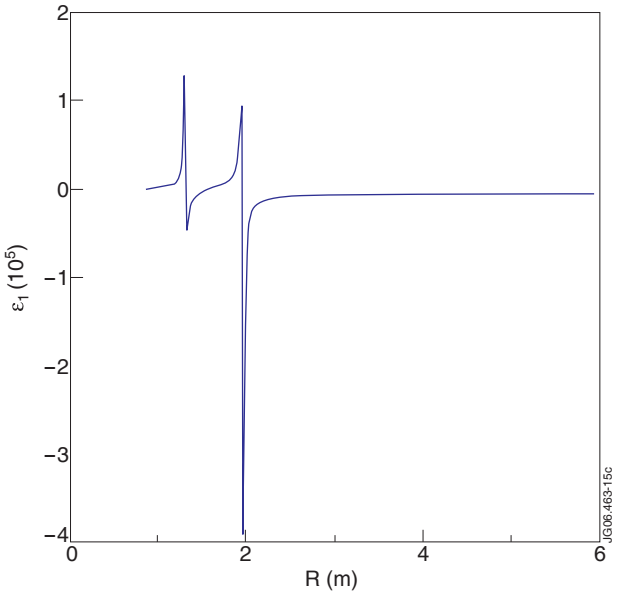

Figure 2.18: ε_1 *for* $\kappa_T = 0.5$ *and* $f/f_{cT} = 3.9$

REGIME 6 This regime displays the same behaviour at the inboard side as Regime 4 at the the outboard side. Mode conversion depends on how high the frequency is: if it is too high then there will be a threshold value of $N_{\|}^2$, otherwise ε_1 decreases smoothly through zero and a guaranteed mode conversion occurs. Fig 2.19 shows an example of when mode conversion can occur.

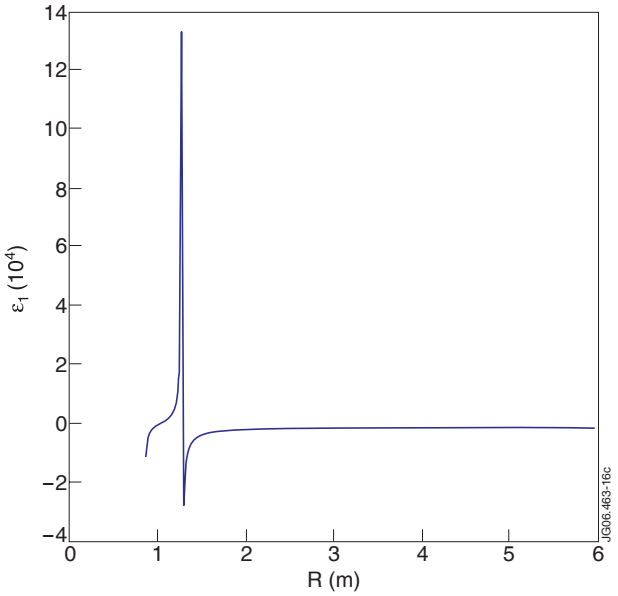

Figure 2.19: ε_1 *for* $\kappa_T = 0.5$ *and* $f/f_{cT} = 5.97$

REGIME 7 Finally for this regime, $\omega > \omega_{cD}, \omega_{cT}$, which means $\varepsilon_1 < 0$ and so no mode conversion is possible.

2.5.2 MHD spectroscopy of the D-T concentration from EM modes in a STPP

By analysing how the eigen-frequencies (calculated in Section 2.5) vary as a function of D-T concentration and $N_{\|}$, one can think of an active frequency sweeping diagnostic, with an external antenna in the proper frequency range, used to determine the D-T concentration [13]. This is one of the most important operational parameters for a power plant, as any deviation from the ideal mixture of 50:50 dramatically reduces the fusion yield as described in chapter 1. Measurement of the spectral lines of deuterium and tritium atoms can indicate the D-T mix [39], however this can only be performed in the cooler regions such as the plasma edge where neutral atoms can still exist. Core measurements however are not possible using this technique, and so the development of alternative techniques is required. By matching the frequency of the externally launched wave to that of the eigenmode, a resonant response of the plasma could be searched for and if detected indicate the D-T mix (see Fig 2.20).

We seek to find what value of $N_{\|}$ maximises the change in mode frequency for

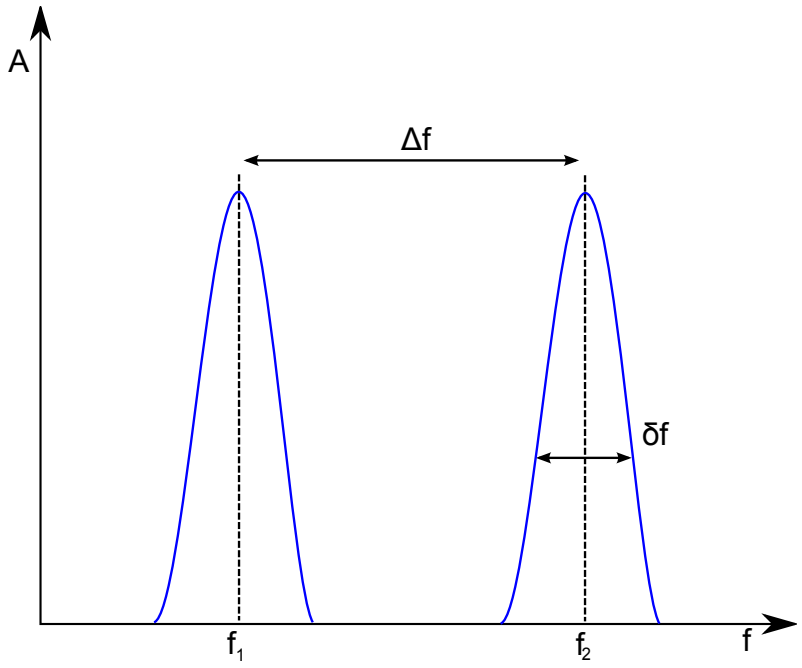

Figure 2.20: *Illustrates the external antenna technique. A cross correlation between the launched wave and the plasma perturbations gives the response of the plasma A. f_1 and f_2 are eigenfrequencies, δf is related to the damping of the mode. As long as the damping is small, so that $\delta f < \Delta f$, the two frequencies can be resolved.*

a given change in D-T concentration (i.e $df/d\kappa_T$), since this makes the diagnostic technique most sensitive. If the mode damping is weak enough the width of the resonance peak will be small, and so diagnosing the D-T concentration will be more accurate. For this reason the analysis focuses on the f_1 eigenfrequency, since it can be seen from Fig 2.10 that $\varepsilon_1 = N_{\|}^2$ occurs far away from the region of mode localisation. A discussion of f_2, where the damping is expected to be strong, is reserved for section 2.5.3. Fig 2.21 shows the $p = 0$ f_1 eigenfrequencies as a function of κ_T and $N_{\|}^2$. One can see that Fig 2.21 is largely monotonic, and so by choosing $N_{\|}^2 = 7000$ one is able to obtain a unique eigenfrequency for a given κ_T, and also maximise $df/d\kappa_T$, and hence the sensitivity of the diagnostic. Fig 2.21 also shows that the sensitivity of $df/d\kappa_T$ as a function of $N_{\|}$ is not strong. This indicates that an external antenna probing the plasma may have a broad choice of $N_{\|}$ values so that the launching technique should not be restricted. Table 2.1 shows that the frequency separation, Δf between modes with different radial mode numbers, p, as well as frequency separation between different types of mode, is significant

enough (more than $\Delta f/f \sim 10\%$) in most cases, so that mode damping below this value would still be acceptable for indentifying the resonance peaks with an external antenna.

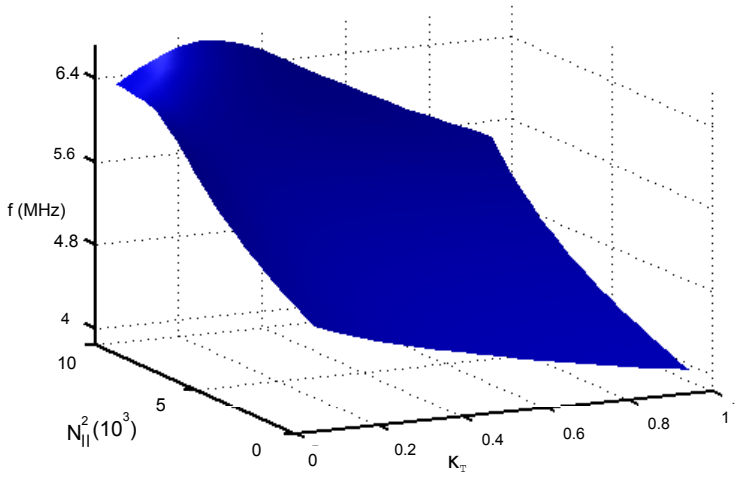

Figure 2.21: *Shows f_1 as a function of κ_T and $N_{\|}^2$*

2.5.3 Cut-off Resonance Couplet

The MHD spectroscopy method described in section 2.5.2 relied on scanning for weakly damped eigenmodes to obtain a well resolved plasma response. This method however is not suitable for heavily damped modes such as in Fig 2.11 where the eigenmode is in close proximity to the mode conversion layer $\varepsilon_1 = N_{\|}^2$. In this case, providing the wavelength of the eigenmode is longer than the distance between the cut-off ($V = 0$) and mode conversion $\left(\varepsilon_1 = N_{\|}^2\right)$ positions (the couplet distance), then the wave may tunnel through and be detected externally. This tunnelling phenomenon is also used for ion-ion hybrid layer reflectometry for measuring the plasma ion species mix (even in the case of launching microwave beams from the high field side) [40]. A calculation of the couplet distance is therefore required to identify whether eigenmodes excited by e.g. alpha particles can be detected externally.

κ_T	$\delta\,(m)$	$\epsilon\,(m)$
0.2	2.453	-
0.33	0.6228	0.2209
0.5	0.2905	0.1103
0.4	0.1550	0.0649
0.66	0.1083	0.0507
0.71	0.0903	0.0471
0.75	0.0829	0.0478
0.77	0.0816	0.0517
0.8	0.0866	0.0605

Table 2.2: *Couplet distances as a function of* κ_T *for* $f/f_{cT} = 1.42$ *and* $N_{\|} = 100$.

$N_{\|}^2$	$\delta\,(m)$	$\epsilon\,(m)$
0	0.1240	0.0390
1000	0.1184	0.0375
2000	0.1132	0.0362
3000	0.1085	0.0350
4000	0.1047	0.0340
5000	0.1022	0.0335
6000	0.1022	0.0339
7000	0.1072	0.0359
8000	0.1240	0.0423
9000	0.1733	0.0611
10000	0.2905	0.1103

Table 2.3: *Couplet distances as a function of* $N_{\|}^2$ *for* $f/f_{cT} = 1.42$ *and* $\kappa_T = 0.5$.

We focus on frequencies in regime 2 from the last section, and define δ and ϵ to be the distance from the mode conversion layer to $V = 0$ on the inboard and outboard side of the potential, respectively. By keeping $f/f_{cT} = 1.42$ fixed, the concentration of tritium κ_T and $N_\parallel^2$ are varied to see their effect on the couplet distance. Fig 2.11 shows the wavelength of the eigenmodes is about 1m, and from Tables 2.2 and 2.3 one can see that the couplet distances are (except in the case $\kappa_T = 0.2$) shorter than one wavelength. This gives an indication that modes excited by energetic alpha particles in the D-T plasma of a STPP could be detected externally and give information about the D-T mixture ratio.

2.6 Discussion

For high β STPP equilibria, it has been shown that the characteristic well in the equilibrium magnetic field acts as a resonating cavity for electromagnetic waves, forming discrete spectra of compressional Alfvén ($\omega > \omega_{cD}$) and ion-ion hybrid eigenmodes ($\omega_{cT} < \omega < \omega_{cD}$) in the plasma core. The frequency and structure of these eigenmodes have been calculated using the 1-D model with $k_\parallel \neq 0$ in the 'cold plasma' approximation with D-T mixture effects taken into account. The cold plasma approximation provides a first insight into the modes and the radial structure of the cut-offs and mode conversion positions over a broad range of $k_\parallel$ and frequencies not accessible by more complex methods. Inclusion of D-T effects in the calculation reveals a discrete spectrum of eigenfrequencies not only above the ion cyclotron frequency but also in the ion-ion hybrid frequency range. Taking into account the dependence of the eigenfrequencies on the D-T concentration, the dependence with respect to $k_\parallel$ has been optimised in order to obtain the maximum value of $df/d\kappa_T$. The possibility of using the eigenmodes as a diagnostic for measuring the D-T concentration, by observing α particle driven emission or probing the discrete spectrum with externally launched EM waves in the ion cyclotron frequency range, has been proposed. Furthermore, the radial position of mode conversion layers in a STPP geometry has been identified for various frequency regimes. This information is necessary for estimates of the mode damping and for further assessment of the feasibility

of the diagnostic techniques described in References [13, 40]. Further development of the 1-D model will include hot plasma effects, non-zero vertical magnetic field, magnetic geometry boundary layer effects and a realistic functional dependence of $k_{\|}$ on radius.

Chapter 3

Charged particle dynamics

Many features of plasma dynamics can be understood by investigating the motion of individual charged particles in electromagnetic fields. This has the advantage of providing clarity of the underlying physical processes, which are relevant for global plasma dynamics. The wave-particle interaction mechanisms relevant for high frequency waves, of interest in this thesis, are partly investigated in the LArge Plasma Device (LAPD) at the University of California, Los Angeles, USA. Clarification of the role of the electric field polarisation and wave propagation direction, with respect to the fast particles, are two main issues which have now been addressed on LAPD thanks to a collaboration with Prof. W. W. Heidbrink and are presented here.

3.1 Unbounded motion in an electromagnetic field

The Lorentz force law governs the motion of a charged particle in an electromagnetic field, leading to equations of motion in the form

$$\frac{d\mathbf{v}}{dt} = \frac{q}{m}\left(\mathbf{E} + \mathbf{v} \times \mathbf{B}\right) \tag{3.1a}$$

$$\frac{d\mathbf{r}}{dt} = \mathbf{v} \tag{3.1b}$$

where q, m are the charge and mass of the particle respectively.

3.1.1 Equilibrium

In the absence of a magnetic field, particles move in straight lines and analysing their motion is straightforward. However, in many plasma environments, specifically those of interest to this thesis, the motion of interest is subject to a background equilibrium magnetic field $\mathbf{B_0}$. In this equilibrium case the motion described by Eq 3.1 results in helical trajectories with a constant 'Larmor' radius (ρ) centred about a magnetic field line (the guiding centre). In Cartesian geometry with $\mathbf{B_0} = B_0\mathbf{e_z}$ the orbit can be represented as

$$\mathbf{r_0}(t) = \begin{pmatrix} x_0 + \rho\left(\sin\phi(t) - \sin\phi_0\right) \\ y_0 - \rho\left(\cos\phi(t) - \cos\phi_0\right) \\ z_0 + v_\parallel t \end{pmatrix} \tag{3.2}$$

where $\rho = v_\perp/\omega_c$ is the Larmor radius, $\omega_c = qB_0/m$ is the cyclotron frequency, $\phi(t) = \phi_0 + \omega_c t$ is the phase of gyration and $\perp$ and $\parallel$ denote perpendicular and parallel to the equilibrium magnetic field. In this case the equation for the 'guiding centre' of the particle motion is simply $\mathbf{r_g} = (x_0 - \rho\sin\phi_0, y_0 + \rho\cos\phi_0, z)$ as can be seen in Fig 3.1.

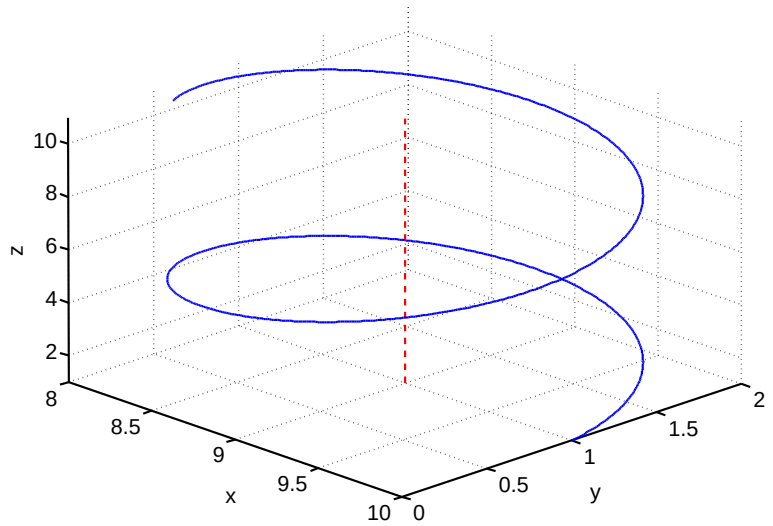

Figure 3.1: *Gyration motion described by Eq 3.2 (blue) and the corresponding guiding centre (red) for* $(x_0, y_0, z_0) = (10, 1, 1)$, $v_\parallel = 1$, $\omega_c = 1$, $\phi_0 = \pi/2$.

3.1.2 Motion in a wave field

The electric field of a plane electromagnetic wave can be written as

$$E_i\left(\mathbf{r},t\right)=\mathrm{Re}\left\{E_i e^{i\psi_i(\mathbf{r},t)}\right\} \tag{3.3}$$

where i represents the coordinates x,y,z, $\psi_i\left(\mathbf{r},t\right)=\mathbf{k}\cdot\mathbf{r}-\omega t+\psi_i^{(0)}$ and without loss of generality $\mathbf{k}=\left(k_\perp,0,k_\parallel\right)$. Faraday's law can then be utilised to express the perturbed magnetic field $\mathbf{B}$ in terms of the electric field $\mathbf{E}$ and, upon operating on Eq 3.1a with $\mathbf{b}\times\left(\mathbf{v}\times\mathbf{b}\right)\cdot$ and $\mathbf{b}\left(\mathbf{v}\cdot\mathbf{b}\right)\cdot$ separately (with $\mathbf{b}=\mathbf{B}/\left|\mathbf{B}\right|$), the evolution of the particle's energy ($\mathscr{E}$) can be described (in straight field line geometry) by [41]

$$\frac{d\mathscr{E}_\perp}{dt}=q\left\{\mathbf{E}_\perp\cdot\mathbf{v}_\perp+\frac{1}{\omega}\left[\mathbf{k}_\perp\cdot\mathbf{v}_\perp\left(E_\parallel v_\parallel\right)-\left(k_\parallel v_\parallel\right)\mathbf{E}_\perp\cdot\mathbf{v}_\perp\right]\right\} \tag{3.4a}$$

$$\frac{d\mathscr{E}_\parallel}{dt}=q\left\{\mathbf{E}_\parallel\cdot\mathbf{v}_\parallel-\frac{1}{\omega}\left[\mathbf{k}_\perp\cdot\mathbf{v}_\perp\left(E_\parallel v_\parallel\right)-\left(k_\parallel v_\parallel\right)\mathbf{E}_\perp\cdot\mathbf{v}_\perp\right]\right\}. \tag{3.4b}$$

From Eq 3.4 the energy change for each component ($\perp,\parallel$) can be seen to be a combination of the work done by the wave electric field (first terms) and a transfer of energy between components via the magnetic field (other terms). It should be noted that it has been implicitly assumed that the wave is a perturbation of the equilibrium system so that the notion of $\perp$ and $\parallel$ still make sense. In general the amount and direction of the energy exchange between a particle and a wave as described in Eq 3.4, over a wave period, depends on the the initial phase of the wave $\psi_i^{(0)}$ and the evolution of the wave phase as seen by the moving particle. In the event that the particle experiences the wave at a constant phase, energy is most effectively transferred between the particle and the wave. This concept is known as wave-particle resonance and will be discussed in the following section.

3.1.3 Wave-particle resonance

For a particle to experience a wave field at a constant phase, Eq 3.3 implies

$$\frac{d\psi_i}{dt}=\frac{d}{dt}\left(\mathbf{k}\cdot\mathbf{r}-\omega t+\psi_i^{(0)}\right)=0, \tag{3.5}$$

i.e. in the frame of reference of the moving particle the phase is stationary. Physically this statement ensures that the particle 'sees' a constant electric field and hence is

accelerated or decelerated for a large fraction of the wave period. By using the coordinates of the gyrating particle from Eq 3.2 but centred about the guiding centre of the Larmor orbit, the wave in Eq 3.3 can be re-expressed as a sum of helical waves using $\exp(i\xi\sin\phi) = \sum_{l=-\infty}^{\infty} J_l(\xi)\exp(il\phi)$ [41]

$$E \sim e^{i\left(k_\perp x + k_\parallel z - \omega t + \psi_i^{(0)}\right)} = \sum_{l=-\infty}^{\infty} J_l(\xi)\, e^{i\left(l\varphi + k_\parallel z - \omega t + \psi_i^{(0)}\right)} \tag{3.6}$$

where J_l is the Bessel function of order l and $\xi = k_\perp \rho$. Physically the plane wave has been decomposed into partial waves each with amplitude $J_l(\xi)$ which propagate along and rotate about the z direction (the guiding centre of the unperturbed particle orbit). The condition for stationary phase as in Eq 3.5 then leads to the following resonance condition [41]

$$\omega - k_\parallel v_\parallel - l\omega_c = 0. \tag{3.7}$$

For ions, $l = 1, 0, -1$ represent the Doppler shifted cyclotron resonance, the Landau resonance and the anomalous Doppler shifted cyclotron resonance respectively (n.b for electrons ω_c is negative so the sign of l must change).

3.1.4 Energy exchange

By substituting the motion of the unperturbed particle trajectory from Eq 3.2 directly into Eq 3.3, Eq 3.4 is averaged over a wave period and the average rate of change of energy of the particle then takes the form [41]

$$\left\langle \frac{d\mathscr{E}_\perp}{dt} \right\rangle = q\frac{\omega - k_\parallel v_\parallel}{\omega}\mathbb{E}_l \tag{3.8a}$$

$$\left\langle \frac{d\mathscr{E}_\parallel}{dt} \right\rangle = q\frac{k_\parallel v_\parallel}{\omega}\mathbb{E}_l \tag{3.8b}$$

where

$$\mathbb{E}_l = v_\perp E_{-,l} + v_\perp E_{+,l} + v_\parallel E_{\parallel,l} \tag{3.9}$$

$$E_{\mp,l} = \frac{1}{2}\left(E_x \sin\psi_{x,l}^{(0)} \mp E_y \cos\psi_{y,l}^{(0)}\right) J_{-l\mp1}(\xi) \tag{3.10a}$$

$$E_{\parallel,l} = E_z \sin\psi_{x,l}^{(0)} J_{-l}(\xi) \tag{3.10b}$$

and $\psi_{i,l} = \psi_i^{(0)} + \mathbf{k}\cdot\mathbf{r_0} - \xi\sin\phi_0 - l\phi_0$. Physically $E_\mp$ represent the parts of the wave electric field that rotate in a right and left hand sense respectively. It is instructive

to consider the case of ion motion with a small Larmor radius so that $\xi \ll 1$. In this case the Bessel functions can be expanded as $J_l \approx (1/l!)\,(\xi/2)^l$ and the lowest order Bessel functions are the largest. Using this approximation the effects of the different resonances can be most clearly understood.

3.1.5 Landau resonance $l = 0$

For $l = 0$ (Landau resonance) Eq 3.8a is identically zero, and only the parallel energy is affected by the wave. The velocity of a particle undergoing this resonance must match the phase speed of the wave $v_\phi = \omega/k_\parallel$ in the direction parallel to the magnetic field. It can be understood that effective energy transfer will occur in this case since the particle will experience a constant electric field as the wave is 'stationary' from the perspective of the particle. The dominant contribution arises from the parallel electric field $E_\parallel$ and the $E_\mp$ contributions are a finite Larmor radius (FLR) correction. By this it is meant that the largest term in Eq 3.9 arises from $l = 0$ in $E_{\parallel,l}$ i.e the zerosth order Bessel function, and the perpendicular electric field enters as a first order Bessel function which is smaller. It should be noted that in curvilinear magnetic geometries the parallel electric field is very small and it is the perpendicular electric field which provides the dominant contribution via particle drifts [42].

3.1.6 The Doppler shifted cyclotron resonance $l = 1$

For $l = 1$ (Doppler resonance) the dominant term in Eq 3.9 is the E_+ i.e the left hand polarisation and there are finite Larmor orbit corrections from $E_\parallel$ and E_-. For a particle undergoing this particular resonance, the parallel motion causes a Doppler shift of the wave frequency from the laboratory frequency to the particle's cyclotron frequency. Although the particle will experience the $l = 1$ partial wave at a constant phase, in the laboratory frame of reference the particle is not in overall phase with the total wave. As the particle gyrates, the electric field vector rotates in such a way that the particle experiences a prolonged and coherent interaction along its orbit as shown in Fig 3.2. In this way one can understand why the dominant contribution

to the energy exchange is due to the left hand polarised part of the electric field, since the ions gyrate in a left handed sense around the magnetic field lines.

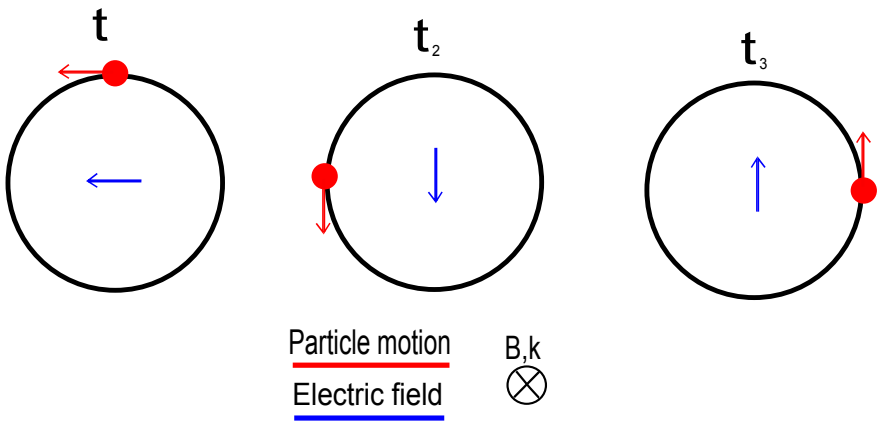

Figure 3.2: *Schematic of the cyclotron resonance for the $l = 1$ case with a left hand polarised wave.*

For the Doppler resonance

$$v_{\parallel} = \frac{\omega - \omega_c}{k_{\parallel}}, \tag{3.11}$$

from which it can be seen that for co-propagating waves and particles $\left(v_{\parallel}/\left|v_{\parallel}\right| = k_{\parallel}/\left|k_{\parallel}\right|\right)$ the particles's speed must not exceed the phase speed of the wave. This can also be re-expressed as the frequency of the wave in the lab frame must exceed the cyclotron frequency of the particle. For counter propagating waves and particles $\left(v_{\parallel}/\left|v_{\parallel}\right| \neq k_{\parallel}/\left|k_{\parallel}\right|\right)$, the resonance condition shows that the wave frequency must not exceed the cyclotron frequency of the particle.

3.1.7 The anomalous Doppler shifted cyclotron resonance $l = -1$

For $l = -1$ (anomalous Doppler resonance) the dominant term in Eq 3.9 is the E_{-} i.e the right hand polarisation, which is in contrast to the Doppler case. By constructing the anomalous Doppler equivalent version of Eq 3.11

$$v_{\parallel} = \frac{\omega + \omega_c}{k_{\parallel}}, \tag{3.12}$$

it can immediately be seen that 1) this particular resonance can only occur for co-propagating waves and particles and 2) the particles's speed must exceed the wave

phase speed in contrast to the Doppler case. The breaching of the phase speed has an important consequence as can be observed in Fig 3.3. Consider a right hand polarised wave in the lab frame. A 'sub' particle moving with the wave will experience wave crests C, B and A, which is right handed, and likewise for a particle moving against the wave. This is the Doppler case, and since the wave is 'seen' to be right hand polarised there will be little energy transfer. However for a 'super' particle the opposite is true, A, B and then C are traversed, which is left handed from the particle's perspective. From this one can understand why the E_- has the greatest contribution for this resonance.

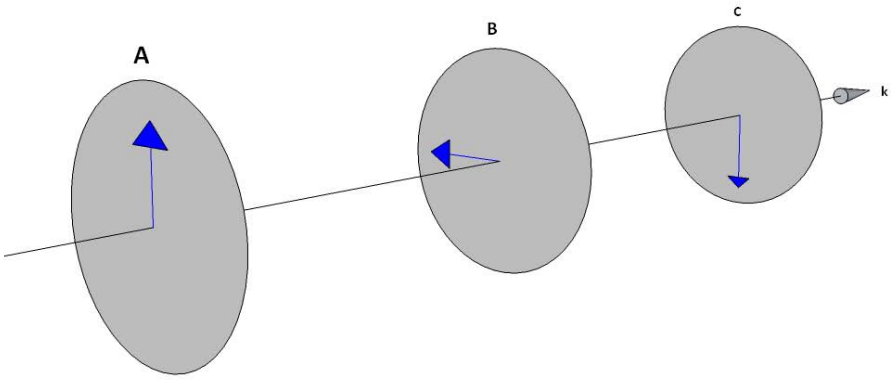

Figure 3.3: *Schematic of the wave crests of a right hand polarised wave (grey) with the rotating electric field vector in blue*

3.1.8 Resonance in an Alfvén wave field

For the case of low frequency ($\omega \ll \omega_{pe}, \omega_{pi}$) transverse electromagnetic waves in a plasma, the dispersion relation for the waves propagating parallel to the equilibrium field separates into 'shear' and 'compressional' Alfvén waves (SAWs and CAEs) as described in chapter 2. The dominant polarisation of the electric field for the shear wave is left hand polarised and the compressional wave is right hand polarised [28], which naturally leads to a discussion of how gyrating ions can interact with these waves. From sections 3.1.6 and 3.1.7 it can be seen that, to zeroth order in the ion Larmor radius, the shear waves interact strongly with ions via the Doppler shifted cyclotron resonance and the compressional waves interact strongly with ions via the

anomalous Doppler shifted cyclotron resonance. This is however only zeroth order, weak interactions via the other resonances are possible and so the all the cyclotron interactions with Alfvén waves are summarised in Figure 3.4

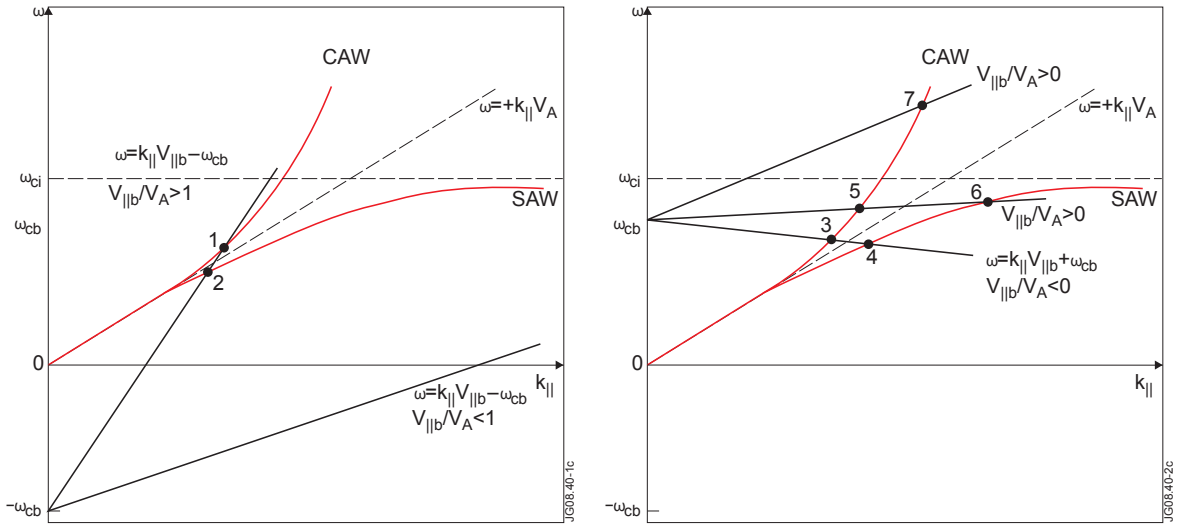

Figure 3.4: *Dispersion relation for the Alfvén waves with the anomalous Doppler (left) and Doppler (right) shifted cyclotron resonance condition superposed.*

Fig 3.4 (left) shows that (points 1 and 2) high velocity particles can experience the anomalous Doppler resonance with both SAWs and CAWs, noting that the most effective resonance is with the CAWs. Low velocity particles can theoretically experience a resonance with SAWs, however in practice the parallel wavelengths associated with such a resonance are too small and kinetic damping usually prevents such waves from persisting [20]. The most striking feature for the anomalous case is that there exists a critical velocity below which no resonance is possible with the CAWs. By assuming that $v_{\mathrm{A}} \ll c$, this critical velocity can be expressed as (see appendix A)

$$\frac{v_{\parallel}^{\mathrm{crit}}}{v_{\mathrm{A}}} \approx \frac{3}{2}\sqrt{1+\frac{2\omega_{cb}}{\omega_{ci}}} \tag{3.13}$$

For the case when the bulk ion species and the fast particles are the same this equation is exact and the threshold reduces to $v_{\parallel}^{\mathrm{crit}}/v_{\mathrm{A}} \approx 2.6$.

For the Doppler case Fig 3.4 (right), with counter propagating ions and waves, a resonance with CAWs and SAWs is possible (points 3 and 4) noting that the most effective resonance is with the SAWs. If the bulk plasma and the fast ion species

are identical then no resonance is possible with SAWs via the Doppler resonance for co propagating particles. However, unlike the anomalous Doppler resonance, the addition of a particle species different from that of the bulk plasma creates a window in frequency where the SAWs may resonate via the Doppler resonance for co-propagation (point 6).

3.2 Resonance experiments on LAPD

Many of the theoretical aspects of wave-particle resonance outlined in section 3.1 can be investigated experimentally by using a cold plasma and injecting a low density energetic beam of ions. Since many aspects of plasma instabilities depend on the existence and character of the wave particle resonances, this subject warrants a more complete experimental investigation. Of particular interest for this thesis is the role that the electric field polarisation and wave propagation direction have in the wave particle interaction. Specifically, it is of interest to show experimentally that 1) ions do not effectively exchange energy with right hand polarised waves via the Doppler shifted cyclotron resonance and 2) that counter propagating waves and particles can indeed exchange energy via the Doppler resonance.

A device of particular significance in the field of fundamental wave particle interactions is the LArge Plasma Device (LAPD) [17] at the University of California, Los Angeles (UCLA). LAPD is a large cylindrical device with an axial equilibrium magnetic field, produced by the external coils, shown in Fig 3.5. Due to the finite radius of LAPD, a minimum value of $k_\perp$ has to be taken into account in comparison with the infinite homogeneous case shown in Fig 3.4. Notwithstanding this, LAPD is perfectly suited to wave particle interaction studies. The plasma is created using a hot plate (the cathode) made of barium oxide, thermionic emission of electrons from this plate ionises the surrounding gas creating a plasma. The main plasma pulse lasts for approximately 10ms and the turnover time between pulses is 1s. This high rep rate enables LAPD to acquire large data sets over which averaging can be performed to obtain very robust measurements.

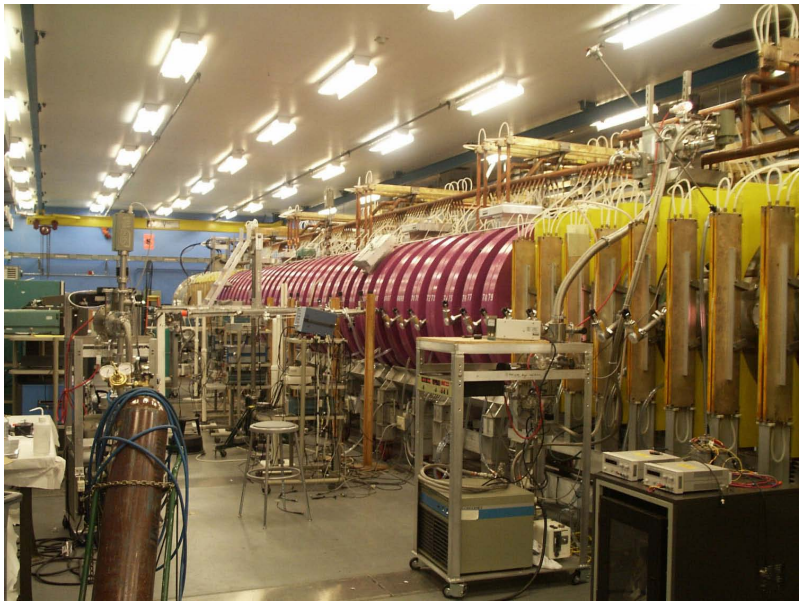

Figure 3.5: *The LAPD experimental machine. The pink and yellow coils produce the axial magnetic field.*

3.2.1 Wave-particle interaction set-up

To investigate wave-particle resonances in LAPD an antenna designed to launch circularly polarised Alfvén waves is placed into the helium plasma as shown in Figs 3.6 and 3.7. A low density ($n_b \sim 5 \times 10^{14}\mathrm{m}^{-3}$) energetic Lithium source (600eV) is then submersed in a 5eV helium plasma ($n_i \sim 2.5 \times 10^{18}\mathrm{m}^{-3}$) at an angle of 49.3° to the equilibrium field to avoid damage of the Lithium source from the fast streaming electrons produced by the cathode. After being subject to the Alfvén wave field the fast particles are collected using a fast ion analyser [43]. By biassing the collector is such a way as to reject any thermal particles, the current produced by the fast particles then gives a measure of the the density of Lithium ions at the collector location. This collector can be placed either side of the Alfvén wave source to investigate co and counter propagating waves and particles. In this experimental campaign the equilibrium magnetic field in the core of the machine was kept at $B_0 = 0.12T$ and the bulk cyclotron frequency at $\omega_{ci} = 475\mathrm{kHz}$.

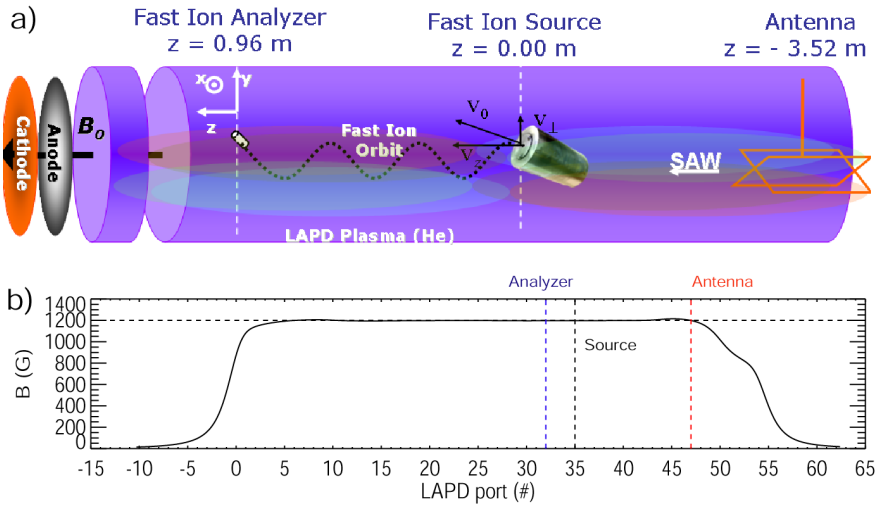

Figure 3.6: *Schematic of the The LAPD experimental set-up, similar to Ref [43].*

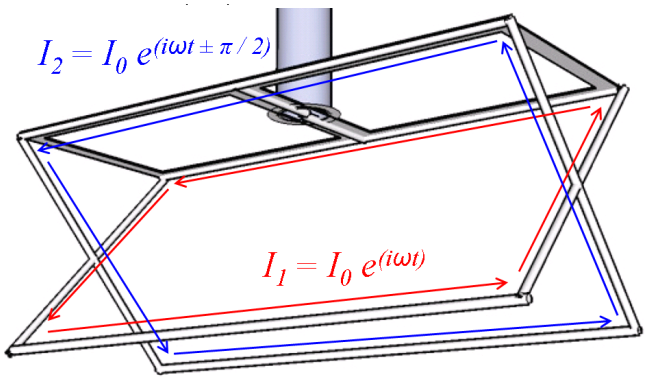

Figure 3.7: *Schematic of the the LAPD SAW antenna. Left and right hand polarised SAWs can be produced.*

3.2.2 Alfvén waves in LAPD

In order to launch Alfvén waves from the antenna shown in Fig 3.7 an alternating current is passed through each of the legs and phased locked by $\pi/2$ to produce a near circularly polarised EM wave. For a single Alfvénic pulse in LAPD the finite axial extent does not affect the wave propagation. However the finite radial extent forces a maximum perpendicular wavelength (or minimum $k_\perp$) on the order of the plasma diameter. Since the CAW dispersion relation depends on the total wave number $k = \sqrt{(k_\perp^2 + k_\parallel^2)}$ (see Eq 2.10), the existence of a minimum $k_\perp$ sets a minimum frequency termed the wave guide cut-off. For typical LAPD parameters this cut-off is above the ion cyclotron frequency for the background plasma in the

Whistler range, preventing the investigation of compressional waves. In LAPD it is therefore only possible to study shear Alfvén waves, and so the antenna is aligned with the equilibrium magnetic field $\mathbf{B_0}$ so that the perturbations $\delta\mathbf{B}$ produced are of shear Alfvén type i.e $\delta\mathbf{B} \perp \mathbf{B_0}$.

In actual fact the ideal dispersion relation of Eq 2.9 is an oversimplification for SAWs in LAPD. When FLR effects are included the dispersion relation becomes [44]

$$\omega^2/k_\parallel^2 = \mathrm{v}_A^2\left(1 - \bar{\omega}^2 + k_\perp^2\rho_s^2\right) \tag{3.14}$$

where $\bar{\omega} = \omega/\omega_{ci}$ and $\rho_s = c_s/\omega_{ci}$ where $c_s = \sqrt{T_e/m_i}$ is the ion sound speed. Unlike SAWs in an infinite plasma whose wave polarisation is left hand polarsied, those launched from an antenna with a finite extent in a finite plasma can in fact display both types of polarisation over the profile of the wave as can be seen in Fig 3.8. This indicates that wave-particle interactions with Alfvén waves in bounded geometries may require consideration of multiple wave polarisations.

3.2.3 The Doppler shifted cyclotron resonance with SAWs in LAPD

The fast particle interactions on LAPD use a Lithium source that emits at a maximum energy of 600eV. At this energy the regimes accessible for effective cyclotron interaction are the Doppler resonances 3,4,5 and 6 of Figure 3.4. To access the anomalous Doppler resonance at this particle energy the magnetic field and density would have to be modified beyond the tolerances of the machine.

For co-propagating waves and particles in LAPD the Doppler shifted cyclotron resonance condition is satisfied for $\bar{\omega} = 0.63$, $k_\parallel = 2.68\mathrm{m}^{-1}$, $v_\parallel = 8.8\times10^4\mathrm{ms}^{-1}$. The Lithium source is placed 3 ports away from the particle detector in the midplane of the plasma cross section. The particles traverse orbits shown in Fig 3.8. The particles experience the resonant field and are either accelerated or decelerated as described in the preceding sections. This effect manifests itself as a radial and angular spreading in the detector plane as shown in Fig 3.9.

The radial spreading results from the increase or decrease in perpendicular energy as a result of the circularly polarised electric field of the Alfvén wave. The

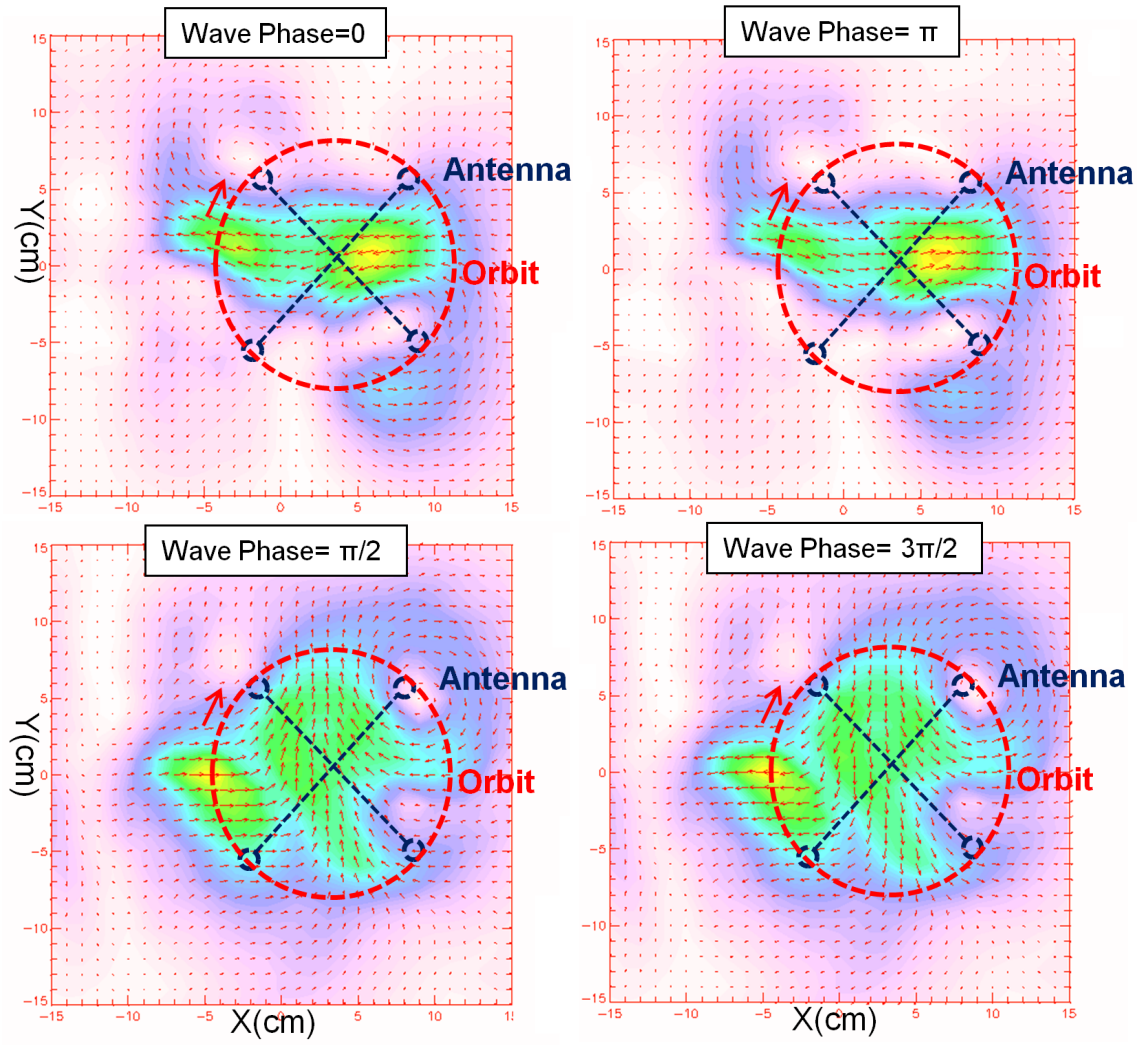

Figure 3.8: *Contours and vectors of the perturbed magnetic field of a SAW in LAPD. The central and outer regions show reversed polarisation.*

angular spreading arises due to the initial spread in velocities at the Lithium source. The initially faster particles do not complete as many Larmor orbits before being detected, and as a result these particles are seen lower in the detector plane. The slower particles are shown higher in the plane. This however is not the only source of angular spreading, the other contribution comes from the $\mathbf{v} \times \delta\mathbf{B}$ force the particle experiences from the resonant Alfvén field. A quantitative analysis, which measures a weighted average [43] of the spread over the detector plane, shows that the particles do indeed undergo significant spreading in radius when the wave field is on, as expected (Fig 3.10 (a)).

By reversing the polarisation of the Alfvén wave it can be seen that the parti-

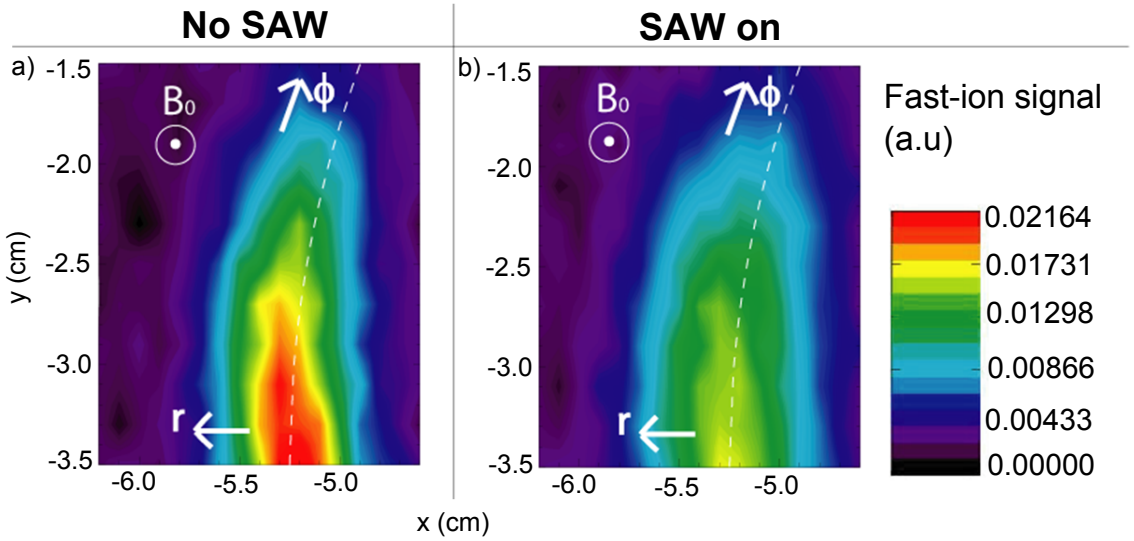

Figure 3.9: *Contour plot of the inferred density (from the detector current) of Lithium particles in the detector plane 3 ports away from the Lithium source. The detector is placed at a position in the plane where 10 experiments are performed, this is then repeated for many points in the plane to produce the detector plane.*

cles do not undergo significant spreading as can be seen in Figure 3.10 (b). This is consistent with our understanding that, with right hand polarisation, the energy transfer from the wave to the ions is not as effective as with left hand polarisation. Fig 3.10 also shows evidence that this spreading is indeed due to the resonant interaction with the wave field and not due to the displacement of the magnetic field lines due to the Alfvén wave field.

Counter propagating beam ions were also seen to interact strongly with SAWs with $\bar{\omega} = 0.58$, $k_{\|} = 2.36\text{m}^{-1}$, $v_{\|} = 8.8 \times 10^4\text{ms}^{-1}$. Fig 3.11 indicates that radial spreading is occurring, however the experimental evidence is less striking than for co propagation as the beam profiles are significantly different. The most likely cause of this irregularity is poor performance of the Lithium source. The counter propagating experiments were performed at the end of the campaign when the source reliability had become low.

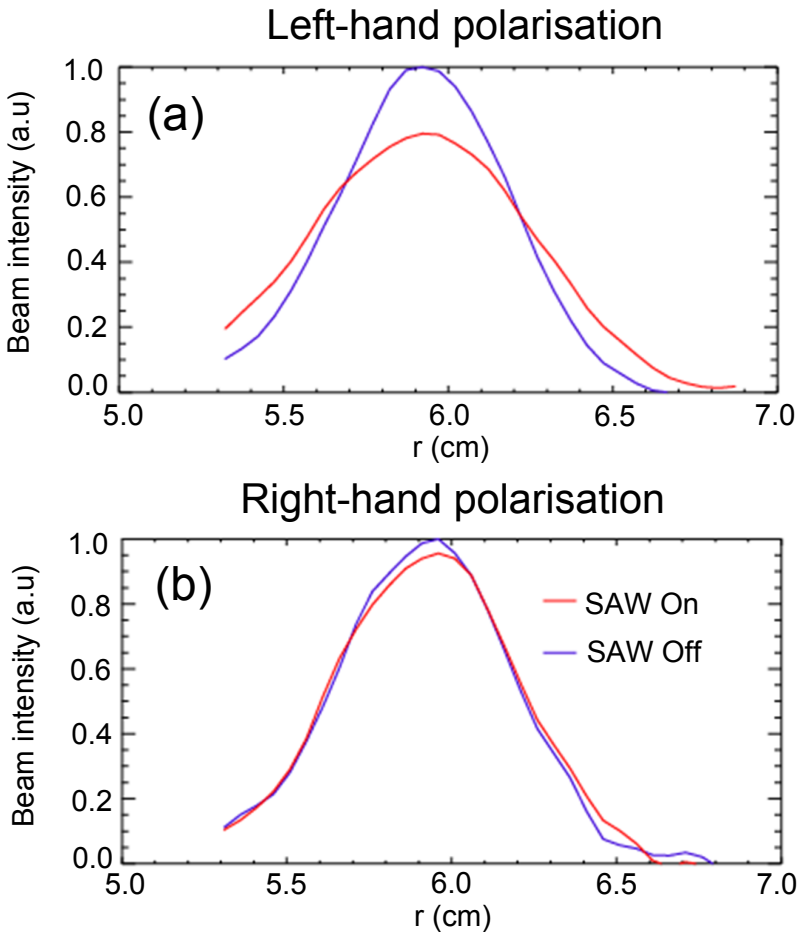

Figure 3.10: *Quantitative analysis of the radial spreading caused by the shear Alfvén wave field in the case of left and right hand polarised SAWs.*

3.3 Discussion

The theory of resonant interactions of waves and particles is well established and understood. However, the experimental verification of the resonant interaction between counter propagating waves and particles has not, until now, been performed. Likewise, the confirmation that left hand gyrating ions and right hand polarised waves do not significantly interact has now been successfully demonstrated. The study of Alfvén waves in the bounded geometry of the LAPD device has also led to the observation that multiple polarisations can be present over the wave profile, indicating that multiple polarisations might need to considered for Alfvén waves in other devices such as tokamaks.

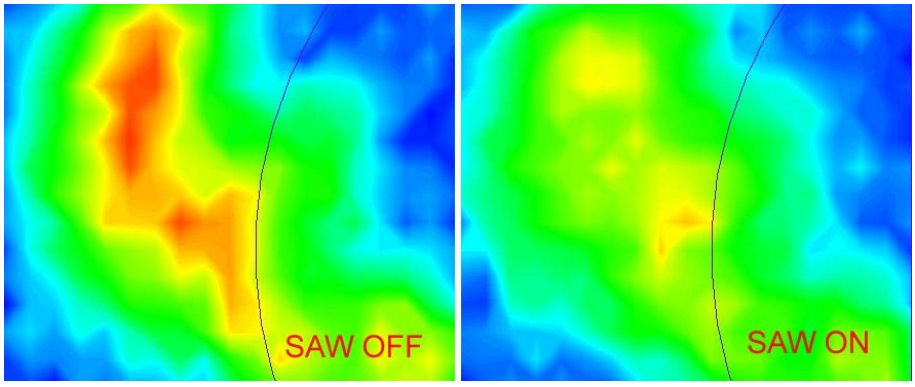

Figure 3.11: *Contour plot of the inferred density (from the detector current) of Lithium particles in the detector plane 3 ports away from the Lithium source with counter propagating waves and particles. The detector is placed at a position in the plane where 10 experiments are performed, this is then repeated for many points in the plane to produce the detector plane.*

Chapter 4

High frequency Alfvén Eigenmodes on MAST

MAST is a small aspect ratio spherical tokamak with typical major and minor radii of $R_0 = 0.86$m and $a = 0.6$m respectively. Looking from above the machine, the equilibrium toroidal magnetic field (B_ϕ) is in the clockwise direction, and the plasma current (I_p) and NBI are in the anti-clockwise direction as shown in Fig 4.1.

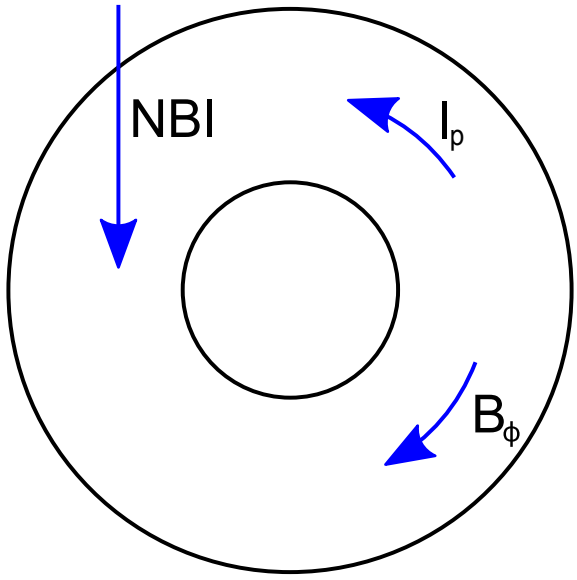

Figure 4.1: *Schematic of the MAST experimental set-up*

For the MAST discharges shown in this thesis, the deuterium plasma is heated firstly by the the plasma current and subsequently by a beam of deuterium ions produced

by neutral beam injection (NBI) in the same direction as the plasma current (co-I_p) as shown in Fig 4.1. The beam is injected with a maximum energy component of $E_{\mathrm{NBI}} \approx 65\mathrm{keV}$ and also with weaker components at $E_{\mathrm{NBI}}/2$ and $E_{\mathrm{NBI}}/3$ [45]. The typical plasma parameters for this series of discharges are $T_e \approx T_i \approx 1\mathrm{keV}$, $n_e \approx 4 \times 10^{19}\mathrm{m}^{-3}$, $B_0 \approx 0.45T$, $I_p \approx 700\mathrm{kA}$. Modes with frequencies comparable to the deuterium cyclotron frequency were previously, occasionally, observed on MAST [18], however a detailed study was not performed. A robust experimental scenario has now been successfully developed for a systematic study of high frequency modes on MAST [19] the results of which are presented in this chapter. Theoretical modelling of the mode behaviour is then investigated using the 1-D model developed in chapter 2 and the resonance conditions outlined in chapter 3.

4.1 Magnetic diagnostics on MAST

EM plasma instabilities can be observed externally on MAST via 'Mirnov' coils installed just outside the plasma, along the machine wall and the central rod. Each coil measures the loop voltage produced by the wave and hence the perturbed magnetic field ($\partial\delta\mathbf{B}/\partial t$) through Faraday's law. These coils are placed at intervals in the toroidal direction so that the wave propagation direction and toroidal mode number can be ascertained. Some of these coils are combined in sets of three mutually orthogonal coils providing information on the inter-relation between B_R, B_z, and B_ϕ (Fig 4.2). The Mirnov coils on MAST are designed to sample up to 10MHz, which is higher than the typical cyclotron frequency of $\sim 3\mathrm{MHz}$.

4.1.1 Digital processing

To reconstruct of a continuous signal using discrete samples the Nyquist-Shannon sampling theorem [46] must be used, which states that

If a function $x(t)$ contains no frequencies higher than B cycles per second, it is completely determined by giving its ordinates at a series of points spaced 1/(2B) seconds apart.

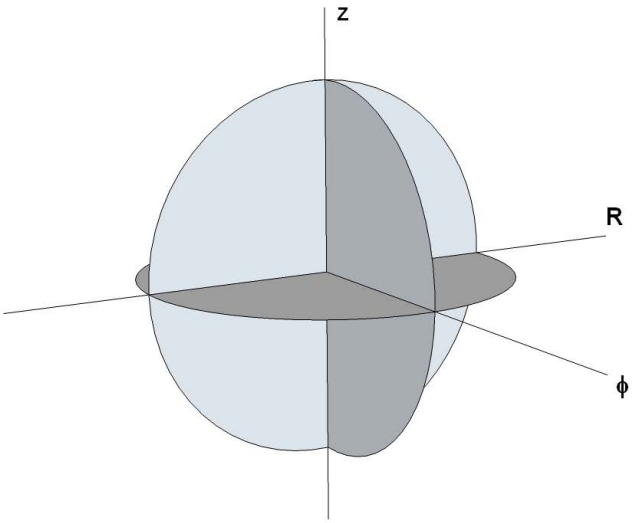

Figure 4.2: *Schematic of the internal configuration of a Mirnov coil*

This can also be interpreted as, given a sampling rate of f, only frequencies below the Nyquist frequency of $f/2$ can be unambiguously reconstructed from the signal, this can also be understood from Fig 4.3. So for the Mirnov coils on MAST the maximum frequency that can be unambiguously resolved is 5MHz.

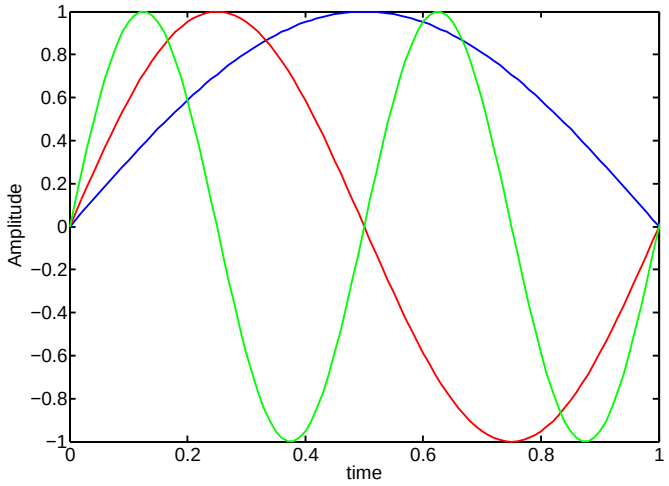

Figure 4.3: *Theoretical signals for a sampling rate of* $1Hz$*. The blue curve shows that the highest frequency detectable, unambiguously, is* $0.5Hz$*.*

A discrete Fast Fourier Transform (FFT) technique is applied to the magnetic signal to analyse the the temporal behaviour of the mode frequencies. A sliding window

technique is applied to the discrete sampled signal. Within this window a discrete Fourier transform is performed to reveal the spectrum of frequencies. By sliding the window along the time axis a spectrogram can be produced by overlapping each window as shown in Fig 4.4. Increasing the size of the FFT window increases the resolution in frequency but decreases that in time, and so this window must be carefully chosen to suit the frequency and time scales of interest.

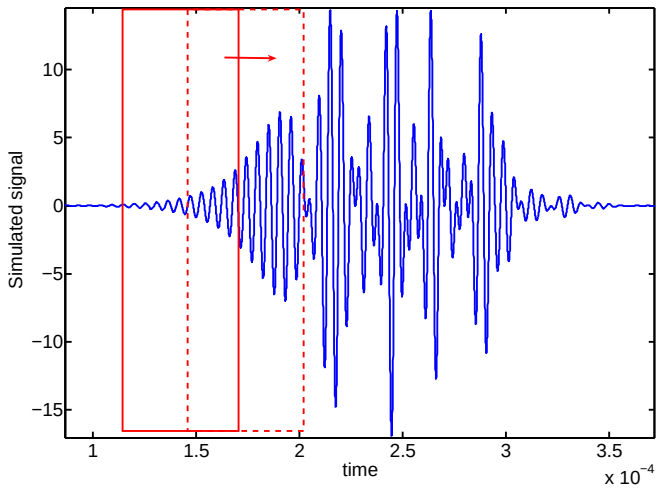

Figure 4.4: *Simulated signal (blue) and the time window (red, solid). The window slides along the time axis whilst overlapping with the previous window (red, dashed).*

4.2 Experimental observations

It was established on MAST that CAEs are most likely to occur in discharges with very flat q profiles, obtained by injecting two-step NBI into the plasma during the inductive current ramp-up phase. With co-I_p NBI heating, long lasting EM modes with $\omega \sim \omega_{cD}/3$ or so have been previously observed on MAST in both low confinement mode (L-mode) and high confinement mode (H-mode) as can be seen in Figure 4.5.

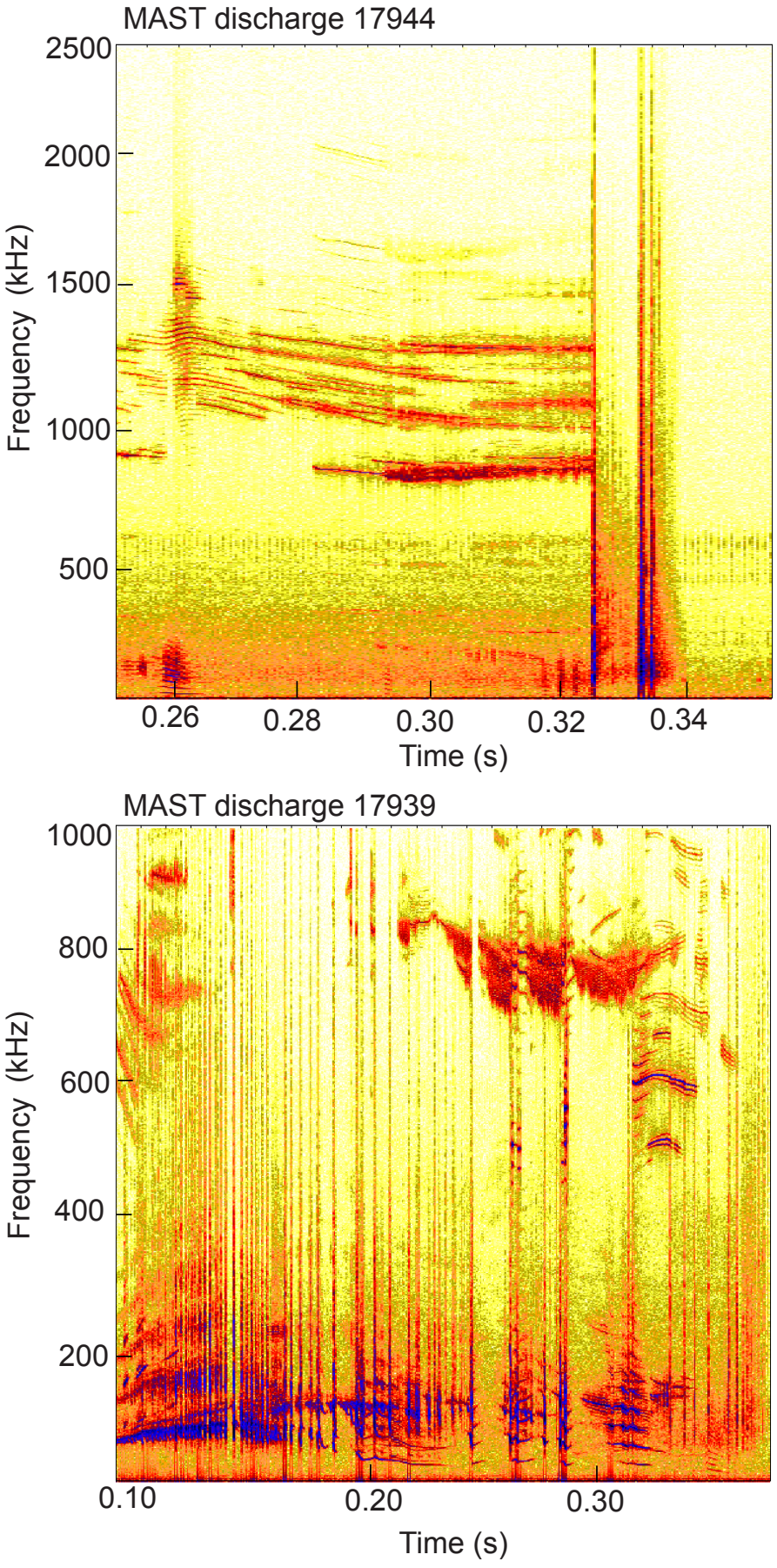

Figure 4.5: *Spectrogram of the high frequency magnetic activity from an L-mode (top) pulse (17944) and H-mode (bottom) pulse (17939).*

4.2.1 L-mode vs. H-mode

Due to changes in the vessel condition over time, it is necessary to check the robustness of the test pulses in Figure 4.5. A direct repeat of these pulses yields the spectrograms in Fig 4.6. The frequency range for the two cases are similar $\approx \omega_{cD}/3$ and the experimental scenarios are shown to be robust over multiple repeats and variations of these pulses.

4.2.2 Toroidal mode number analysis

The most striking feature of the high frequency modes observed on MAST is that almost all the modes are seen to propagate counter to the plasma current (and also the injected beam), i.e they mostly have negative toroidal mode numbers n as can be seen in Figs 4.8 and 4.9. The excitation of CAEs propagating counter to the injected ions posed a question (later studied on LAPD) about the efficiency of the Doppler resonance interaction between counter propagating waves and particles. In MAST the convention is that positive means anti-clockwise (from above), therefore a negative n mode propagates co-B_t and counter-I_p. From chapter 3 it can therefore be understood that the Doppler shifted cyclotron resonance condition is the appropriate wave particle interaction mechanism for these modes.

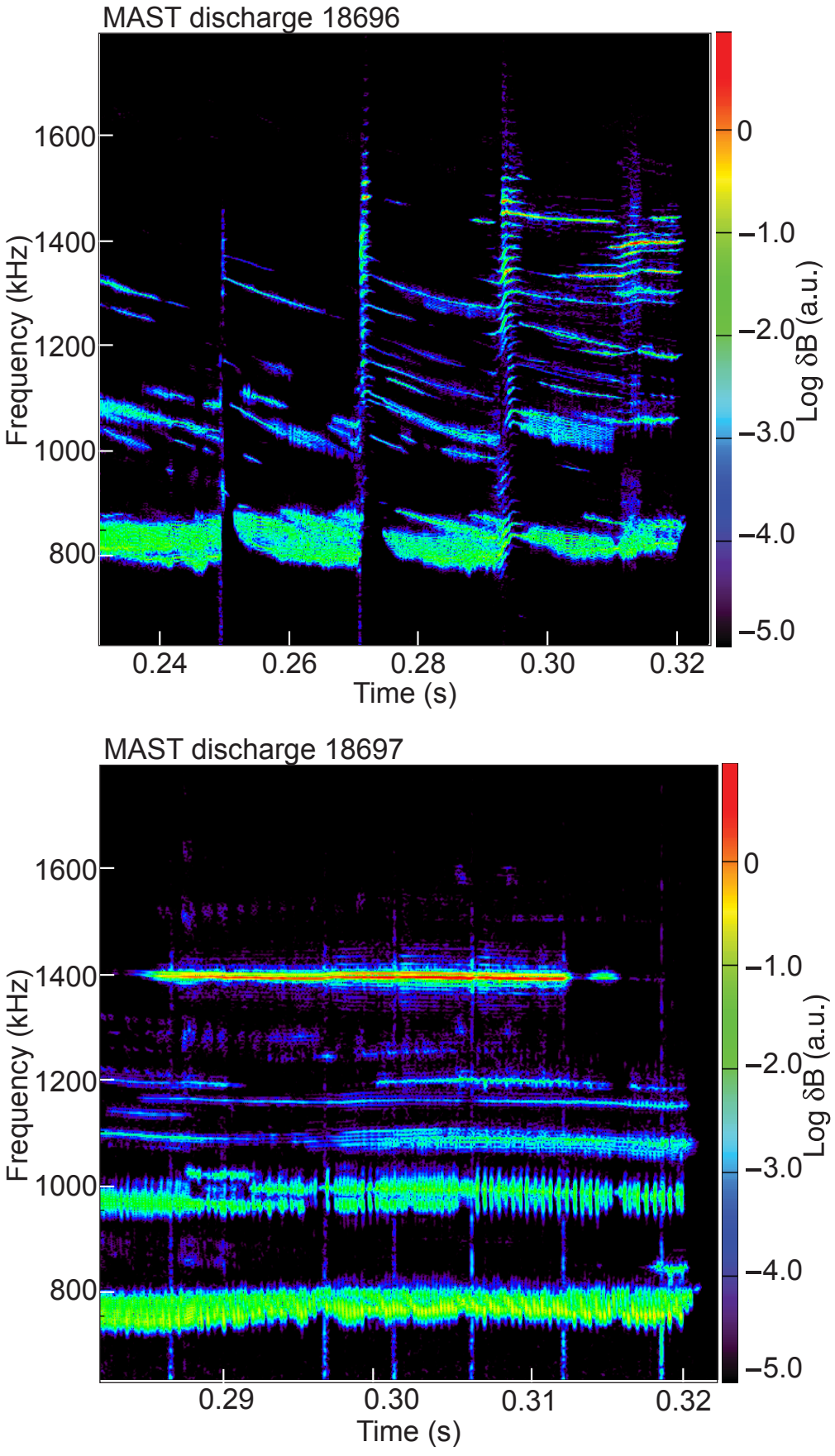

Figure 4.6: *Repeat of those pulses in Figure 4.5 showing the spectrograms for the L-mode (top) pulse (18696) case and H-mode (bottom) pulse (18697).*

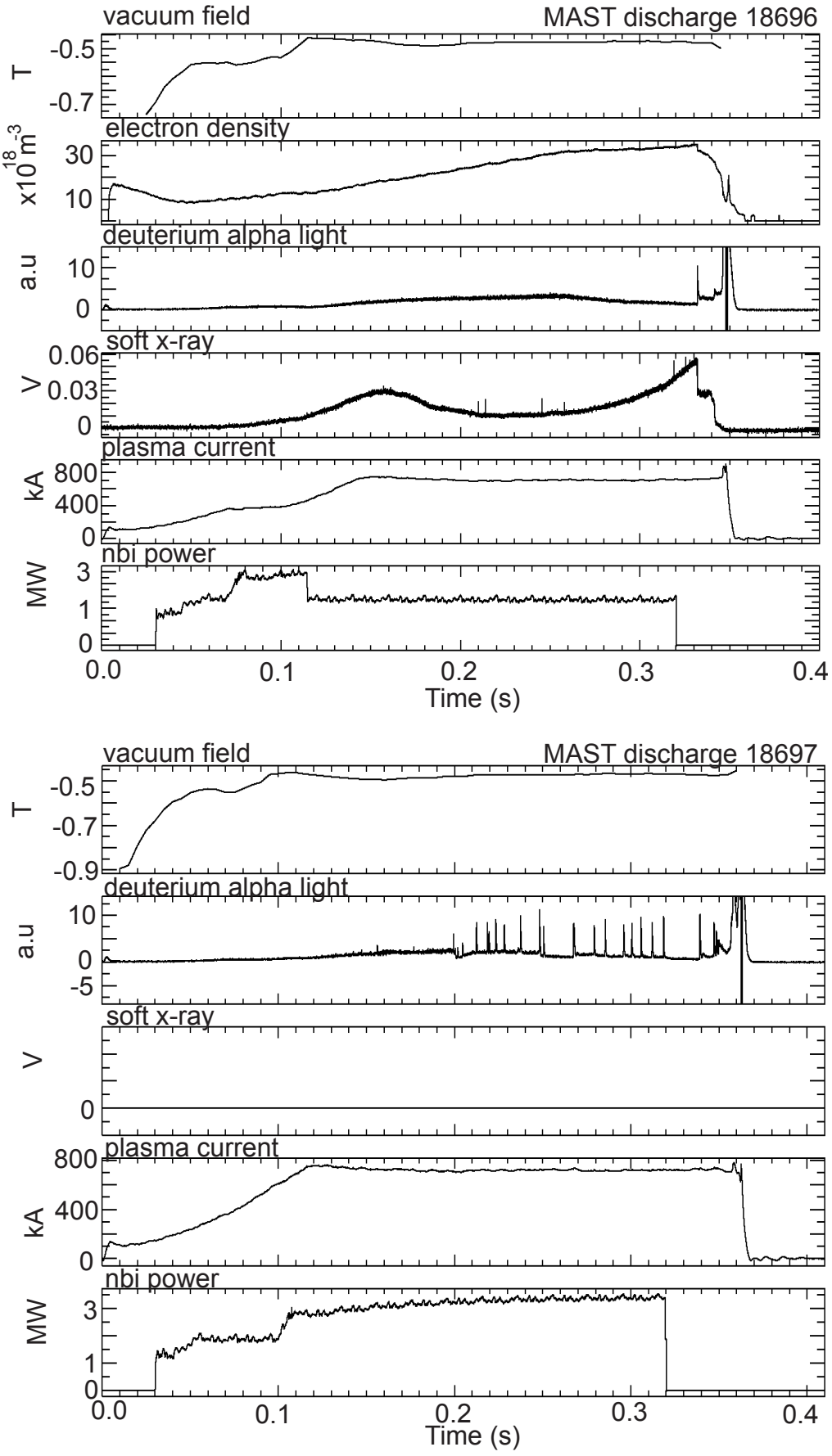

Figure 4.7: *Shows the evolution of the vacuum magnetic field, electron density, D_α light, soft X-ray, plasma current and total NBI power for Fig 4.6.*

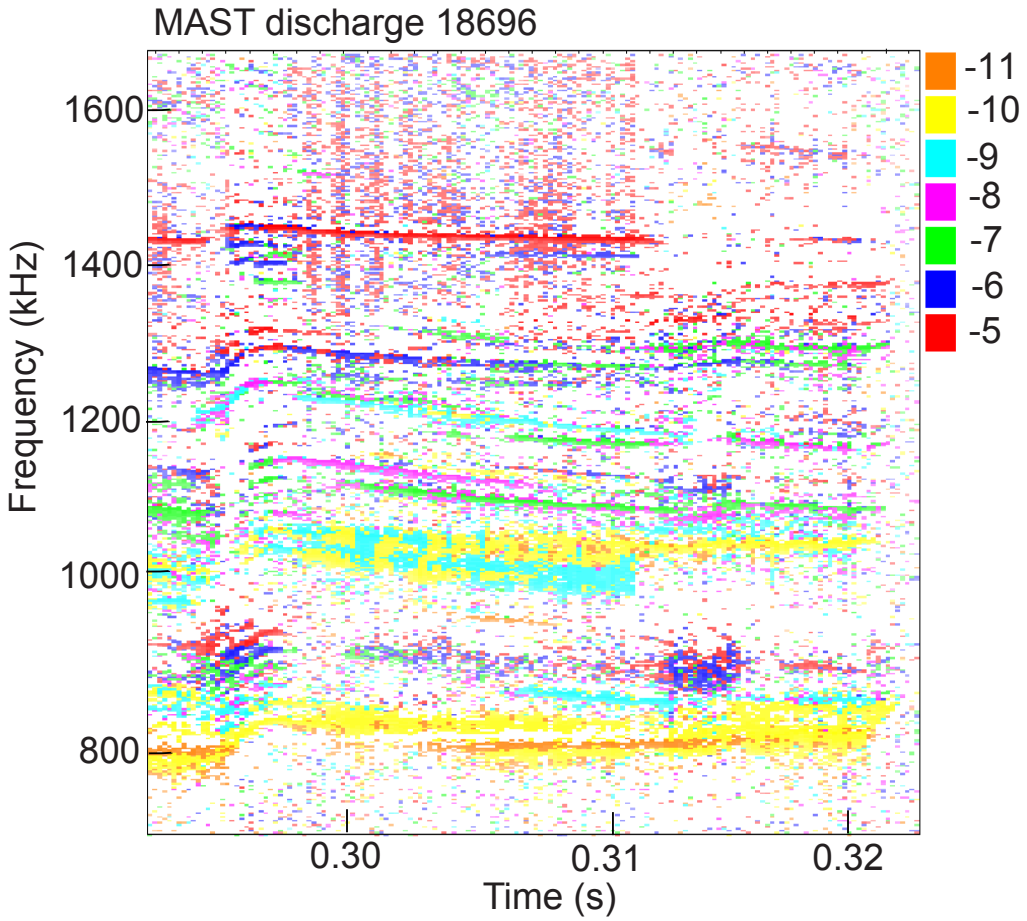

Figure 4.8: *Shows toroidal mode number (n) analysis for #18696. Here we see high negative mode numbers.*

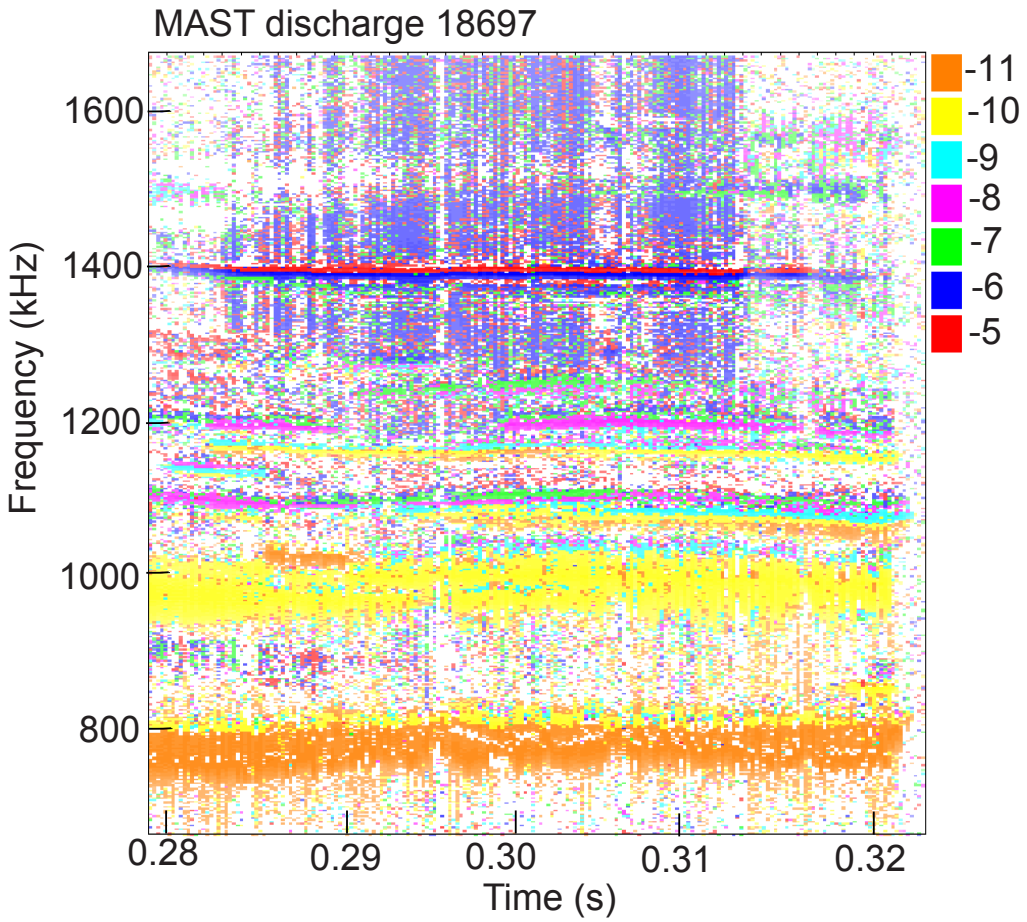

Figure 4.9: *Shows toroidal mode number (n) analysis for #18697. Here we see high negative mode numbers.*

It can also be seen that the modes decrease in frequency as $|n|$ increases. This feature is in contrast to most experimentally observed low frequency modes and also current theoretical predictions [15]. Small frequency splitting between successive mode numbers, for example in #18696, can be explained by toroidal rotation, since $f_{\mathrm{rot}}^{\mathrm{max}} \approx 19kHz$. Here modes with the same frequency but different n numbers will experience a Doppler shift due to the plasma rotation, so that in the laboratory reference frame these modes are split in frequency according to $f_{\mathrm{lab}} = f_{\mathrm{plas}} + nf_{\mathrm{rot}}$. However, rotation cannot explain frequency separations $\Delta f_{n=-5\rightarrow-6} \approx 150kHz$.

4.2.3 Simultaneous excitation of multiple mode classes

The simultaneous excitation of modes of different classes has also been observed in this series of discharges. From Fig 4.11 two types of mode are observed, those

whose frequency remains approximately constant in time and those whose frequency changes in time. A toroidal mode number analysis of pulse 18489 shows that these modes propagate in opposite directions as seen in Fig 4.12

4.2.4 Non-linear behaviour

The non-linear behaviour of fast particle driven modes has been extensively studied for low frequency modes in tokamak plasmas. Notable is the work by Berk and Breizman [25,26] which shows that non-linear effects can manifest as rapid frequency chirping. Such chirping has been observed readily in this campaign on high frequency beam driven instabilities, the most striking example of which can be seen in Fig 4.10 by zooming in on figure 4.6 (bottom).

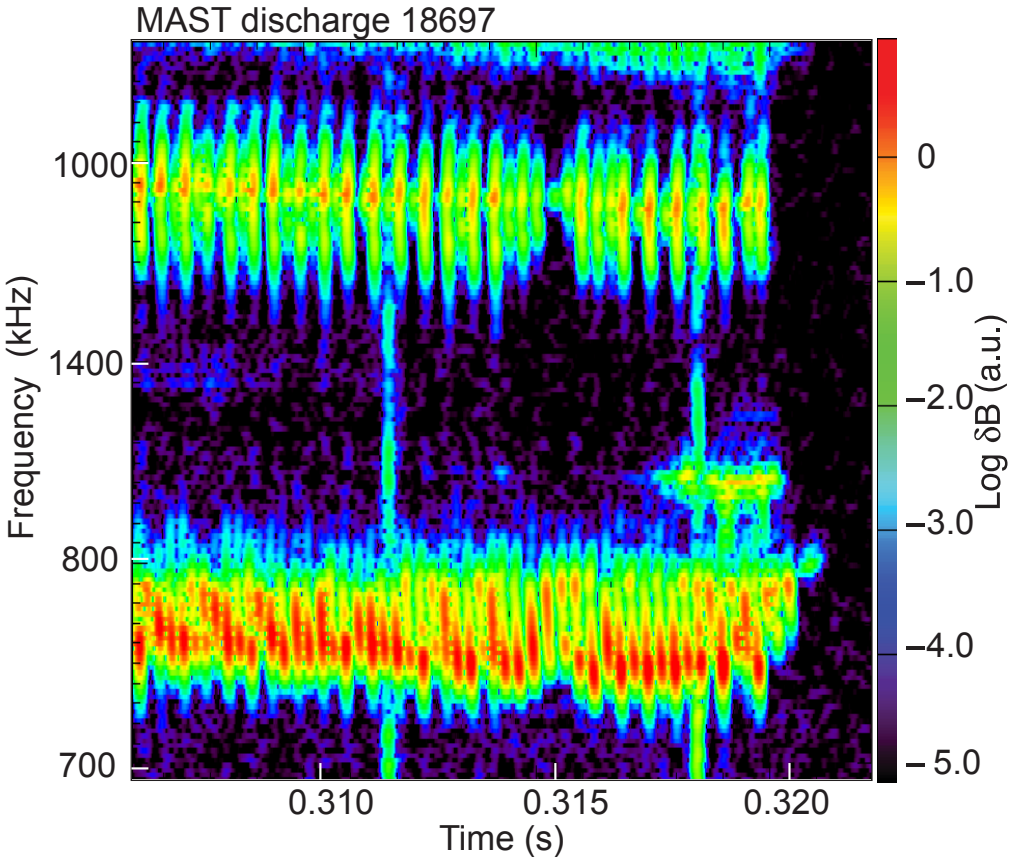

Figure 4.10: *A zoom of the spectrogram of #18697 in Figure 4.6 (bottom)*

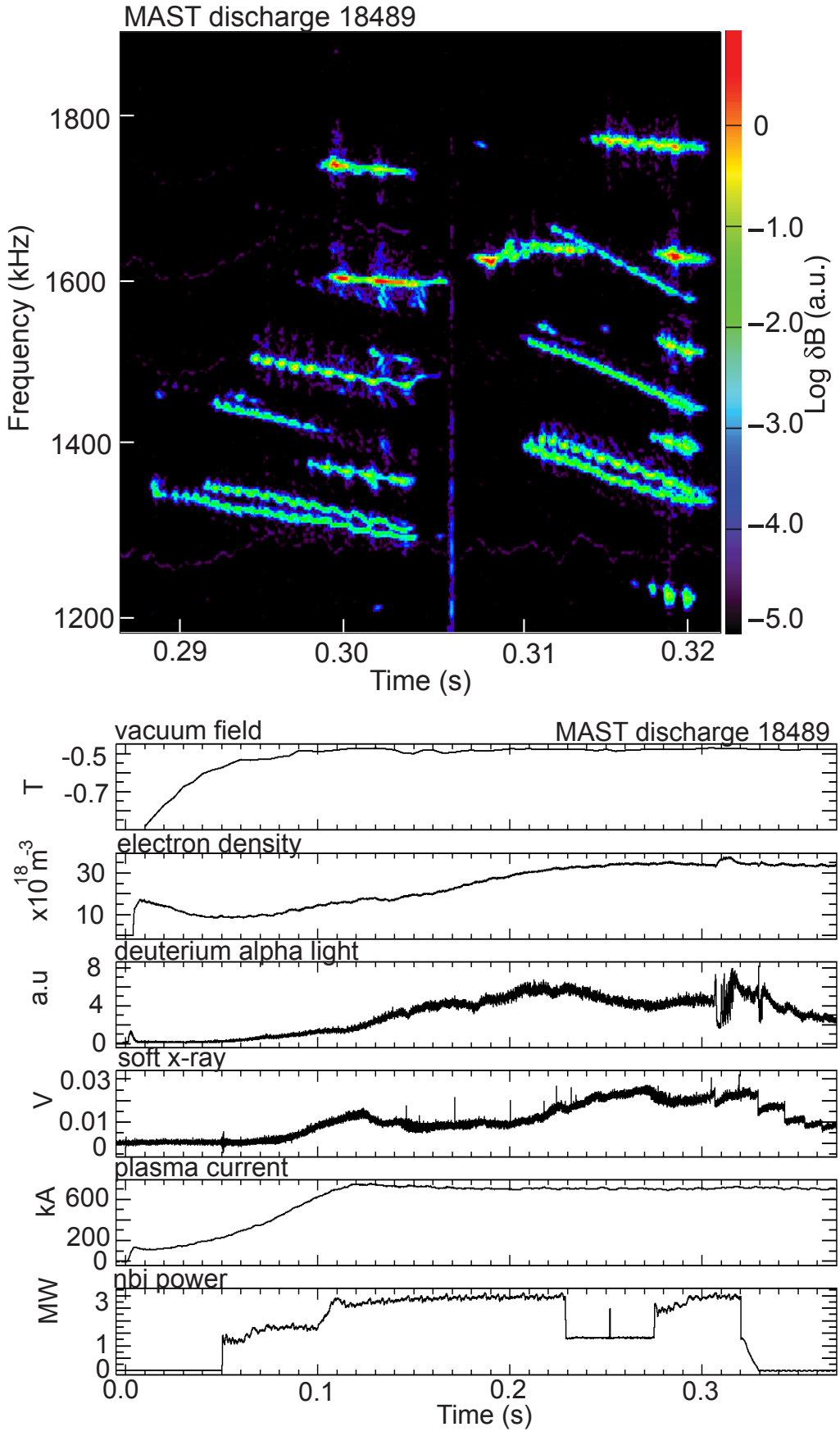

Figure 4.11: *Spectrogram and time trace for pulse 18489.*

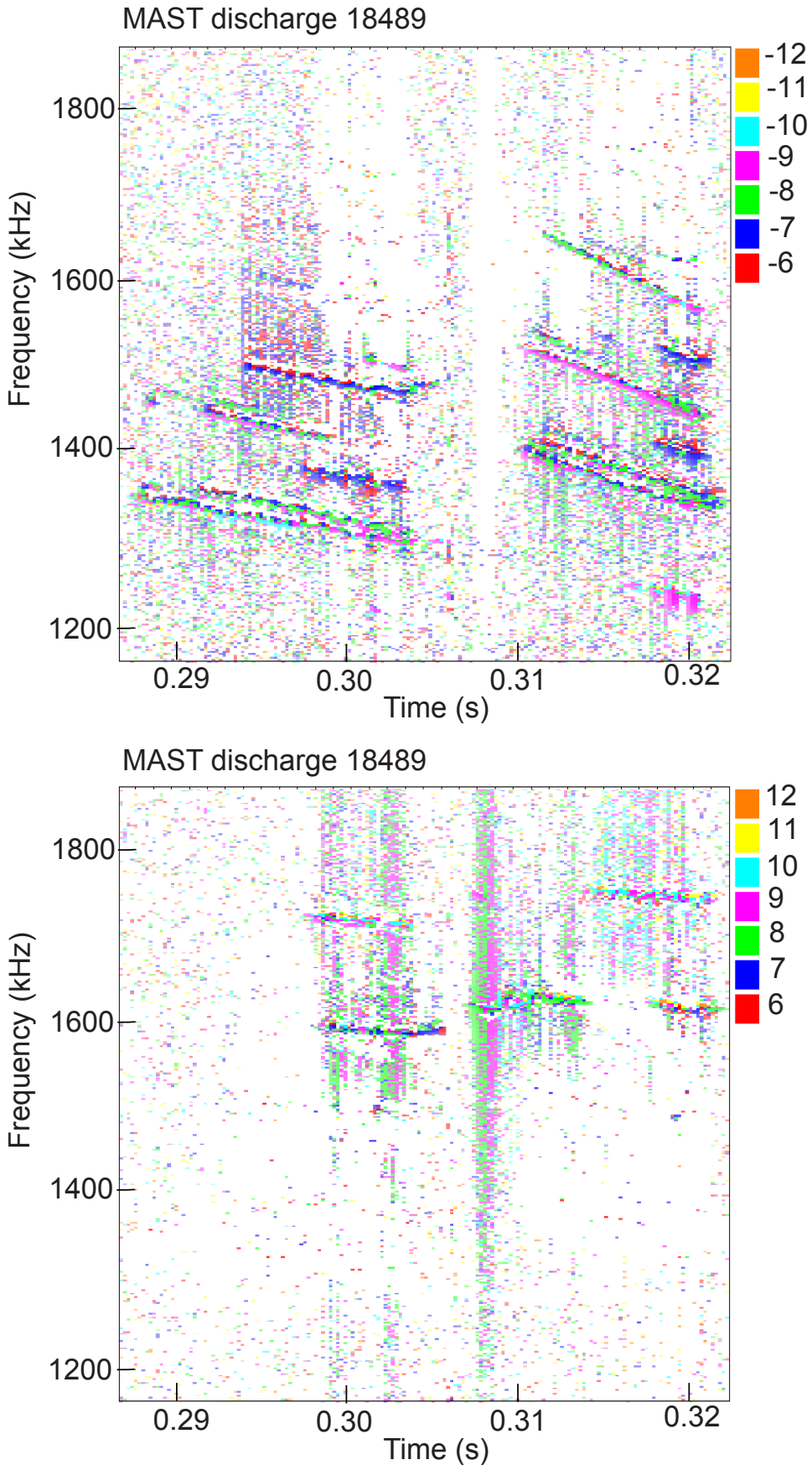

Figure 4.12: *Toroidal mode number analysis for #18489.*

4.2.5 Pellet injection

It has been proposed [47] that the existence of numerous high frequency modes, in this type of MAST discharge, relies on having of a hollow density profile, which was often seen as Figure 4.13 shows.

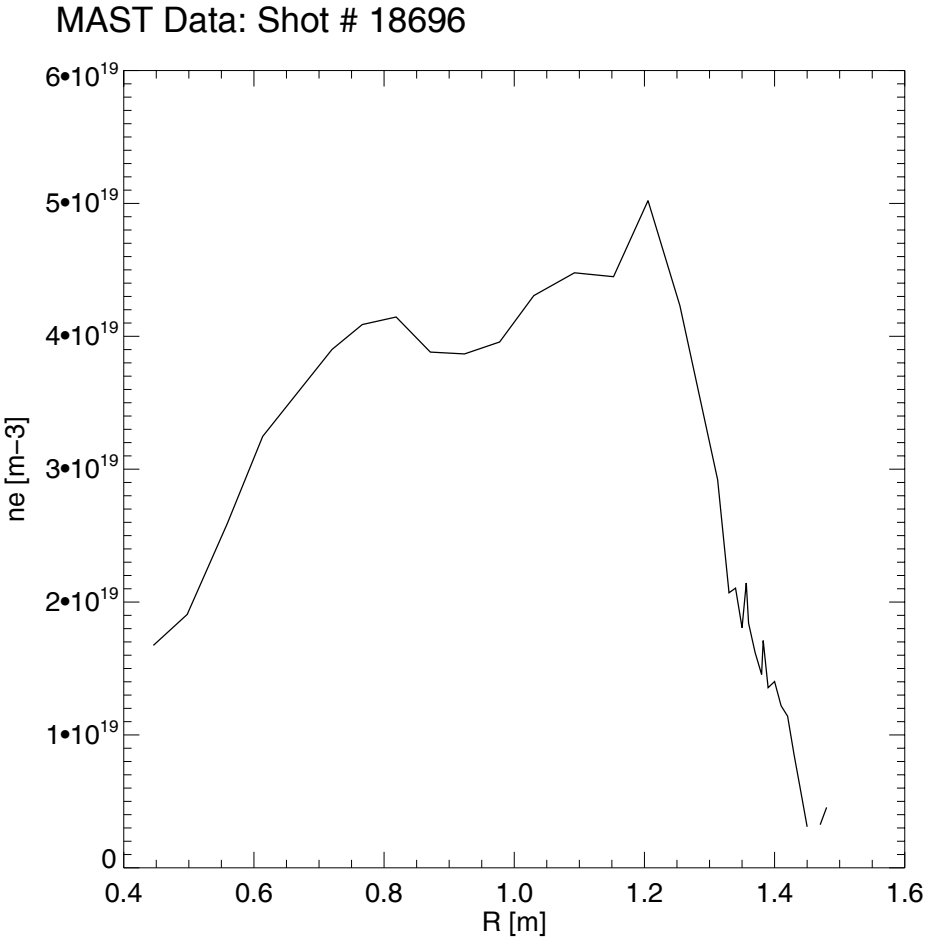

Figure 4.13: *Profile of electron density as measured by the MAST Thompson scattering system at $t = 0.32s$ in pulse #18696*

In order to affect the density profiles, deuterium pellets were injected on pulses #18700 and #18701. For #18700 the pellet was injected into the outer region of the plasma at $t = 0.305$s, which had little effect on the modes as can be seen in Figure 4.15 (top). For #18701, a pellet was injected firstly at $t = 0.3$s into the core of the plasma, where the effect was to extinguish all high frequency activity. The modes subsequently returned at which point a second pellet was injected at

$t = 0.315$s in the outer regions of the plasma, where again the effect was minimal (Fig 4.15 bottom). From this it can be deduced that the hollow density profile is unlikely to play a significant role in the existence of the modes as can also be seen by observing the density evolution in Fig 4.14

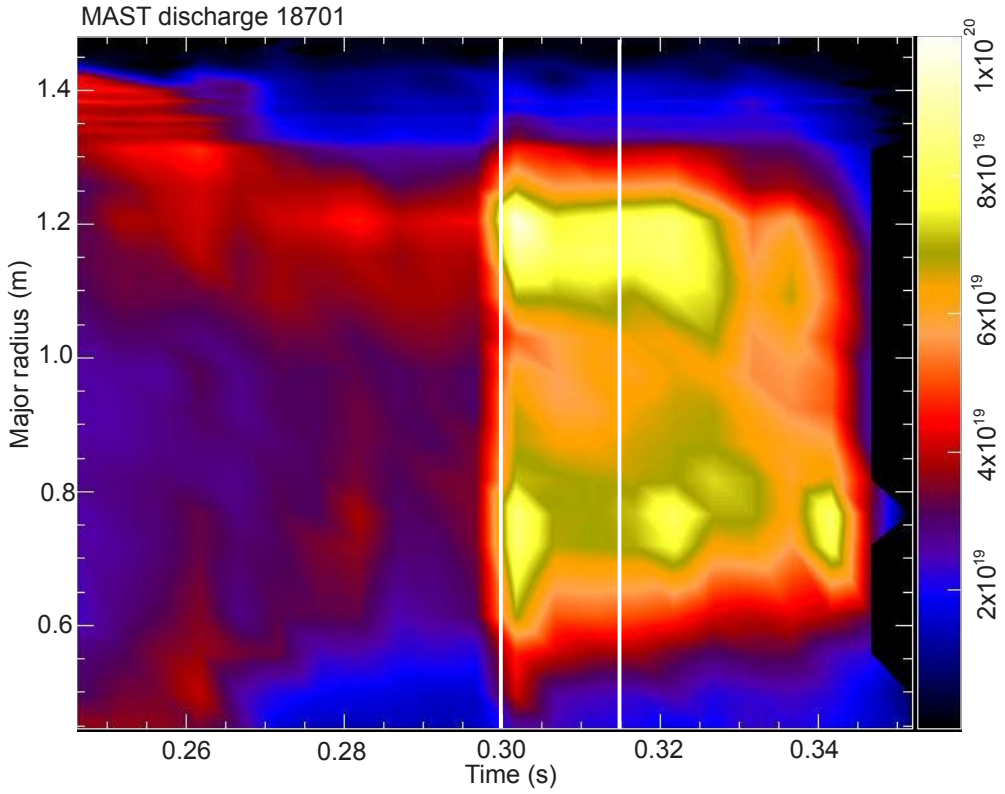

Figure 4.14: *Electron density contours as a function of time for #18701. The white vertical lines indicate the pellet injection times.*

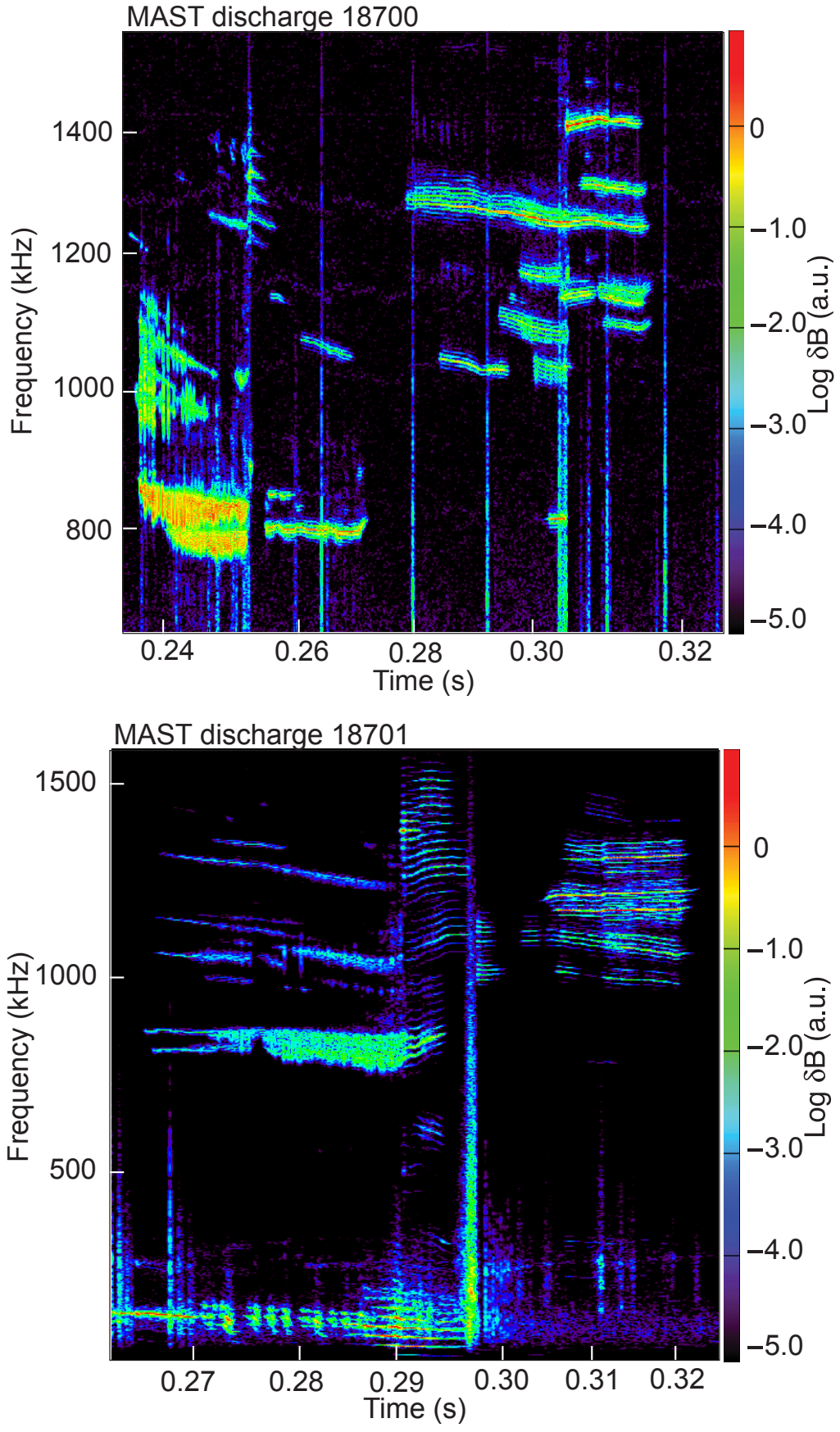

Figure 4.15: *Spectrogram of the high frequency magnetic activity from pulses #18700 and #18701, these discharges were repeats of #18697.*

4.2.6 Very high frequency modes

The experimental results presented so far have shown modes that exist between $\omega_{cD}(0)/4$ and $\omega_{cD}(0)/2$ (where $\omega_{cD}(0)$ is the cyclotron frequency of the thermal deuterium plasma at the geometric axis of the machine). There have been discharges however where modes have been observed with frequencies comparable to the on axis cyclotron frequency of $f_{cD} \approx 3.8$MHz as can be seen in Figure 4.17. It has been shown in chapter 2 and also in other works [15] that high frequency modes tend to be localised at the outboard side of a tokamak plasma. In this case the frequency of the mode seen in Fig 4.17 will certainly be above the local ion cyclotron frequency and hence be compressional in nature.

4.2.7 Linear growth rate

The modes observed in this series of MAST discharges are not driven strongly. By analysing the raw magnetic time series data for MAST #18696 the net linear growth rate ($\gamma \equiv \gamma_l - \gamma_d$) can be determined by fitting an exponential to the data as shown in Fig 4.16, which leads to normalised growth rate $\gamma/\omega \approx 0.5\%$.

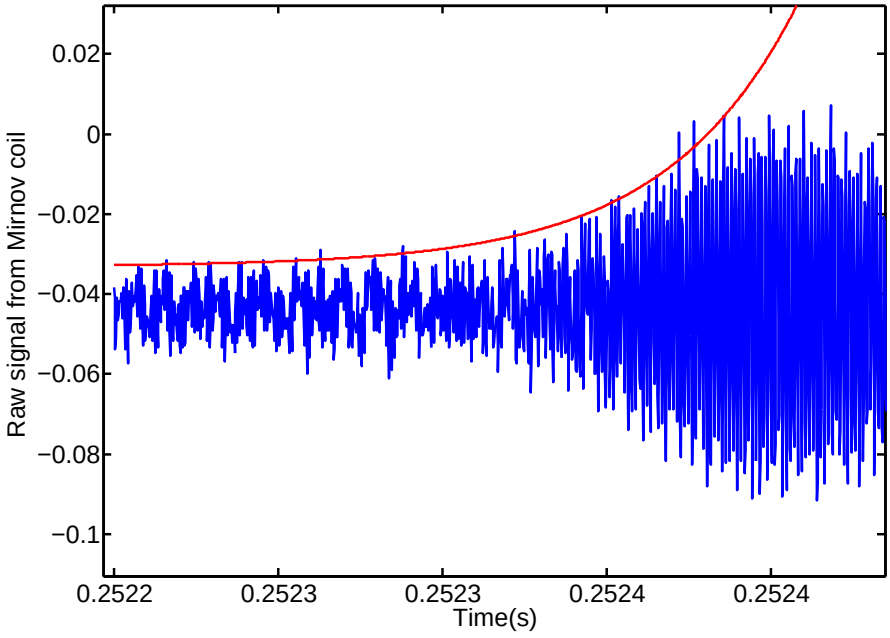

Figure 4.16: *Raw signal from Mirnov coils (blue) together with a fitted exponential (red) for #18696.*

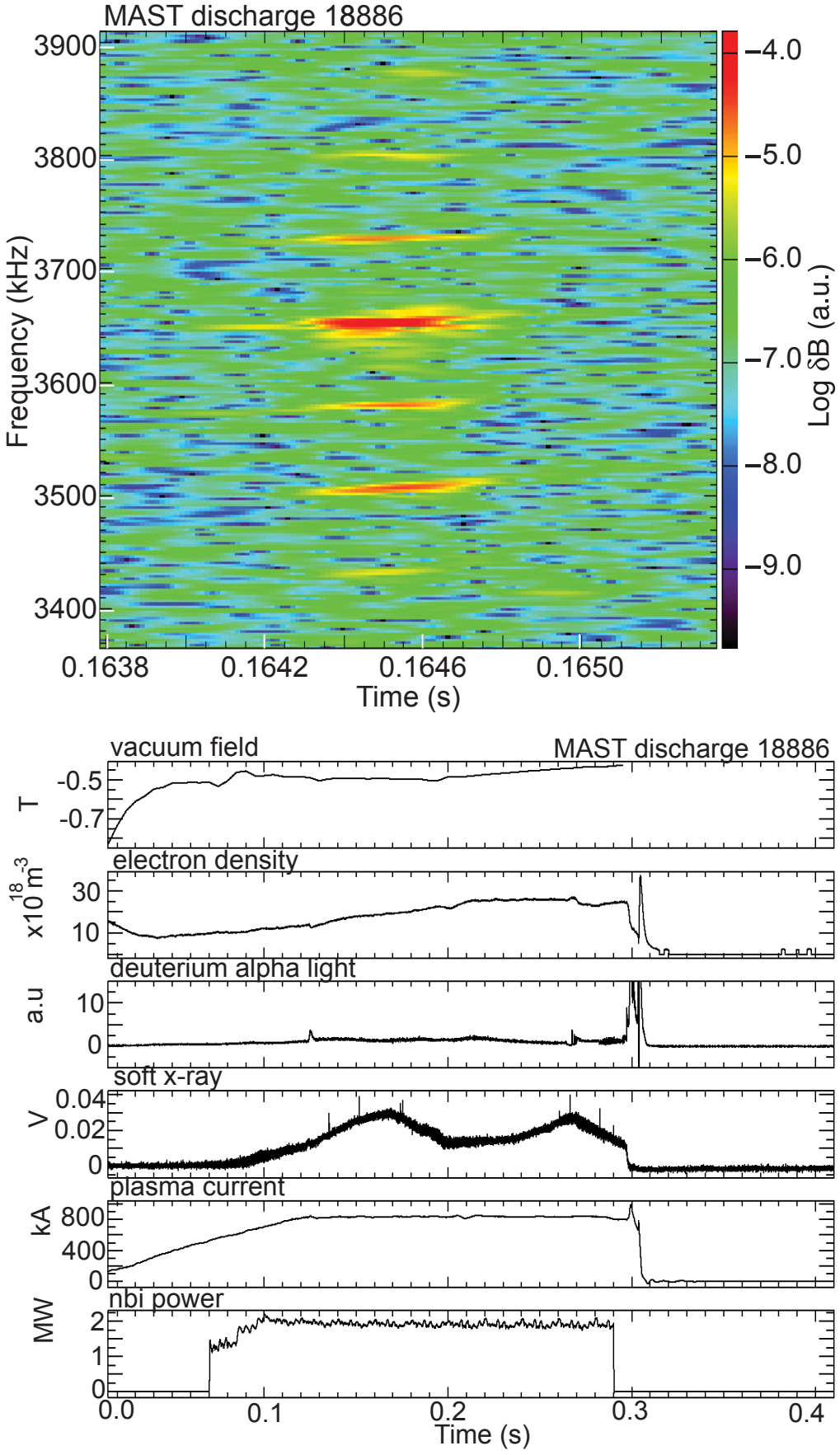

Figure 4.17: *Spectrogram and time trace for pulse 18886.*

4.3 Modelling of high frequency modes on MAST

To model the high frequency modes observed on MAST, the 1-D cold plasma model from chapter 2 is utilised. In contrast to the STPP, where CAEs with $\omega > \omega_{cD}$ were found due to the magnetic well, modes with $\omega < \omega_{cD}$ are searched for on MAST due to the magnetic and density inhomogeneities. Previously the high β plasma of the STPP justified the use of the 1-D approach. In MAST however it is the natural elipticity of the plasma that justifies the 1-D model. By assuming the wave perturbations take the form $e^{i(n\phi+k_\theta r\theta-\omega t)}$, where ϕ is positive in the clockwise direction (from above) and θ is positive in the anti-clockwise direction (in the poloidal plane), then the following is approximately true in a large aspect ratio tokamak plasma.

$$k_\parallel \approx \frac{-n_{\rm exp}q - k_\theta r}{Rq}. \tag{4.1}$$

where $n_{\rm exp} = -n$ is the toroidal mode number using the MAST convention. For the case of a highly elliptical plasma $k_\theta \approx k_z$ and so Eq 4.1 gives an approximate relation between $k_\parallel$ and k_z in the region of mode localisation, which reduces the number of degrees of freedom in the model. From now on, unless otherwise stated, all modelling efforts will refer to discharge #18696 for which the most compete diagnostic data exists.

4.3.1 The equilibrium data

At $t = 0.32$s the plasma had dimensions $R_0 = 0.856$m, $a = 0.605$m and $\varepsilon \equiv a/R_0 = 0.707$. As was described in section 4.2.5 the equilibrium electron density tended to form a hollow structure. The following density model will therefore be used

$$n_e = n_{e0}(1 + Ax^2 - (1 + A)x^4). \tag{4.2}$$

where $x = (R - R_0)/a$. By altering the coefficient A a wide variety of density profiles can be generated as shown in Figure 4.18, where $n_{e0} = 3.9 \times 10^{19}\mathrm{m}^{-3}$. For #18696 $A = 1.75$ is taken. For the STPP, the analysis focussed on a constant density profile, which relied on a combination of the toroidal field from the coils and poloidal field from the plasma current to produce the potential well to localise the

wave. For MAST however the change in density is expected to make a significant contribution to the dielectric tensor, and this will be tested by changing the density profile from one with $A = 1.75$ to one with $A = 0$.

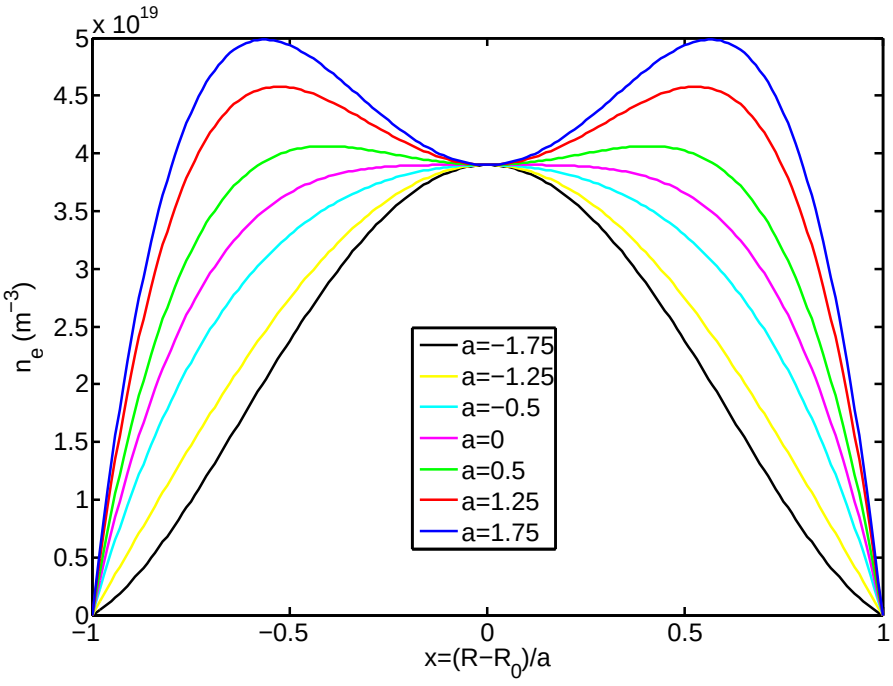

Figure 4.18: *Modelled profiles of electron density for #18696.*

In MAST the plasma current of 700kA produces a poloidal magnetic field that is comparable to the equilibrium toroidal magnetic field from the external coils at the outboard side of the plasma. This can be seen if we assume that the current density J is constant, so that the magnetic field takes the form of Eq 4.3 which is displayed in fig 4.19 (top).

$$B_\phi = \frac{B_0}{1 + \varepsilon x}, \qquad B_\theta = \frac{\mu_0 a J x}{2} \tag{4.3}$$

where B_0 is the vacuum toroidal magnetic field at the geometric axis of the machine and $J = 609\text{kAm}^{-2}$. The equilibrium safety factor q profile is also required for Eq 4.1, which takes the following form as a function of major radius Fig 4.19 (bottom).

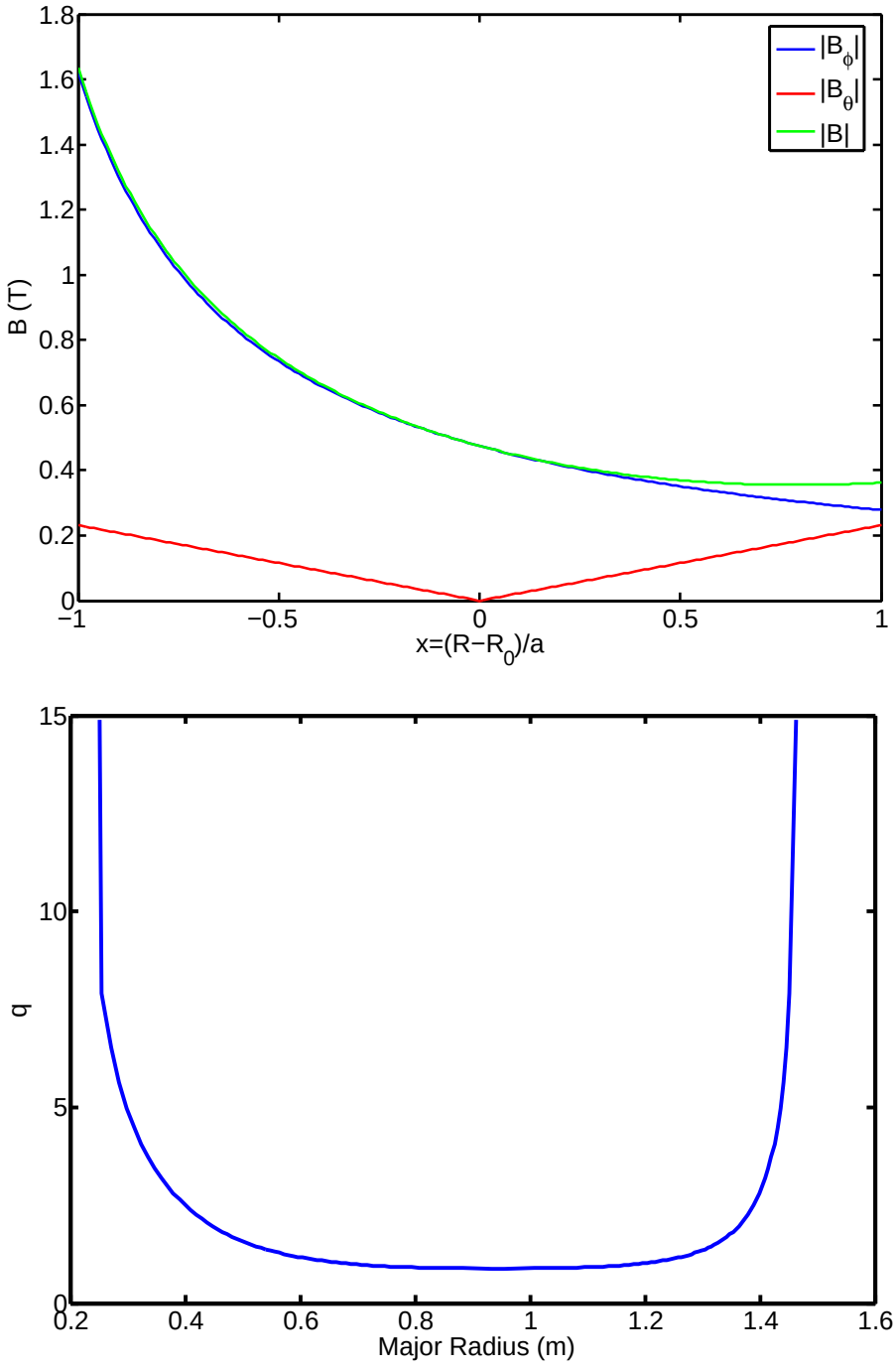

Figure 4.19: *Modelled magnetic field (top) and q profile (bottom) for #18696.*

4.3.2 Spectrum analysis

As with the STPP, the radius of the minimum of the potential well is roughly constant with $R_{\rm loc} \approx 1.23$m in the MAST case. At this major radius in the mid-plane $q \approx 1.08$, which can be seen from Fig 4.19 (bottom). Using these approximations Eq 4.1 can now be utilised to produce the following spectrum of modes as a function of $k_{\|}$ for a $n_{\rm exp} = -9$ mode (Fig 4.20 top). Also overlayed in fig 4.20 is the compressional Alfvén dispersion relation $f = kv_A/2\pi$. The similarity between the two curves indicates that the modes are compressional.

Further evidence of the compressional nature of these modes can be seen by observing the wave polarisation $P = iE_R/E_z$ at the mode localisation position $R_{\rm loc}$. For the spectrum shown in Fig 4.20 (top), the polarisation is shown in Fig 4.20 (bottom). It can be seen that the polarisation is right handed ($P > 0$) indicating the modes are compressional in nature. It should also be noted that the modes are elliptically polarised, meaning both left and right handed components of the wave electric field are present. This implies that multiple energy transfer mechanisms between the fast particles and the wave exist, 1: via the Doppler resonance with the left handed part (no FLR effect) and 2: via Doppler resonance with the right handed part (FLR effect).

The harmonic method has been employed instead of the asymmetric approach in chapter 2. The two methods in fact only show a slight difference in the calculated eigenfrequencies and in the overall shape of the eigenfunction. Since the application of the 1-D model to MAST is only an approximation, inclusion of subtle features such as the asymmetric potential will not add a greater accuracy. Therefore for ease of computation the harmonic method will be used for the MAST analysis. In order to fix the $k_{\|}, k_z$ dependence the localisation radius $R_{\rm loc}$ is required. However, since the eigenmodes are global, the variation of the spectrum as a function of $R_{\rm loc}$ should also be checked. By varying the localisation radius by 10% of the minor radius, a, the spectrum can be seen to change as in figure 4.21 where a maximum variation of about 10% is observed.

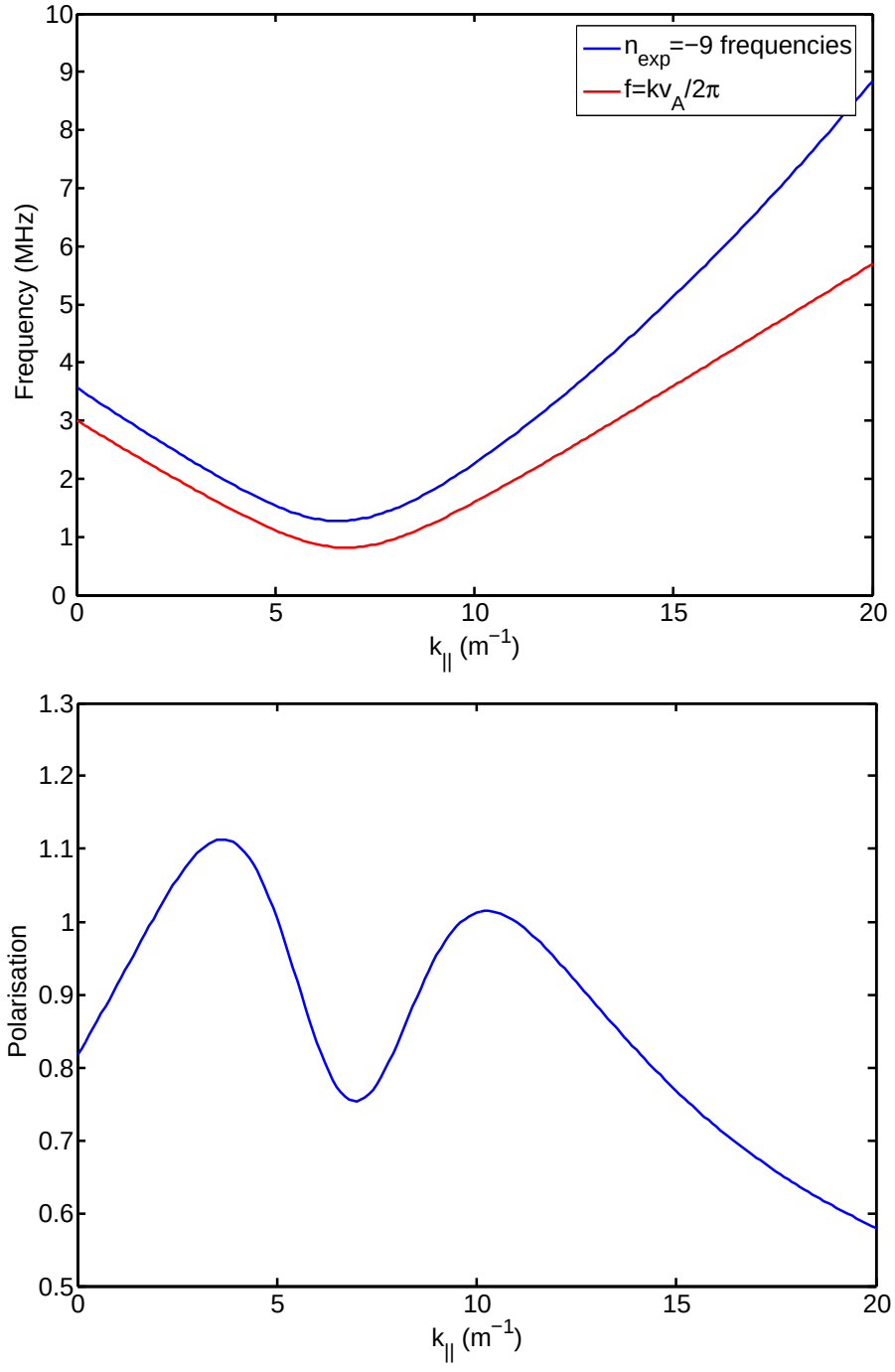

Figure 4.20: *Modelled eigenmode frequency as a function of $k_{\|}$ for a $n_{exp} = -9$ mode for pulse #18696 along with the cartesian dispersion relation for compressional Alfvén waves (top). Polarisation $P = iE_R/E_z$ (bottom).*

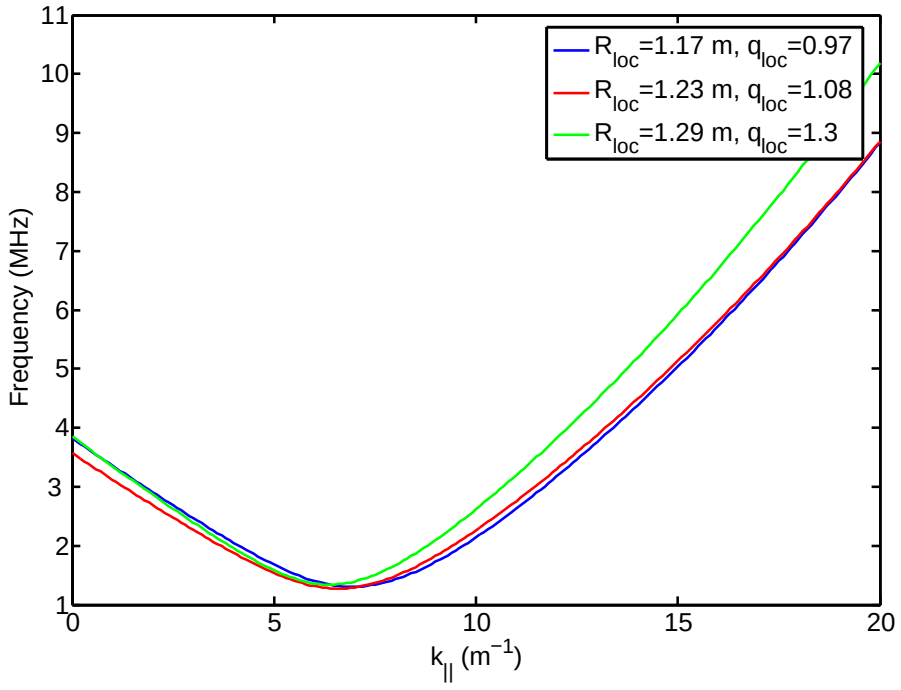

Figure 4.21: *Modelled eigenmode frequency as a function of $k_{\|}$ for a $n_{exp} = -9$ mode for pulse #18696. The different lines show the spectrum for different values of R_{loc}.*

It was previously stated that the role of the density profile would significantly contribute to the dielectric tensor and hence change the mode properties. This is now checked by changing the density profile to $A = 0$ with $n_{e0} = 5 \times 10^{19}\mathrm{m}^{-3}$, which alters the localisation radius from $R_{\mathrm{loc}} = 1.23\mathrm{m}$ to $R_{\mathrm{loc}} = 1.16\mathrm{m}$. This effect can be compared to the case when we change the magnetic field from the total to simply the toroidal component. In this case the localisation radius only changes from $R_{\mathrm{loc}} = 1.23\mathrm{m}$ to $R_{\mathrm{loc}} = 1.26\mathrm{m}$. The effect on the eigenfrequenceis in these cases are shown in Fig 4.22, where the effect of the changing density profile is on the same order as changing the magnetic field profile, about 10% change in frequency.

We note again that since the application of this 1-D model is only an approximation it would not be sensible to compare the absolute eigenfrequenceis with those from the experiments. However features of the spectrum and frequency differences can be meaningfully compared.

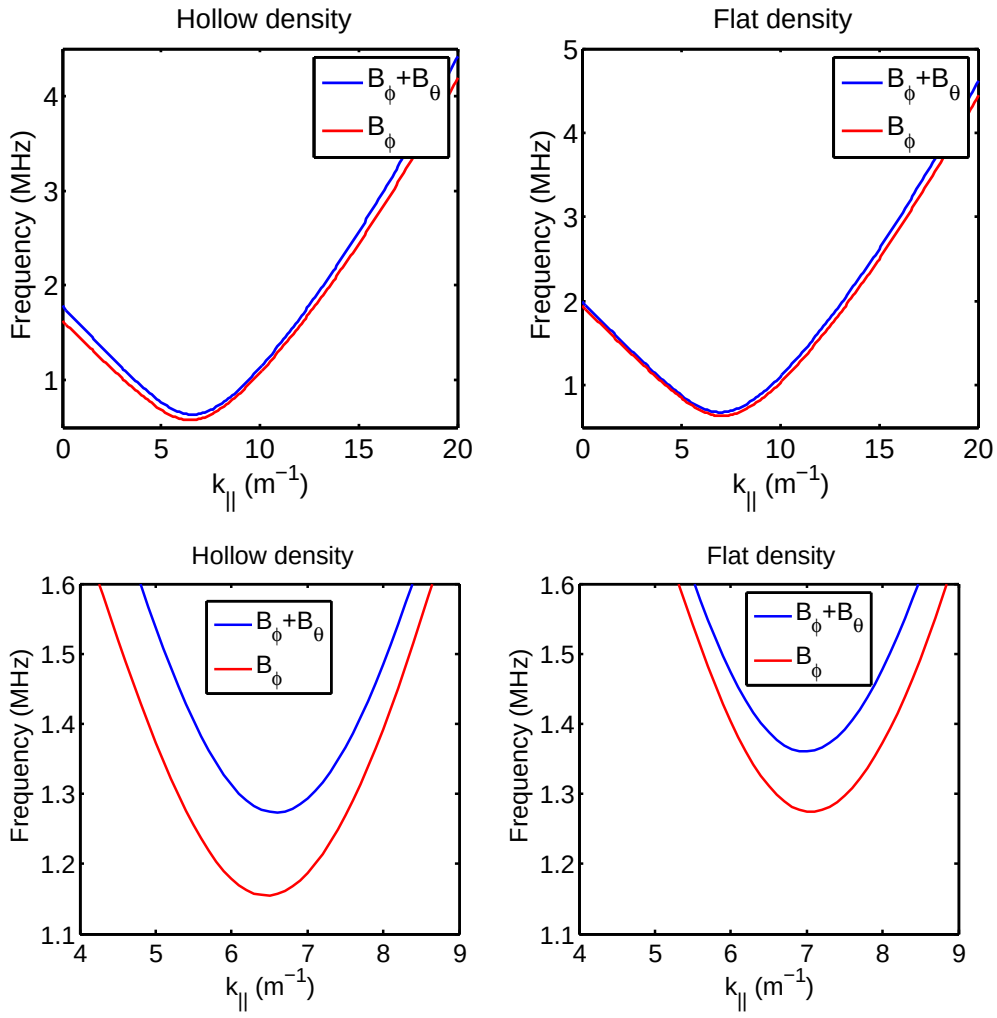

Figure 4.22: *Modelled eigenmode frequency as a function of $k_{\|}$ for a $n_{exp} = -9$ mode for pulse #18696. The different lines show the spectrum for the case of a purely toroidal field (red) and the total field (blue). Left shows the case of a hollow density profile and right shows the flat profile case, bottom displays a zoom of the top.*

4.3.3 Absence of $n_{\mathbf{exp}} > 0$ modes

The most striking feature of the high frequency activity on MAST is the almost total absence of $n_{\mathrm{exp}} > 0$ modes. These are modes which propagate in the same direction as the fast particles and plasma current (opposite to the equilibrium magnetic field). From chapter 3 it can be understood that, for co-propagation, the anomalous Doppler shifted cyclotron resonance is appropriate for $\omega < \omega_{cD}$. From chapter 3 it was noted that in order to access this particular resonance a critical velocity threshold must be overcome. For an infinite homogeneous plasma with energetic ion species the same as that of the bulk plasma this threashold is recalled to be $v_{\parallel}^{\mathrm{crit}}/v_{\mathrm{A}} = 3\sqrt{3}/2$ for purely parallel propagating waves. For compressional modes propagating at an arbitrary angle to the equilibrium magnetic field however this threashold is in fact higher. By taking Eq 4.1 as the form for $k_{\perp}$ the critical velocity can be approximated by (see appendix A)

$$v_{\parallel}^{\mathrm{crit}} = v_{\mathrm{A}}\sqrt{1 + \frac{R^2 q^2}{r^2}}. \tag{4.4}$$

For the MAST deuterium NBI system the maximum injection energy is 65keV, which corresponds to a maximum ion velocity of $v^{\mathrm{max}} = 2.5 \times 10^6 \mathrm{ms}^{-1}$. The threshold is then represented by the following contour plot Fig 4.23, which shows that the threshold cannot be overcome for the energetic particles in #18696. This shows that the anomalous Doppler resonance cannot be accessed and that $n_{\mathrm{exp}} > 0$ modes should not be expected.

4.3.4 Inverted $n_{\mathbf{exp}}$ dependence

From Eq 2.19 in chapter 2 one can see that by increasing $k_{\parallel}$ or k_z the potential well becomes more shallow and so the fundamental frequency becomes higher. In previous theory [15] the frequency dependence on the toroidal mode number n is always a square or modulus, and hence when $|n|$ increases so too does the frequency. Experimental observations however show the reversed trend as seen in Fig 4.8. By plotting the spectrum for multiple n modes a possible explanation for this trend can be seen (Fig 4.24).

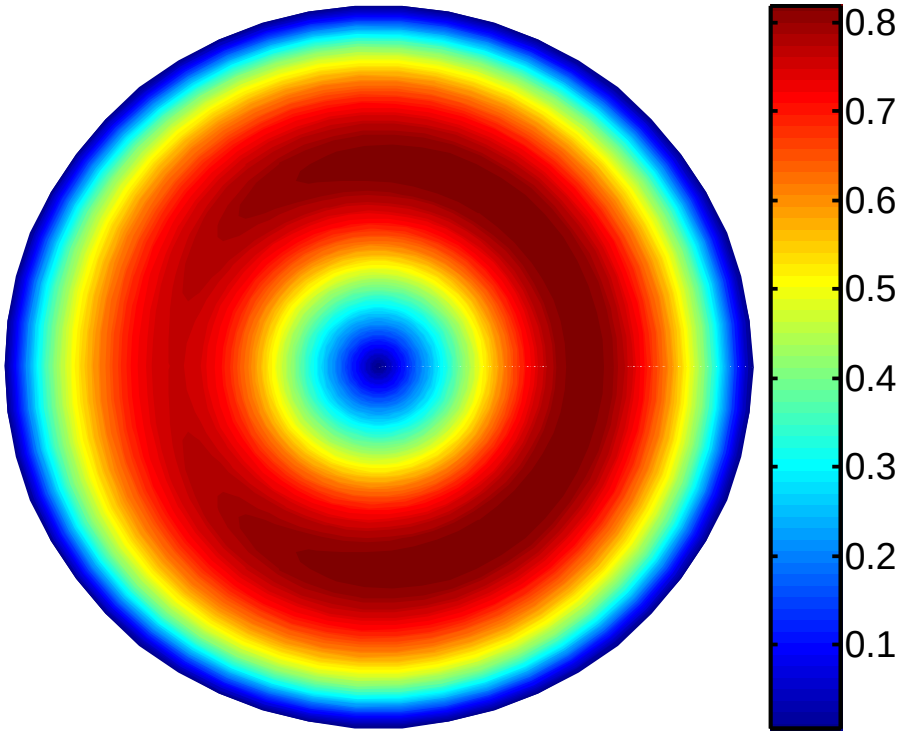

Figure 4.23: *Contours of $v^{max}/v_{\|}^{crit}$ over the plasma cross section. All contours are less than unity, showing that the anomalous Doppler resonance cannot be accessed. The plasma has been assumed to be circular for simplicity.*

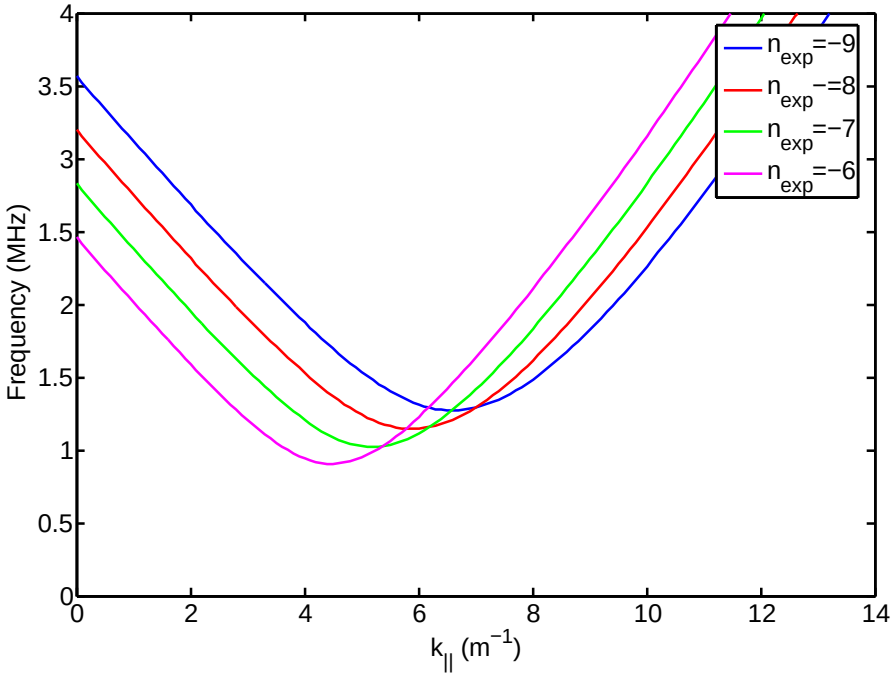

Figure 4.24: *Modelled eigenmode frequency as a function of $k_{\|}$ for $n_{exp} = -9, -8, -7, -6$ modes in pulse #18696.*

For low values of $k_{\|}$ the frequency dependence is as expected from the previous theory. However for larger $k_{\|}$ the trend is indeed reversed. This reversal is due to the differing k_z resulting from the change in n in Eq 4.1. In the language of tokamak geometry, the decrease in frequency is due to a large shift in the poloidal mode number m.

4.3.5 General spectrographic features

Assuming that the observed waves are exited by group of particles with a small range of parallel velocities, then one can place an estimate on the upper bound for the parallel velocity of the resonant particles responsible for exciting these instabilities. By plotting the resonance line $f = v_{\|}/\lambda_{\|} + f_{cD}$, using $R_{\text{loc}} = 1.23\text{m}$, and insisting that the line must intersect the spectrum in Fig 4.24 in the observed frequency order (fig 4.25), the maximum parallel velocity for counter moving ions is approximated as $v_{\|} \approx -1.3 \times 10^6 \text{ms}^{-1}$.

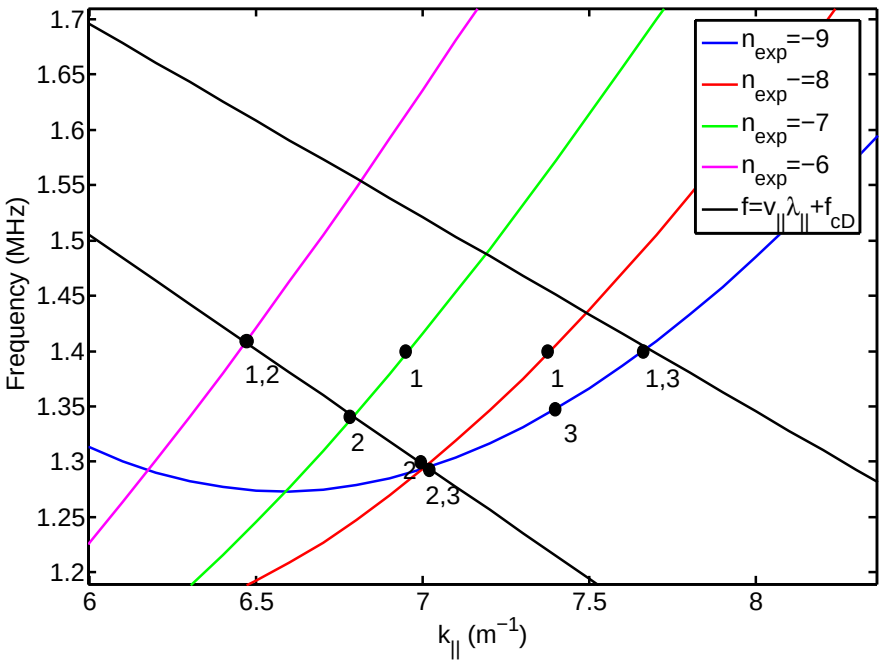

Figure 4.25: *Modelled eigenmode frequency as a function of* $k_{\|}$ *for* $n_{exp} = -9, -8, -7, -6$ *modes for pulse #18696 along with resonance lines for a small range of parallel resonant velocities* ($v_{\|} \in [-1.3 \times 10^6, -1.1 \times 10^6]\, ms^{-1}$).

Using this assumption, a number of questions regarding the level and variety of high frequency activity can be answered. Points 1 in Fig 4.25 show, that within this range of resonant particles, modes with the same frequency but with different toroidal mode numbers can be excited. Spectrographically, this will manifest as modes separated by the toroidal plasma rotation frequency as seen experimentally in Fig 4.8. Points 2 show that modes with different n numbers can be excited with frequency differences up to about 100kHz, with the frequency spacing increasing for decreasing $|n|$. Finally points 3 demonstrate that modes with the same n can be excited with frequency spacing on the order of 100kHz as seen experimentally.

4.4 Discussion

It has been highlighted that the observed modes are most likely to be compressional in nature. The Doppler shifted cyclotron resonance has been shown to be the appropriate resonance for these modes, and the inaccessibility of the anomalous resonance has been suggested as an explanation for the lack of observed $n_{\text{exp}} > 0$ modes. The elliptical polarisation of the modes reveals two routes of energy exchange between the waves and the particles, via the left hand and right hand parts of the wave electric field. This indicates that a more sophisticated linear kinetic treatment will be required to treat these modes fully.

Chapter 5

Linear Kinetic Analysis

The effective excitation of normal modes of a system requires a source of free energy to 'drive' the modes and a resonance to enable the energy to 'flow' into the wave. In the case of modes excited by energetic particles, this free energy arises due to the non thermal component of the distribution function F provided by the fast particles. For the high frequency compressional instabilities observed on MAST, which are excited via the Doppler shifted cyclotron resonance, the relevant free energy source comes from the gradients of the distribution function in velocity space [48, 49]. A kinetic treatment of the linear drive of these instabilities is therefore required.

As was noted in chapter 3, in order for a compressional wave to exchange energy with particles via the Doppler resonance, finite Larmor radius effects must be included. However, it has been observed in confined geometries, for example in the LAPD device (Fig 3.8), that shear waves exhibit both left hand and right hand polarisations, and MAST compressional Alfvén eigenmodes show an elliptical polarisation. The implication for modelling the modes observed on MAST is that there are two components to the linear kinetic drive associated with the left and right handed components of the wave electric field. The left handed part is treated in this chapter, however the right handed part requires finite Larmor radius corrections such as in reference [50] which is not discussed in this thesis.

5.1 TRANSP Simulations

The Monte Carlo part of the TRANSP code [51] is used with 10^5 macro particles to simulate the deuterium NBI distribution function at $t = 0.32$s for #18696.

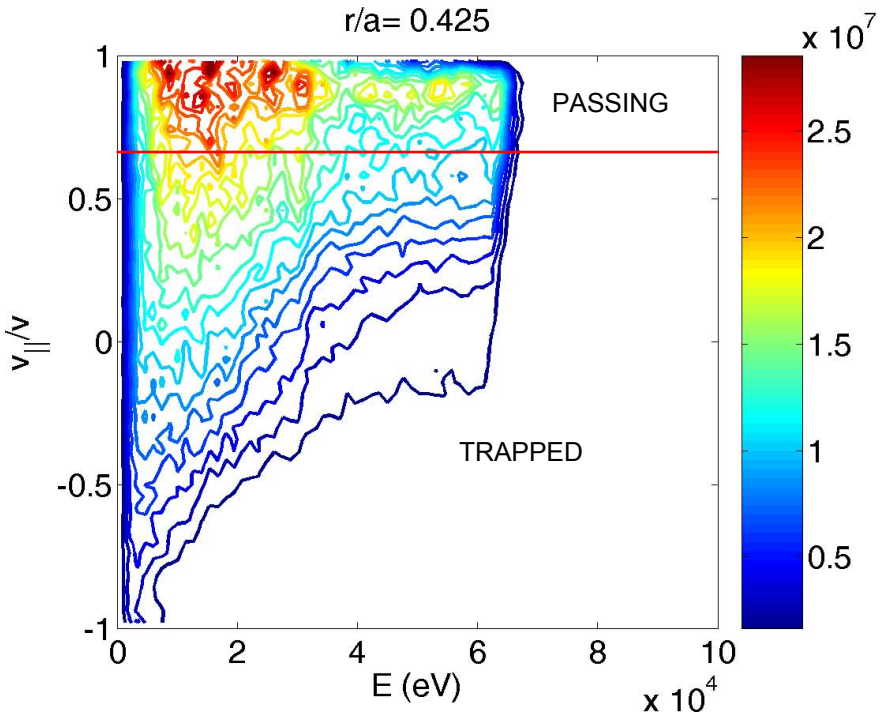

Figure 5.1: *Contours of F_{NBI} as a function of energy and pitch angle averaged over the poloidal angle. Note that positive $v_{\|}/v$ means with respect to the current, not the magnetic field.*

Simulation results show that most of the particles are found to exist in the core of the plasma and also show the existence of a significant (high density of fast ions) bump on tail in energy out to a normalised radius of $r/a = 0.425$. From Figs 5.1 and 5.2, one can see that the bump on tail only exists for passing particles moving almost parallel to the equilibrium field, indicating that the inhomogeneities of the magnetic field should not affect the use of the Doppler shifted cyclotron resonance condition described in chapter 3.

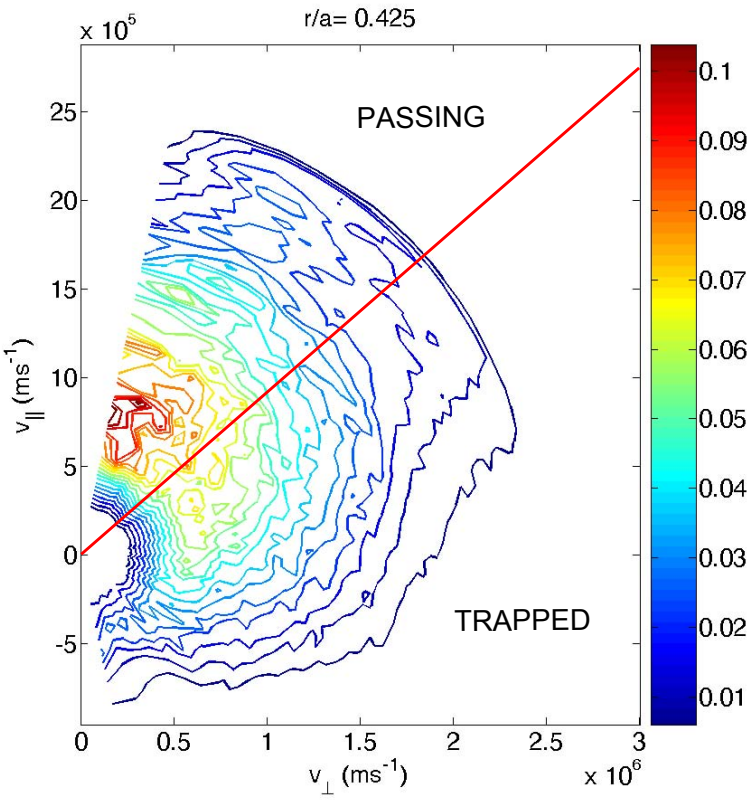

Figure 5.2: *Contours of F_{NBI} as a function of $v_\parallel$ and $v_\perp$ averaged over the poloidal angle. Note the sharp boundary close to $v_\perp = 0$ is a result of TRANSP data not including $v_\parallel/v = 1$. Note also that positive $v_\parallel/v$ means with respect to the current, not the magnetic field.*

5.2 Modelling the distribution function

For those particles with $v_\parallel/v \approx 0.94$ the 'bumps' in the distribution of fast particles are modelled by shifted Gaussian peaks in velocity space. This is in contrast to previous work [52] where a constant pitch angle distribution function was used. The advantage of the Gaussian profile is that the analysis can be performed analytically and gives a physical insight into the drive and damping processes.

By taking a line out of Fig 5.2 at $v_\parallel/v = 0.94$ the total distribution function is then fitted by the sum of 4 Gaussians, 1 from thermal ions and 3 from the NBI ions as shown in Fig 5.3. Physically the 3 bumps from the NBI arise due to the 3 injection energies $E, E/2, E/3$ [45]. However it will be subsequently shown (section 5.4) that only particles with velocities corresponding to the modelled Gaussian 1 will significantly contribute to the kinetic drive, hence the other bumps will be neglected.

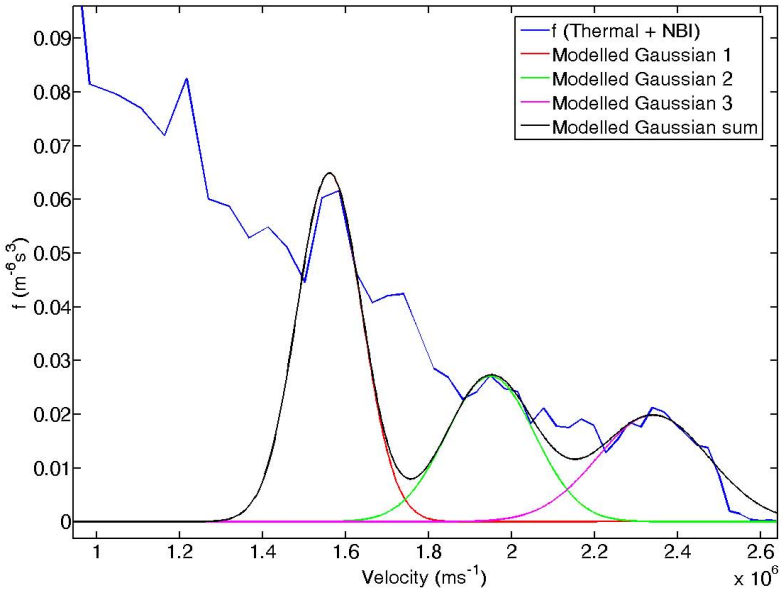

Figure 5.3: *Distribution function (thermal and NBI) as a function of the absolute value of velocity for* $v_{\parallel}/v = 0.94$.

The modelled beam distribution function then becomes

$$f_{\mathrm{tot}} = \frac{n_0}{(2\pi eT(eV)/m)^{3/2}} e^{-E/T_{\mathrm{eV}}} + \frac{n_{b1}}{2\pi^2 v_{\perp b}\Delta v_{\perp}\Delta v_{\parallel}} e^{-\left(v_{\parallel}-v_{\parallel b}\right)^2/\Delta v_{\parallel}^2} e^{-(v_{\perp}-v_{\perp b})^2/\Delta v_{\perp}^2} \tag{5.1}$$

where $n_0 = 4\times10^{19}\mathrm{m}^{-3}$, $T = 950\mathrm{eV}$, $n_{b1} = 1.8\times10^{17}\mathrm{m}^{-3}$, $v_{\parallel b1} = -1.47\times10^{6}\mathrm{ms}^{-1}$, $\Delta v_{\parallel 1} = 1.03\times10^{5}\mathrm{ms}^{-1}$, $v_{\perp} = 6\times10^{5}\mathrm{ms}^{-1}$, $\Delta v_{\perp} = 1\times10^{5}\mathrm{ms}^{-1}$

and we assume $v_{\perp b}^2 \gg \Delta v_{\perp}^2$ in all the calculations that follow.

5.3 Local analysis

In order to calculate the linear kinetic drive, associated with the modelled distribution function in Eq (5.1) for a global eigenmode of a tokamak plasma, a small orbit approximation is assumed, the local drive γ^{loc} is computed and then a weighted integral of this drive, with the wave field, over the region of eigenmode localisation is performed [53]

$$\gamma^{\mathrm{gl}} = \frac{\int_0^a r dr \gamma^{\mathrm{loc}}(r)\left|E(r)\right|^2}{\int_0^a \left|E(r)\right|^2}. \tag{5.2}$$

More specifically the local drive calculation assumes homogeneity of both equilibrium density and magnetic field, with the equilibrium field taking the form $\mathbf{B_0} = B_0\mathbf{e_z}$ in a Cartesian geometry.

The main high frequency activity in #18696 of around 1MHz (Fig 4.20) where $k_\perp/k_\parallel \approx 0.5$. It can be shown [28] that the first finite Larmor radius terms in γ^{loc} are proportional to $k_\perp^2\rho_i^2$ and since the fast particles of interest are mostly propagating parallel to the equilibrium field the limit $k_\perp\rho_i \to 0$ is taken. This simplifies the calculation of the dielectric tensor and dispersion relation, both of which are required in the calculation of γ^{loc}.

5.3.1 $k_\perp\rho_i = 0$ dielectric tensor

The dielectric tensor ε takes the same form as for the cold plasma limit (Eq 2.3) for $k_\perp\rho_i = 0$ [28]

$$\varepsilon = \begin{pmatrix} \varepsilon_1 & i\varepsilon_2 & 0 \\ -i\varepsilon_2 & \varepsilon_1 & 0 \\ 0 & 0 & \varepsilon_3 \end{pmatrix} \tag{5.3}$$

where

$$\varepsilon_1 = 1 + \varepsilon_- + \varepsilon_+ \tag{5.4a}$$

$$\varepsilon_2 = \varepsilon_- - \varepsilon_+ \tag{5.4b}$$

recalling that the dielectric tensor is obtained through the conductivity tensor σ by $\varepsilon = I + i\sigma/\epsilon_0\omega$ and specifically the quantities $\varepsilon_\mp$ are related to the conductivity tensor element σ_{xx}, which takes the following form for $k_\perp\rho_i = 0$

$$\sigma_{xx} = \sum_s \frac{-q_s^2}{m_s}\frac{i\pi}{2}\int_{-\infty}^{\infty}\int_0^{\infty} v_\perp^2 U\left[\frac{1}{\omega - k_\parallel v_\parallel - \omega_{cs}} + \frac{1}{\omega - k_\parallel v_\parallel + \omega_{cs}}\right] dv_\perp dv_\parallel, \tag{5.5}$$

where,

$$U = \frac{\partial f_{0s}}{\partial v_\perp} + \frac{k_\parallel}{\omega}\left(v_\perp\frac{\partial f_{0s}}{\partial v_\parallel} - v_\parallel\frac{\partial f_{0s}}{\partial v_\perp}\right), \tag{5.6}$$

f_{0s} is the equilibrium distribution function for species s and q_s, m_s, ω_{cs} are the charge, mass and cyclotron frequency of species s [28]. From this the ion beam contribution

from Eq 5.1 is found to be

$$\varepsilon_{b\mp} = \frac{\omega_{pb}^2}{2\omega^2}\left\{\frac{3}{2}\frac{\Delta v_\perp^2}{\Delta v_\parallel^2} + \frac{v_{\perp b}^2}{\Delta v_\parallel^2} - 1 + Z\left(x_\mp\right)\left[\frac{\omega}{k_\parallel \Delta v_\parallel} - \frac{v_{\parallel b}}{\Delta v_\parallel} + x_\mp\left(\frac{3}{2}\frac{\Delta v_\perp^2}{\Delta v_\parallel^2} + \frac{v_{\perp b}^2}{\Delta v_\parallel^2} - 1\right)\right]\right\} \tag{5.7}$$

The thermal deuterium and electron contributions are found to be

$$\varepsilon_{D\mp} = \frac{\omega_{pD}^2}{2\omega k_\parallel v_{\mathrm{T}D}} Z\left(\frac{\omega \mp \omega_{cD}}{k_\parallel v_{\mathrm{T}D}}\right) \tag{5.8a}$$

$$\varepsilon_{e\mp} = \frac{\omega_{pe}^2}{2\omega k_\parallel v_{\mathrm{T}e}} Z\left(\frac{\omega \mp \omega_{ce}}{k_\parallel v_{\mathrm{T}e}}\right) \tag{5.8b}$$

where the thermal distributions are maxwellians, ω_p is the plasma frequency, v_{T} is the thermal speed, Z is the plasma dispersion function and $x_\mp = \left(\omega - k_\parallel v_{\parallel b} \mp \omega_{cD}\right)/k_\parallel \Delta v_\parallel$ (for a deuterium beam). The $\mp$ correspond to the Doppler and anomalous Doppler resonances respectively as discussed in chapter 3.

5.3.2 The dispersion relation

The wave equation Eq (2.1) can be simplified using the local approximation ($\nabla \rightarrow i\mathbf{k}$) and since $k_\perp^2 \rho_i^2$ terms have been neglected in the dielectric tensor they should also be neglected in the wave equation. This leads to two possible solutions in the limit of infinite plasma conductivity parallel to the equilibrium magnetic field [28]

$$N_\parallel^2 = \varepsilon_1 + \varepsilon_2 \tag{5.9a}$$

$$N_\parallel^2 = \varepsilon_1 - \varepsilon_2 \tag{5.9b}$$

where $N_\parallel = ck_\parallel/\omega$ is the refractive index parallel to the equilibrium magnetic field, $k_\parallel = \mathbf{k}\cdot\mathbf{B_0}/|\mathbf{B_0}|$. Eqs 5.9a and 5.9b describe left (shear branch) and right (compressional branch) handed polarised electromagnetic waves respectively [28] and can be rewritten as

$$N_\parallel^2 = 1 + 2\varepsilon_\mp \tag{5.10}$$

where $-$ and $+$ correspond to Eq (5.9a) and Eq (5.9b) respectively. From this it can be seen that the shear branch only receives kinetic contributions via the Doppler resonance and the compressional branch only via the anomalous resonance. This is consistent with neglecting the finite Larmor radius terms in the dispersion relation

and in the dielectric tensor. If the thermal plasma is assumed to be 'cold' and the frequency range of interest satisfies $\omega \ll \omega_{ce}, \omega_{pe}$, then the dispersion relation for electromagnetic waves becomes

$$\Lambda_{\text{th}} + \Lambda_b = 0 \tag{5.11a}$$

$$\Lambda_{\text{th}} = N_{\parallel}^2 - 1 - \frac{\mp\omega_{pD}^2}{\omega_{cD}\left(\omega \mp \omega_{cD}\right)}, \qquad \Lambda_b = -2\varepsilon_{b\mp} \tag{5.11b}$$

5.3.3 The growth rate $\gamma^{\text{loc}}/\omega$

Since the waves under investigation are harmonic in time, the real part of the wave frequency (ω) corresponds to oscillations whilst the imaginary part (γ^{loc}) corresponds to exponential growth or decay of the associated wave. The ratio $\gamma^{\text{loc}}/\omega$ therefore gives the growth rate (or decay rate) normalised to the oscillation frequency. By noting from Eq (5.1) that $n_b/n_0 \ll 1$ and from section 4.2.7 that $\gamma^{\text{loc}}/\omega \ll 1$, the small parameter $\delta \sim n_b/n_0 \sim \gamma^{\text{loc}}/\omega \ll 1$ is used to re-write the dispersion relation as an expansion in δ

$$\mathscr{O}\left(\delta^0\right) \quad : \qquad \Lambda_{\text{th}} = 0 \tag{5.12a}$$

$$\mathscr{O}\left(\delta^1\right) \quad : \qquad \gamma^{\text{loc}} = \frac{-\text{Im}\left(\Lambda_b\right)}{\frac{\partial \Lambda_{\text{th}}}{\partial \omega}}. \tag{5.12b}$$

Eq (5.12a) gives the solution for the real part of the frequency ω, which is then substituted into Eq (5.12b) to calculate the growth rate γ^{loc}. From this it can be understood that the imaginary contribution to Λ_b comes only from the plasma dispersion function [28]

$$Z\left(x\right) = e^{-x^2}\left(i\pi^{1/2} - 2\int_0^x e^{t^2} dt\right). \tag{5.13}$$

The normalised local linear growth rate is then calculated to be

$$\frac{\gamma^{\text{loc}}}{\omega} = \frac{-\sqrt{\pi} e^{-x_{\mp}^2} \dfrac{\omega_{pb}^2}{\omega^2}\left[\dfrac{\omega}{k_{\parallel}\Delta v_{\parallel}} - \dfrac{v_{\parallel b}}{\Delta v_{\parallel}} + x_{\mp}\left(\dfrac{3}{2}\dfrac{\Delta v_{\perp}^2}{\Delta v_{\parallel}^2} + \dfrac{v_{\perp b}^2}{\Delta v_{\parallel}^2} - 1\right)\right] \text{sgn}\left(k_{\parallel}\right)}{2 + \dfrac{\omega_{pD}^2}{\left(\omega \mp \omega_{cD}\right)^2}} \tag{5.14}$$

so that an instability can arise when the square bracket is negative.

5.3.4 The instability threshold

For the experimentally observed case of modes driven via the Doppler shifted cyclotron resonance with a negative beam velocity (negative with respect to the magnetic field) and counter propagating waves with $\omega < \omega_{cD}$, the condition for an instability to develop can be represented by

$$\left|v_{\|b}\right| < -\frac{\omega}{k_{\|}} - \frac{\omega_{cD}}{k_{\|}}\left[\frac{\Delta v_{\|}^2}{\frac{3}{2}\Delta v_{\perp}^2 + v_{\perp b}^2} - 1\right], \tag{5.15}$$

where the following anisotropy condition must therefore be necessary satisfied

$$\frac{\Delta v_{\|}^2}{\frac{3}{2}\Delta v_{\perp}^2 + v_{\perp b}^2} < 1 - \frac{\omega}{\omega_{cD}}. \tag{5.16}$$

This implies that anisotropy of the kind shown in Fig 5.4 is preferable for generating an instability, which warrants the use of a non zero $\Delta v_{\perp}$ Gaussian over a constant pitch angle distribution function.

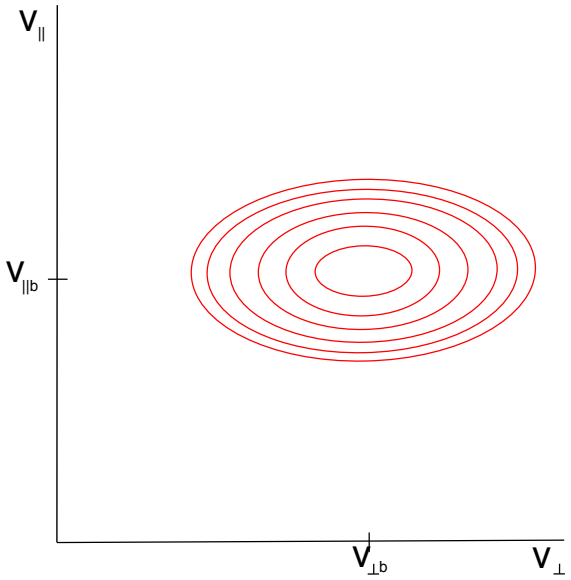

Figure 5.4: *Contours of F_{NBI} from Eq 5.1*

It can be seen that if the unstable temperature anisotropy condition [54]

$$\frac{\Delta v_{\|}^2}{\Delta v_{\perp}^2} < 1 - \frac{\omega}{\omega_{cD}}. \tag{5.17}$$

is satisfied then, as long as $\left|v_{\|b}\right|$ is not too large, an instability will arise. However if temperature anisotropy is not satisfied then a critical $v_{\perp b}$ is required to initiate an instability.

For the case of the anomalous Doppler shifted cyclotron resonance with a negative beam velocity (negative with respect to the magnetic field) and co propagating waves, the instability condition can be represented by

$$\left|v_{\|b}\right| > -\frac{\omega}{\left|k_{\|}\right|} + \frac{\omega_{cD}}{\left|k_{\|}\right|}\left[\frac{\Delta v_{\|}^2}{\frac{3}{2}\Delta v_{\perp}^2 + v_{\perp b}^2} - 1\right]. \tag{5.18}$$

In order of an instability to develop for an arbitrary $v_{\|b}$ it can then be seen that the following condition must be satisfied

$$\frac{\Delta v_{\|}^2}{\frac{3}{2}\Delta v_{\perp}^2 + v_{\perp b}^2} > 1 - \frac{\omega}{\omega_{cD}}. \tag{5.19}$$

and that therefore the unstable temperature anisotropy condition [54]

$$\frac{\Delta v_{\|}^2}{\Delta v_{\perp}^2} > 1 + \frac{\omega}{\omega_{cD}}. \tag{5.20}$$

must also be necessarily satisfied. This implies that anisotropy of the kind shown in Fig 5.5 is preferable for generating an instability. However if Eq 5.19 is not satisfied then temperature anisotropy is no longer a necessary condition for an instability and a critical $v_{\|b}$ is required to initiate an instability.

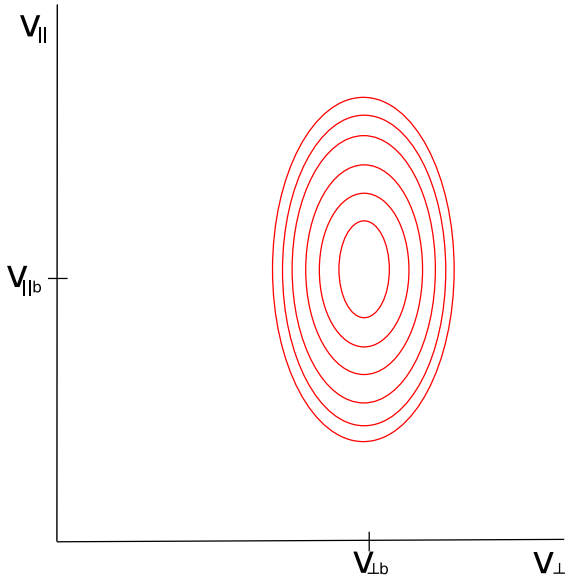

Figure 5.5: *Contours of F_{NBI} from Eq 5.1*

In summary, waves in resonance via the Doppler and anomalous Doppler mechanisms have been shown to be unstable to opposite anisotropy regimes. Although not a necessary condition for the onset of an instability, temperature anisotropy contributes in a destabilising way to the growth of an instability.

5.4 Global analysis

To calculate the global kinetic growth rate from Eq 5.2 the spectrum from Fig 4.20 in chapter 4 is substituted into the expression for the local growth rate in Eq 5.14 which yields Fig 5.6, noting that the velocity space part of the distribution function defined in Eq (5.1) is assumed to hold for all radii.

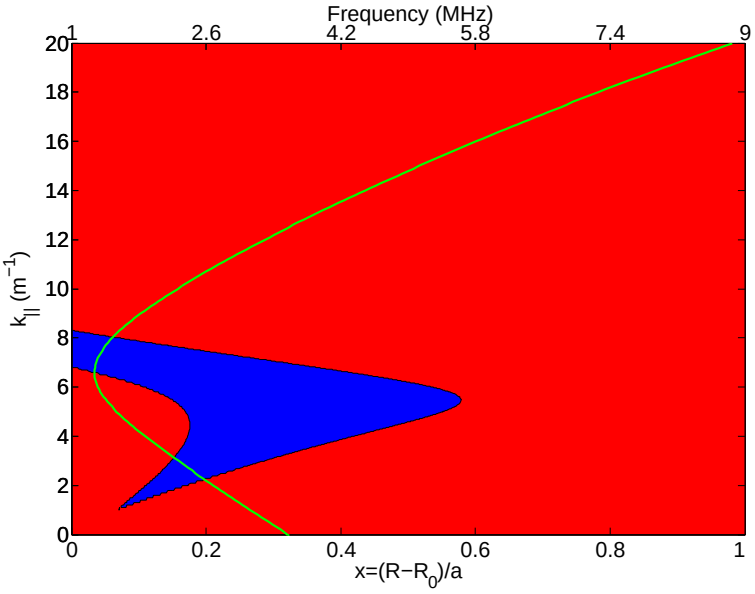

Figure 5.6: γ^{loc} *as a function of normalised radius and* $k_{\|}$ *for the Doppler resonance. Blue indicates regions of instability while red indicates regions of damping. The green line shows the eigenfrequency corresponding to* $k_{\|}$

From Fig 4.6 the main $n_{\text{exp}} = -9$ activity was found at around 1MHz, so the lowest eigenfrequency from Fig 5.6 is taken to produce γ^{loc} as a function of radius as shown in Fig 5.7 (essentially taking a line out of Fig 5.6 at $k_{\|} = 6.6\text{m}^{-1}$). The important difference to note between the symmetric and asymmetric eigenmodes in Fig 5.7 is that the peak shifts more to the outboard side of the plasma in the symmetric case, into the damping region, so that one can expect a more heavily damped mode in this case.

Note that for the lowest eigenfrequency $v_{\|\text{res}}\,(r/a = 0.425) \approx -1.4 \times 10^6\text{ms}^{-1}$ showing (from Fig 5.3) that modelled Gaussian 1 is indeed the most important part of the distribution function to include in the drive calculation.

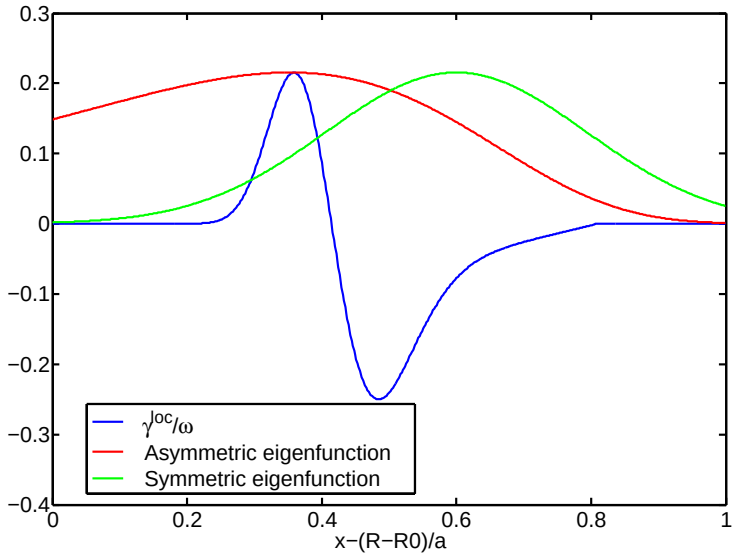

Figure 5.7: *The normalised growth rate as a function of normalised radius (blue) and the eigenmode (or electric field) profile as a function of radius (asymmetric red and symmtric green).*

To calculate the global drive for the mode in Fig 5.7, one must perform the integral from Eq (5.2) of the local drive over the eigenmode region. In the case of Fig 5.7 this results in a damping $\gamma^{\rm gl}/\omega = -0.0086$ for the asymmetric case and $\gamma^{\rm gl}/\omega = -0.0183$ for the symmetric case. However, since TRANSP is accurate to about 10% [51] it is sensible to calcualte the global drive as a function of $v_{\|b}$ and $v_{\perp b}$ to asses the sensitivity of our result (Fig 5.8).

The use of a velocity 'bump' that persists out to all radii is a major source of damping in this calculation. Despite this fact however Fig 5.8 shows that, within the error bars of TRANSP, an overall growth can be calculated for a $n_{\rm exp} = -9$ mode at about $f = 1$MHz.

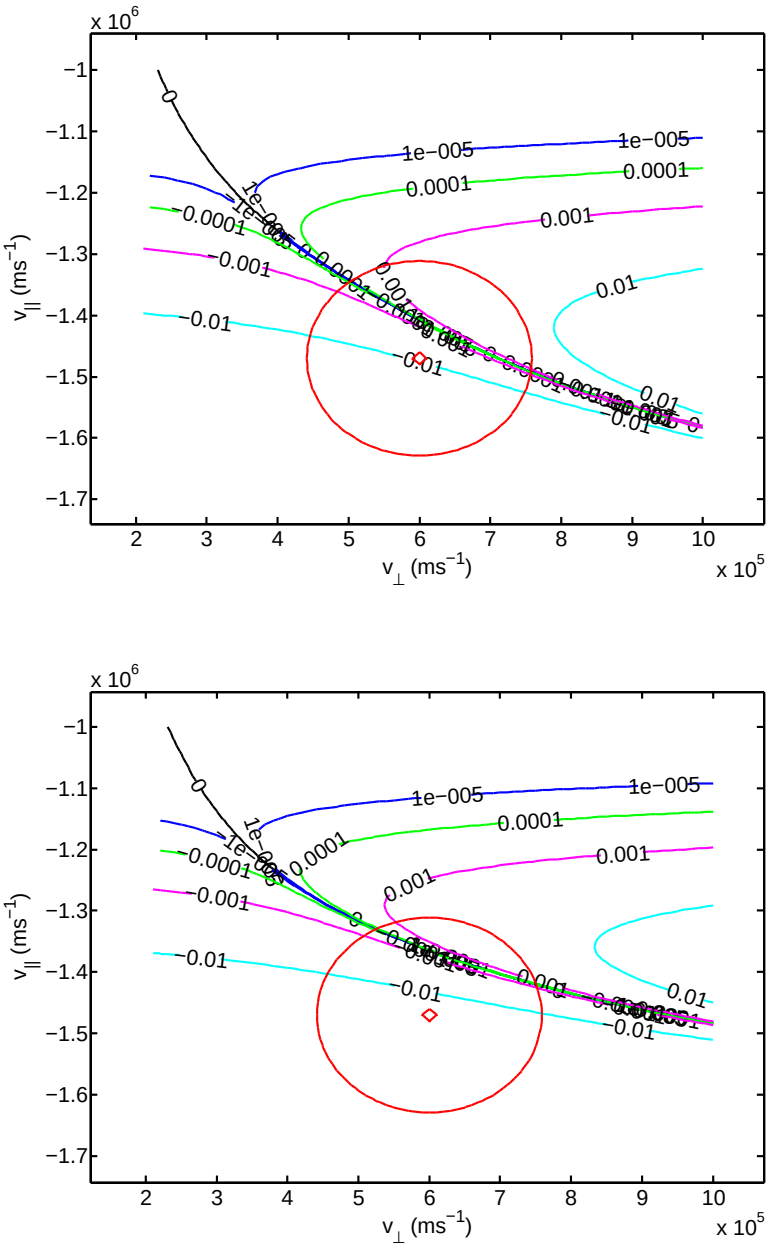

Figure 5.8: *γ^{gl}/ω contours as a function of $v_{\|b}$ and $v_{\perp b}$ using an asymmetric (top) and symmetric (bottom) eigenfunctions. The red circle shows the 10% tolerance around the TRANSP value of the modelled beam velocity.*

5.5 Discussion

The linear kinetic drive for the high frequency compressional modes observed on MAST has been calculated for the contribution arising from the left handed part of the elliptical wave polarisation. Modelling of the distribution function from the TRANSP data using a simplified shifted Gaussian distribution function reveals that the instability threshold depends on temperature anisotropy and on velocity thresholds, with the Doppler and anomalous Doppler resonances exhibiting opposite trends from one another. This simplified distribution also shows that the kinetic drive is extremely sensitive to the details of the distribution function and that the most accurate simulation should always be used for velocity space instabilities.

Chapter 6

Non-linear analysis near marginal stability

The final chapter in this thesis investigates the non-linear evolution of marginally unstable Alfvénic modes excited by NBI fast ions in spherical tokamaks. It will be shown that the effect of dynamical friction is destabilising compared to velocity space diffusion, and the experimental differences between beam driven and ICRH driven Toroidal Alfvén Eigenmodes (TAEs) will be interpreted. Until this point only the existence and excitation of these modes has been discussed, however the non-linear evolution of fast particle driven modes is also of interest, as this determines the possible character of any fast particle losses i.e pulsating or steady state. The character of the evolution can remotely provide information about the plasma conditions [14], which will be necessary for 'burning' plasma environments that cannot be accessed directly. Such waves (e.g TAEs) also have the potential to eject energetic particles from the plasma [55], which is undesirable. Although full multi-mode analysis is required to assess the global transport properties, the non-linear temporal behaviour of individual waves is nevertheless an essential element of any calculations with predictive capability.

6.1 Marginal stability

A mode of the system it said to be 'marginally unstable' if it is driven just above the instability threshold and so satisfies

$$\gamma \equiv |\gamma_l - \gamma_d| \ll \gamma_d \leq \gamma_l \tag{6.1}$$

where γ_l is the linear growth rate of the wave and γ_d is the linear wave damping rate. For a marginally unstable mode the characteristic time for the wave electric field to grow, $1/\gamma$, can become comparable with collisional times, $1/\nu_{\text{eff}}$, which represents the characteristic time for restoring the unstable distribution function. In this case the Vlasov equation is replaced by a Fokker-Planck equation in order to capture the effect of collisions on the near threshold mode evolution.

A general theory [25] has been developed for describing the non-linear evolution of a wave satisfying the marginal stability criterion of Eq 6.1. It was theoretically shown in [25] that the mode evolution just above the threshold reflects an interplay between the wave electric field, that tends to flatten the distribution function of energetic particles, and the relaxation processes, which tend to restore the unstable distribution function with a characteristic time scale $1/\nu_{\text{eff}}$. The relaxation process restoring the unstable distribution function was modelled in [25] via an 'annihilation' (Krook [56]) collision operator that treats the effect of collisions as $-\nu_{\text{eff}}\,(F - F_0)$, with F_0 and F being the equilibrium and perturbed distribution functions respectively. Within this model it was found that a steady-state solution does not always establish itself near the threshold, and four main regimes of the near-threshold non-linear amplitude evolution have been predicted in [25] depending on the ratio of ν_{eff}/γ: 1) a steady-state regime; 2) a regime with periodic amplitude modulation; 3) a chaotic regime, and 4) an 'explosive' regime. The case of velocity space diffusion was also investigated in [26] and produced very similar non-linear behaviour to the Krook collisions (see figure 6.1).

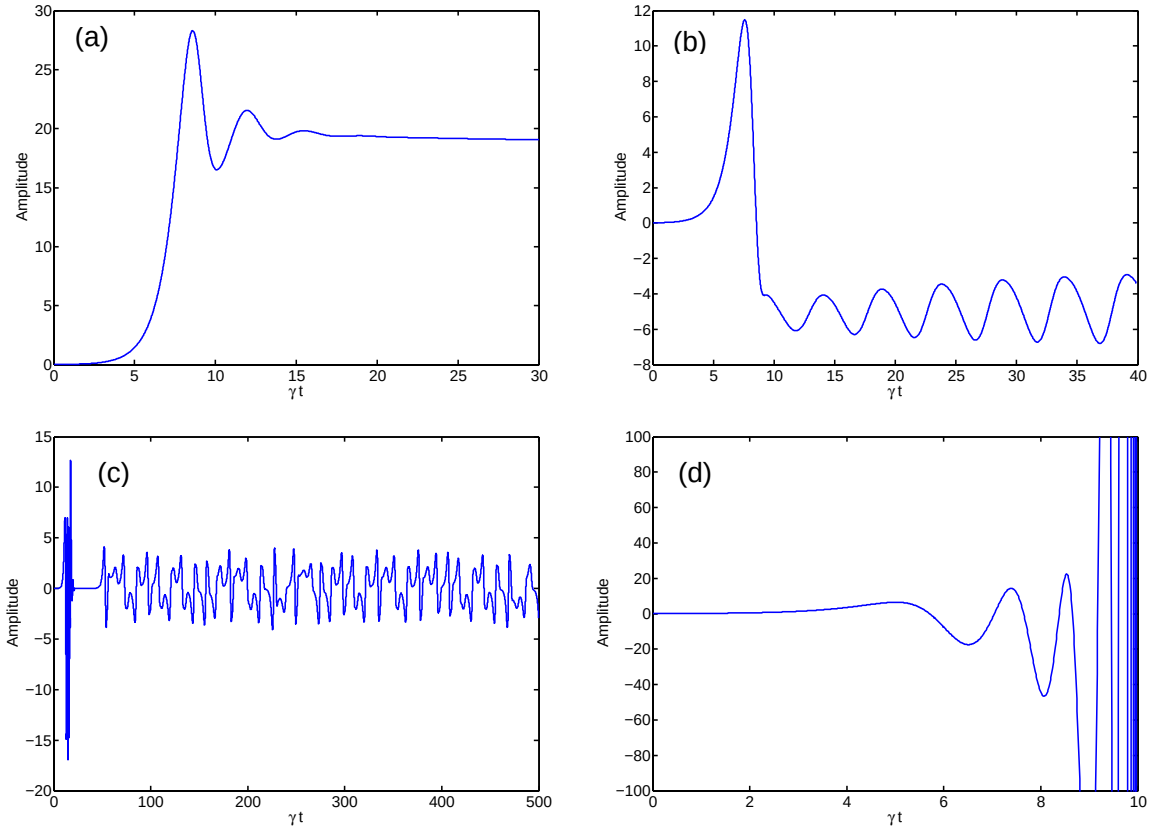

Figure 6.1: *Different regimes of marginally unstable amplitude evolution for velocity space diffusion collisions (a) steady state, (b) amplitude modulation (pitch fork splitting), (c) chaotic, (d) explosive [produced using Eq 6.14 with $\alpha = \beta = 0$, benchmarked against [24])*

6.2 Collisions

Collisions between particles in a plasma are notably different from those in a neutral gas. In contrast to neutral particles that collide at short range due to the intense electric field close to the atoms, and result in large angle scattering, plasma particles suffer small angle scattering due to the long range ($\sim \lambda_D$) electric field that exists in a plasma. The sum of these small events eventually leads to a large deviation from the particle's original trajectory, which is then termed a 'collision'. It is these distant collisions that dominate a plasma environment [57]. For fast particles such as NBI injected ions, the injection velocity v_f typically lies in the range $v_{Ti} \ll v_f \ll v_{Te}$ where v_{Ti} and v_{Te} are the background ion and electron thermal velocities respectively. Since the Coulomb cross section depends on the relative velocity of the

two colliding particles [57], collisions between fast ions and electrons will dominate at higher velocities, while those from thermal ions will dominate at lower velocities. There exists a critical energy (E_c) at which the energy flow from fast ions to thermal electrons and ions are comparable [9, 58]

$$E_c = 14.8 A_f T_e \left\langle \frac{Z_i^2}{A_i} \right\rangle^{2/3} \tag{6.2}$$

where T_e is the electron temperature in eV, A_f is the fast ion atomic number and

$$\left\langle \frac{Z_i^2}{A_i} \right\rangle = \frac{\sum_i n_i \left(Z_i^2/A_i\right) \ln \Lambda_i}{n_e \ln \Lambda_e} \tag{6.3}$$

is the average charge to mas ratio of the thermal ions ($\ln\Lambda_i, \ln\Lambda_e$ denote the Coulomb logarithms for ion-ion and ion-electron collisions). Above this energy the dominant collisional effect on the fast ions is an electron drag similar to a large ball rolling through a sea of marbles. Below E_c the thermal ion collisions dominate and, since the masses of the colliding particles are similar, the effect is to significantly alter the fast particle direction (pitch angle scattering) and energy (energy diffusion). These collisions can be described by their affect on the distribution function F, which is represented by a dynamical friction and diffusion in velocity space [59]

$$\left.\frac{dF}{dt}\right|_{coll} = -\nabla_v \cdot \left(F \left\langle \Delta \mathbf{v} \right\rangle\right) + \frac{1}{2} \nabla_v \cdot \left(\nabla_v \cdot \left(F \left\langle \Delta \mathbf{v} \otimes \Delta \mathbf{v} \right\rangle\right)\right) \tag{6.4}$$

where $\Delta \mathbf{v}$ is the change in velocity due to collisions, $\langle \ldots \rangle$ denotes velocity averaging, $\langle \Delta \mathbf{v} \rangle$ is called the coefficient of dynamical friction (drag) and $\langle \Delta \mathbf{v} \otimes \Delta \mathbf{v} \rangle$ is the diffusion tensor. Both dynamical friction and diffusion must be considered when obtaining the global equilibrium distribution function F_0. It can be the case however that only one collisional process dominates F_0 locally, e.g. well above the critical energy, where drag dominates. Roughly speaking

$$\text{Drag} \sim \frac{F}{v}, \qquad \text{Diffusion} \sim \frac{F}{v^2}, \tag{6.5}$$

demonstrating that for high velocity particles, drag is important, as was previously described. However it is incorrect to assume that only this process governs F in the presence of an unstable wave, as here fluctuations in F develop locally around the resonance, which generates small scales in phase space δv. In this case

$$\text{Drag} \sim \frac{F}{\delta v}, \qquad \text{Diffusion} \sim \frac{F}{(\delta v)^2} \tag{6.6}$$

which demonstrates that the formation of small scales in velocity space, due to the wave, can 'activate' the diffusive collision operator even in the region where drag dominates globally. More formally, the region of phase space that is significantly affected by the presence of the wave is a delta function (the resonance) in the absence of collisions. The effect of collisions in this sense is to give a width to the resonance in phase space, the greater this width the greater the influence of collisions on the wave evolution. This width essentially defines the volume in phase space that can be 'moved' into and out of resonance by collisions in a time scale of interest (in this case the growth time of the wave). From these considerations it may appear that the diffusive collision operator is the dominant one for the non-linear evolution of the wave, however it will be subsequently shown in section 6.5, that drag can in fact dominate. It is therefore necessary to include both effects in a theory of marginal stability.

6.3 Experimental observations

The first three regimes described in section 6.1 have been identified in JET experiments on Toroidal Alfvén Eigenmode (TAE) excitation by ICRH (ion cyclotron resonance heating) [23, 24] (Fig 6.2 top). Here, as the ICHR power increases, the steady state, amplitude modulated and chaotic regimes are seen in sequence. The Fourier space representation is seen as steady state frequency, side band formation ('pitch-fork' splitting), and 'fuzzy' frequency behaviour respectively. The explosive regime leading to a strongly non-linear phase was identified in MAST experiments with TAEs driven by NBI (neutral beam injection) [22] (Fig 6.2 bottom). Due to the strong non-linearity that develops in the explosive scenario, the instability on MAST was observed in the form of TAE 'bursts', representing a near-threshold type [60] of a general 'bursting' non-linear scenario described in [61]. A comparison of the non-linear TAE evolution [22] with that on other machines has shown that there is a tendency for NBI-driven Alfvénic instabilities to exhibit a bursting behaviour on NSTX [62], TFTR [63], DIII-D [64] and JT-60U [65]. On the other hand, ICRH-driven modes in the Alfvén frequency range, similar to those in [23,24],

show predominantly the first three types of mode evolution on TFTR [66], JT-60U [67], DIII-D [68] and C-MOD [69]. Taking into account that the distribution function of NBI-produced energetic ions establishes itself due to dynamical friction (also called electron drag and slowing down) [70], while the Stix type distribution function of ICRH-accelerated ions [71] is formed via a quasi-linear RF diffusive process, a comparison between dynamical friction and velocity-space diffusion becomes an important issue for kinetic instabilities. In this chapter such a comparison is made for a 'bump-on-tail' instability and extended to toroidal systems with the TAE instability.

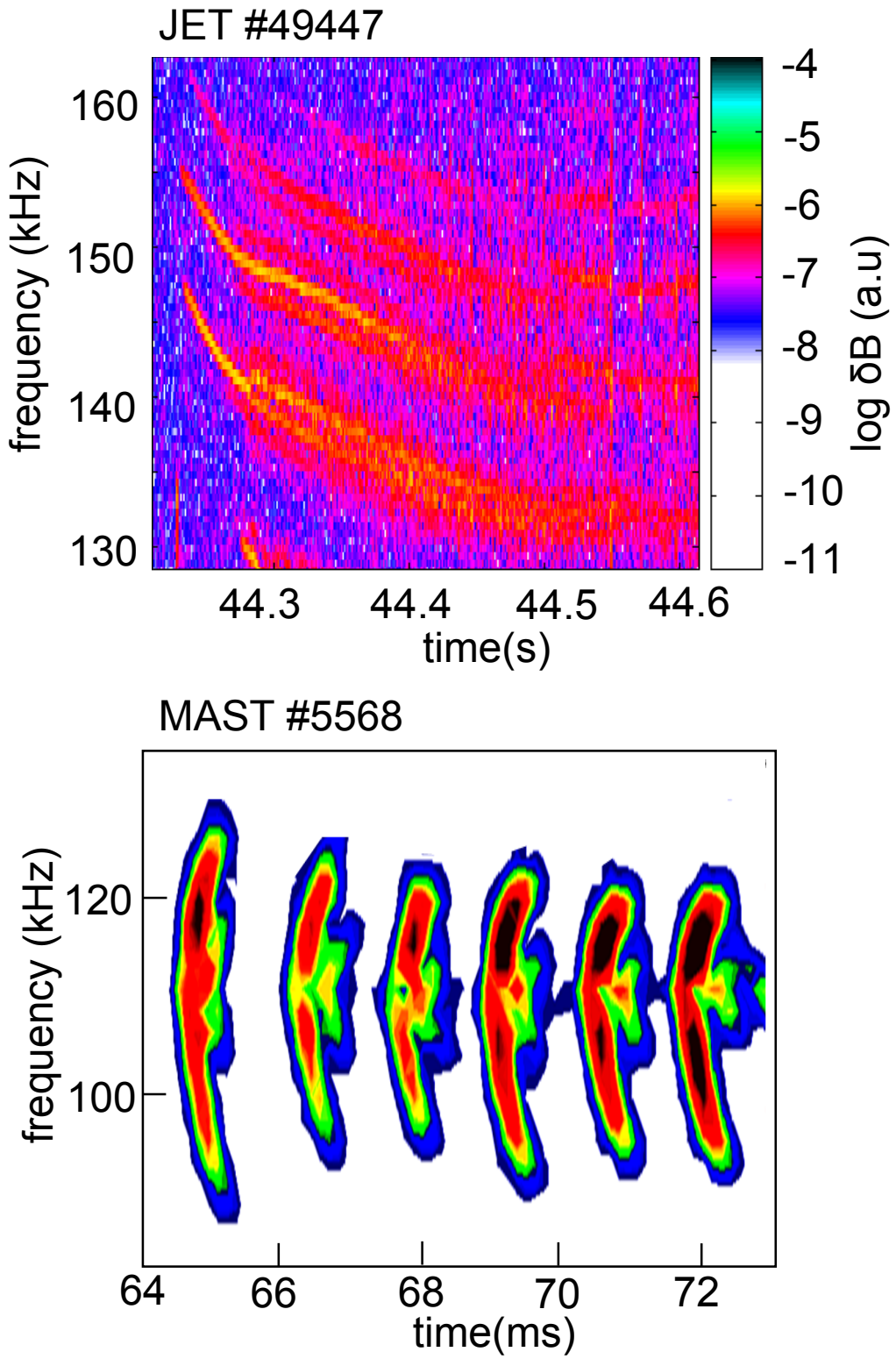

Figure 6.2: *Fourier spectrogram of a JET experiment with slowly increasing ICRH power showing steady state, followed by amplitude modulation and then chaotic behaviour [24] (top) and a MAST experiment with constant NBI power showing explosive behaviour seen as rapid frequency sweeping [22] (bottom).*

6.4 The bump-on-tail problem

In the aforementioned theory [25] the 'bump on tail' problem in a 1-D velocity space was considered for investigating the non-linear evolution of a marginally unstable electrostatic wave with frequency $\omega = \omega_{pe} = \sqrt{4\pi n_e e^2/m_e}$ in the presence of an unstable beam distribution $F(x, v, t)$. It can be shown [72], using a linear perturbation theory, that electrostatic perturbations, propagating with phase speed ω/k, will become unstable if the equilibrium distribution function F_0 satisfies Eq 6.7

$$\left.\frac{\partial F_0}{\partial v}\right|_{\frac{\omega}{k}} > 0. \tag{6.7}$$

Typically this configuration is achieved by injecting a beam component at high energy into a background thermal component as shown in Fig 6.3. In this case one describes the unstable perturbations as 'beam excited plasma waves'. Given this initially unstable wave, the distribution function will then evolve to reflect the energy transfer from the unstable distribution function to the wave itself. Particles 'move' from higher to lower energy resulting in a flattening of the distribution function at the resonance point in phase space ($v = \omega/k$) as illustrated in Fig 6.4 (the 'quasi-linear plateau' [73]), which eventually halts the progression of the wave. For the bump on tail case produced by beam injection, the constant flux of particles into and out of the resonance point limits the extent to which this plateau can inhibit the wave and, as alluded to in section 6.1, these processes can compete for a marginally unstable wave.

To describe this evolution in the presence of a wave with $E = \frac{1}{2}\left[\hat{E}(t)\, e^{i(kx-\omega t)} + \text{c.c}\right]$ the Fokker-Planck equation below must be solved

$$\frac{\partial F}{\partial t} + v\frac{\partial F}{\partial x} + \frac{e}{2m}\left[\hat{E}(t)\, e^{i(kx-\omega t)} + \text{c.c}\right]\frac{\partial F}{\partial v} = \left.\frac{dF}{dt}\right|_{\text{coll}} \tag{6.8}$$

together with Maxwell's equations for the electric field

$$\left[-i\omega_{pe}\frac{\partial \hat{E}(t)}{\partial t}e^{i(kx-\omega t)} + \text{c.c}\right] + 4\pi\frac{\partial j_f}{\partial t} = 0 \tag{6.9}$$

where $\hat{E}(t)$ is allowed to be complex to permit non-liner frequency shifting and j_f is the fast particle contribution to the perturbed current produced by the wave.

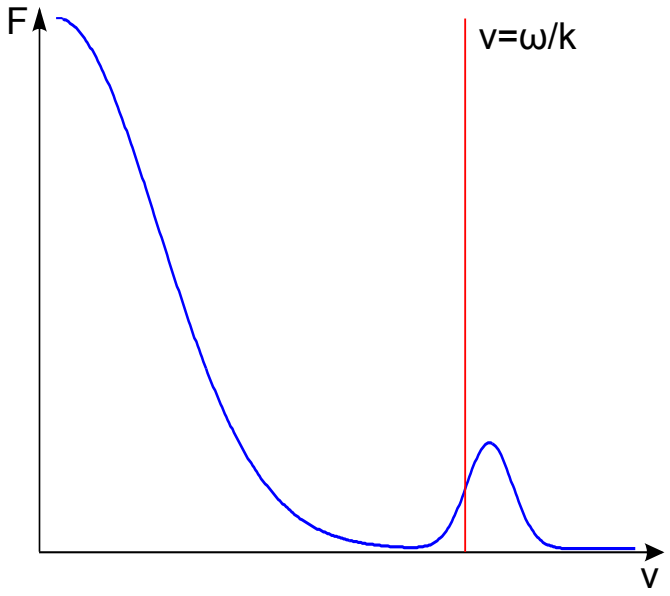

Figure 6.3: *Example of a typical bump on tail distribution function.*

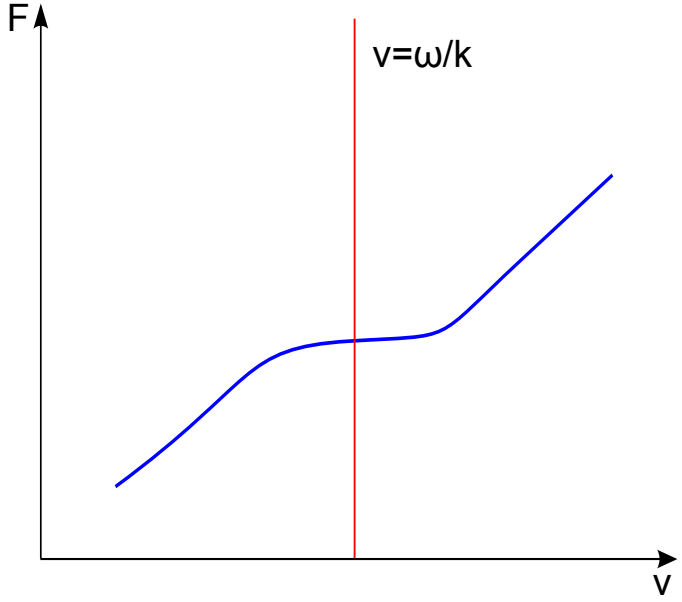

Figure 6.4: *Zoom of F from Fig 6.3, showing the formation of the quasi-linear plateau*

In Eq 6.9 it has been assumed that any change in $\hat{E}(t)$ occurs on a slower time scale than the wave frequency ω_{pe}, and that the fast particles to not significantly alter the wave frequency.

6.4.1 Extending the marginal stability model

Since only the resonant particles contribute significantly to the non-linear dynamics of the wave, F in Eq 6.8 can be taken as the distribution function of fast particles close to the resonance and not the global distribution function. Considering this, the collision operator in the vicinity of the resonance is represented by

$$\left.\frac{dF}{dt}\right|_{\text{coll}} = \alpha^2 \left(\frac{\partial F}{\partial u} - \frac{\partial F_0}{\partial u}\right) + \nu^3 \left(\frac{\partial^2 F}{\partial u^2} - \frac{\partial^2 F_0}{\partial u^2}\right) - \beta\left(F - F_0\right) \tag{6.10}$$

where α, ν and β are coefficients of drag, diffusion and Krook respectively and $u = kv - \omega$. In the case of Krook collisions β is defined to be a constant, however for drag and diffusion α and ν are taken as the values at the resonance point. By substituting the operators of Eq 6.10 into Eq 6.8, the relevant kinetic equation becomes

$$\frac{\partial F}{\partial t} + \left(\frac{u+\omega}{k}\right)\frac{\partial F}{\partial x} + \frac{ek}{2m}\left[\hat{E}\left(t\right)e^{i(kx-\omega t)} + \text{c.c}\right]\frac{\partial F}{\partial u} - \nu^3\frac{\partial^2 F}{\partial u^2} - \alpha^2\frac{\partial F}{\partial u} + \beta F = -\nu^3\frac{\partial^2 F_0}{\partial u^2} - \alpha^2\frac{\partial F_0}{\partial u} + \beta F_0 \tag{6.11}$$

which, together with Eq 6.9, will describe the dynamics of the system close to the resonance.

6.4.2 Weak Non-linearity approach

Since the wave is assumed to be sinusoidal in nature, the distribution function F is written as a Fourier series $F = F_0 + f_0 + \sum_{n=1}^{\infty}\left[f_n \exp\left(in\psi\right) + \text{c.c}\right]$ and $\psi = kx - \omega t$, which allows the wave equation in Eq 6.9 to be written as

$$\frac{\partial \hat{E}}{\partial t} + 4\pi e\frac{\omega}{k^2}\int f_1 du + \gamma_d \hat{E} = 0 \tag{6.12}$$

where wave damping due to the thermal plasma has been included explicitly.

A perturbative approach is taken so that the time-scales τ of interest are assumed to be small compared to the the non-linear bounce time (τ_B) of a particle in the wave field. In this way the distribution function F will not be significantly perturbed from its equilibrium value, permitting the ordering $F_0 \gg f_1 \gg f_0, f_2$ to be taken. F then admits a power series in $\hat{E}(t)$, which allows the first order non-linearity $\mathscr{O}\left(\hat{E}^3\right)$ to be captured by the following truncated Fourier expansion of of Eq 6.11 [25, 26]

$$\frac{\partial f_0}{\partial t} - \nu^3 \frac{\partial^2 f_0}{\partial u^2} - \alpha^2 \frac{\partial f_0}{\partial u} + \beta f_0 = -\frac{ek}{2m}\left(\hat{E}\frac{\partial f_1^*}{\partial u} + \text{c.c}\right) \tag{6.13a}$$

$$\frac{\partial f_1}{\partial t} + iuf_1 - \nu^3 \frac{\partial^2 f_1}{\partial u^2} - \alpha^2 \frac{\partial f_1}{\partial u} + \beta f_1 = -\frac{ek}{2m}\hat{E}\frac{\partial}{\partial u}\left(F_0 + f_0 + f_2\right) \tag{6.13b}$$

$$\frac{\partial f_2}{\partial t} + 2iuf_2 - \nu^3 \frac{\partial^2 f_2}{\partial u^2} - \alpha^2 \frac{\partial f_2}{\partial u} + \beta f_2 = -\frac{ek}{2m}\hat{E}^*\frac{\partial f_1}{\partial u} + \mathscr{O}\left(\hat{E}f_3\right). \tag{6.13c}$$

For a marginally unstable wave Eq 6.12 implies that the non-linear terms can compete with the linear terms when the non-linearity is still small, which implies that the truncated kinetic equation Eq 6.13 should describe the non-linear marginally unstable mode evolution. For a sufficiently large collision frequency this perturbative approach can be maintained indefinitely so long as $\nu_{\text{eff}} \gg \omega_B \equiv \left(ek\hat{E}/m\right)^{1/2}$ [26]. By comparing the second term in Eq 6.13b to the collision terms separately, resonance widths can be constructed to characterize the role of various collisions at the wave-particle resonance with $\Delta u_\nu = \nu$, $\Delta u_\alpha = \alpha$ and $\Delta u_\beta = \beta$ for diffusive, drag and Krook collisions respectively.

Eq 6.13 is solved iteratively for f_1, and hence for the electric field from Eq 6.12, noting that f_2 does not contribute to the final expression for the wave amplitude, and so it will subsequently be dropped from the analysis (see appendix B). Specifically f_1 is obtained by first neglecting f_0, which gives the linear response of the plasma to the wave. Secondly f_0 is obtained using this f_1 and then finally f_1 is subsequently solved for using this f_0 to obtain to first non-linear correction to the wave amplitude. The resulting equation for the evolution of the wave amplitude takes the following form (see appendix B)

$$\frac{dA}{d\tau} = A\left(\tau\right) - \frac{1}{2}\int_0^{\tau/2} dz\, z^2 A\left(\tau - z\right) \int_0^{\tau-2z} dx\, e^{-\hat{\nu}^3 z^2(2z/3+x) - \hat{\beta}(2z+x) + i\hat{\alpha}^2 z(z+x)} \times A\left(\tau - z - x\right) A^*\left(\tau - 2z - x\right) \tag{6.14}$$

where $A = \left[ek\hat{E}(t)/m(\gamma_l - \gamma_d)^2\right][\gamma_l/(\gamma_l - \gamma_d)]^{1/2}$, $\tau = (\gamma_l - \gamma_d)t$, $\hat{\nu}^3 = \nu^3/(\gamma_l - \gamma_d)^3$, $\hat{\alpha} = \alpha/(\gamma_l - \gamma_d)^2$, $\hat{\beta} = \beta/(\gamma_l - \gamma_d)$ and $\gamma_l = 2\pi^2(e^2\omega/mk^2)\partial F_0(\omega/k)/\partial v$.

The non-linear contribution to the amplitude is governed by a sophisticated time integration over the history of the wave, and provides a stabilising effect so long as the minus sign in front of the integral is preserved. In this case a saturated steady state is possible in the form $A_0 = |A_0|\exp(ib\tau)$ as $\tau \to \infty$. Assuming the integral in Eq 6.14 converges in this limit, the steady state solution will satisfy

$$ibA_0 = A_0 - A_0|A_0|^2 I \tag{6.15}$$

where

$$I = \frac{1}{2}\int_0^\infty dz\, z^2 \int_0^\infty dx\, e^{-\hat{\nu}^3 z^2(2z/3+x)-\hat{\beta}(2z+x)+i\hat{\alpha}^2 z(z+x)}. \tag{6.16}$$

It can then be demonstrated that

$$b = -\frac{\mathrm{Im}\{I\}}{\mathrm{Re}\{I\}}, \qquad |A_0|^2 = \frac{1}{\mathrm{Re}\{I\}}, \tag{6.17}$$

from which it can be concluded that steady state solutions to Eq 6.14 cannot exist if I has a negative real part.

The case of no dynamical friction, $\hat{\alpha} = 0$, in Eq 6.14 was previously considered in [26] and the non-linear amplitude evolution was divided into soft and hard non-linear regimes. In the soft case the amplitude evolves to a low level, reflecting the closeness to the instability threshold, whereas the hard case leads to a solution which blows up in a finite time $A \sim (t - t_0)^{-p}$, the so called 'explosive' solution. The inclusion of a non-zero $\hat{\alpha}$ introduces an oscillatory dependence to the integral, which has a profound effect on the non-linear behaviour of the mode amplitude, as the integral in Eq 6.14 can then easily change sign. In this case no steady state solution is possible and the 'explosive' solution is expected.

The physical significance of this observation can be understood by solving Eq 6.13a for the complimentary function. For pure Krook and pure diffusion, perturbations to the distribution function decay in time as $f_0 \sim e^{-\beta t}$ and $f_0 \sim e^{-\frac{u^2}{4\nu^3 t}}/\sqrt{\nu^3 t}$ respectively, destroying the history of the perturbations. For pure drag however the solution takes the form of an advecting profile $f_0 \sim f_0(u + \alpha^2 t)$, which retains

a 'memory' in some sense. This can also be understood by noting the parity of the operators with respect to time in Eq 6.11. Both Krook and diffusion operators have odd parity, whereas drag has an even parity. Even parity operators leave the equation unchanged if time is reversed, indicating that drag is a reversible process and allows the plasma to retain a 'memory'. However, Krook and diffusion break this time reversal symmetry indicating irreversibility, and decorrelation of collisional events after some time.

6.4.3 Numerical considerations

To solve Eq 6.14, a MatLab code has been developed using a similar numerical scheme to that of R. F. Heeter [74], which uses a finite difference scheme and utilises a recurrence relation technique to reduce the computational intensity of the integral. The finite difference version of Eq 6.14 can be written as

$$A\left(j+1\right)=A\left(j\right)+A\left(j\right)\Delta\tau+C_1\sum_{k=1}^{j/2}A\left(j-k\right)S\left(j,k\right) \tag{6.18}$$

where $C_1=-\Delta\tau^5/2$. By changing variables to $\xi=\tau-2z-x$ in the x integral, $S\left(j,k\right)$ can then be written as

$$S\left(j,k\right)=\sum_{l=0}^{j-2k}e^{C_2(l-j)+C_3k^2(4k/3+l-j)+iC_4k(j-l-k)}A\left(l+k\right)A\left(l\right) \tag{6.19}$$

where $C_2=\hat{\beta}\Delta\tau$, $C_3=\hat{\nu}^3\Delta\tau^3$, $C_4=\hat{\alpha}^2\Delta\tau^2$. The following recurrence relation is then used to reduce the computational intensity of the simulation

$$S\left(j,k\right)=e^{-C_2-C_3k^2+iC_4k}S\left(j-1,k\right)+e^{-2kC_2-2C_3k^3/3+iC_4k^2}A\left(j-k\right)A\left(j-2k\right). \tag{6.20}$$

The code was benchmarked against results obtained in [24] and was found to agree, as can be seen in Fig 6.1.

6.4.4 Pure drag

For the case of pure drag $\left(\hat{\nu}=\hat{\beta}=0\right)$ the amplitude evolution is always of explosive type and blows up in a finite time. In this case Eq 6.14 does not admit steady state

solutions for any value of $\hat{\alpha}$. This can be demonstrated by letting $\tau \to \infty$ in the integral of Eq 6.14, which gives

$$\lim_{\tau\to\infty} \int_0^{\tau/2} dz \frac{z}{i\hat{\alpha}^2} \left[e^{i\hat{\alpha}^2 z(\tau - z)} - e^{i\hat{\alpha}^2 z^2} \right]. \tag{6.21}$$

This integral will not converge due to the existence of the $(\tau - z)$ term in the first exponential. The numerical evaluation of Eq 6.14 also supports this as can be seen in Fig 6.5. This is in contrast to the previously studied of Krook and diffusive cases.

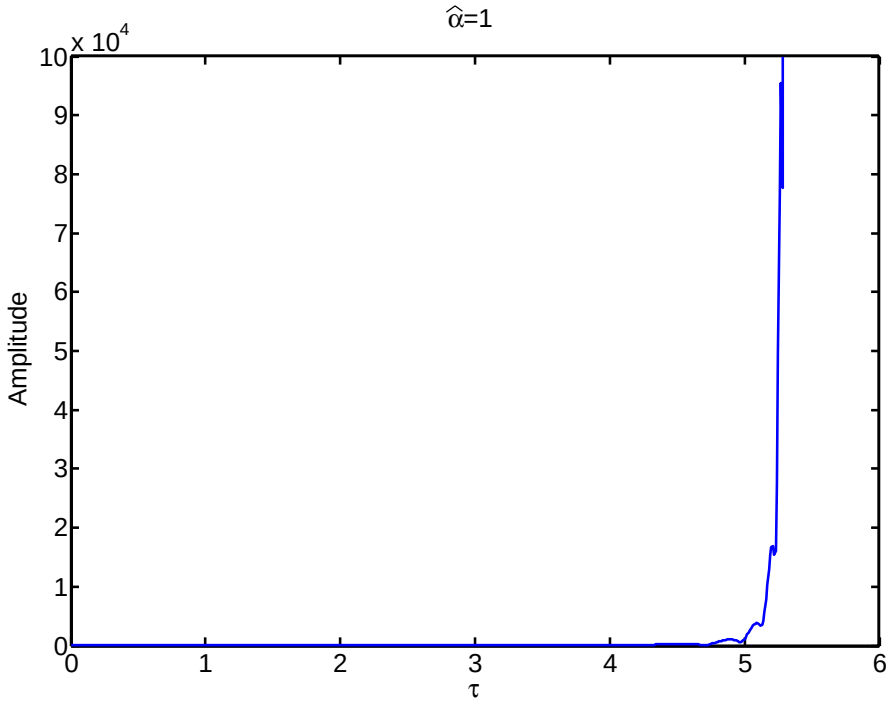

Figure 6.5: *Amplitude evolution for the pure drag case, with initial perturbation* $A = 1$ *and time step* $\Delta\tau = 0.01$*, showing explosive behaviour* $A \sim (t - t_0)^{-p}$.

6.4.5 Drag and Diffusion

By adding diffusion along with drag, steady state solutions to Eq 6.14 can exist for small amounts of drag (see Fig 6.6 (top)) with

$$|A_0|^{-2} = \frac{1}{2}\mathrm{Re}\left\{ \int_0^{\infty} \frac{z}{z\hat{\nu}^3 - i\hat{\alpha}} e^{-2\hat{\nu}^3 z^3/3 + i\hat{\alpha}z^2} \, dz \right\}. \tag{6.22}$$

However, when $\hat{\nu}/\hat{\alpha} < 1.043$, I in Eq 6.16 acquires a negative real part that prohibits the existence of a steady state (figure 6.6 (bottom)). For those parameters which

exhibit a steady state, the behaviour of the amplitude as a function of the drag parameter $\hat{\alpha}$ can be seen in Fig 6.7

The stability of the steady state solutions is also of interest, unstable solutions lead to the amplitude modulated and chaotic regimes seen in Fig 6.1. By perturbing the steady state solution $A = A_0\left(1+\delta A\right)$, where $\delta A = C\exp\left(\lambda\tau\right) + D\exp\left(\lambda^*\tau\right)$, Eq 6.14 reduces to a dispersion relation for λ (see appendix B)

$$
\begin{aligned}
0 = &\left\{\lambda + ib - 1 + \frac{\left|A_0\right|^2}{2}\int_0^\infty dz\, P\left(z\right)\left[\frac{e^{-\lambda z}}{\hat{\nu}^3 z^2 - i\hat{\alpha}^2 z + \lambda} + \frac{e^{-\lambda z}}{\hat{\nu}^3 z^2 - i\hat{\alpha}^2 z}\right]\right\} \\
&\times\left\{\lambda - ib - 1 + \frac{\left|A_0\right|^2}{2}\int_0^\infty dz\, P^*\left(z\right)\left[\frac{e^{-\lambda z}}{\hat{\nu}^3 z^2 + i\hat{\alpha}^2 z + \lambda} + \frac{e^{-\lambda z}}{\hat{\nu}^3 z^2 + i\hat{\alpha}^2 z}\right]\right\} \\
&-\left\{\frac{\left|A_0\right|^2}{2}\int_0^\infty dz\, P\left(z\right)\frac{e^{-2\lambda z}}{\hat{\nu}^3 z^2 - i\hat{\alpha}^2 z + \lambda}\right\}\times\left\{\frac{\left|A_0\right|^2}{2}\int_0^\infty dz\, P^*\left(z\right)\frac{e^{-2\lambda z}}{\hat{\nu}^3 z^2 + i\hat{\alpha}^2 z + \lambda}\right\}.
\end{aligned}
\tag{6.23}
$$

where $P\left(z\right) = z^2\exp\left(-2\hat{\nu}^3 z^3/3 + i\hat{\alpha}^2 z^2\right)$. For large values of $\hat{\nu}$ the amplitude saturates to the steady state, as seen in Figure 6.6 (top), which implies that $\mathrm{Re}\left\{\lambda\right\} < 0$. It is reasonable to assume that, as $\hat{\nu}$ is lowered, λ changes continuously until $\mathrm{Re}\left\{\lambda\right\} > 0$ when the solution becomes unstable. The point at which $\mathrm{Re}\left\{\lambda\right\} = 0$ will therefore define a stability boundary in $\hat{\nu}, \hat{\alpha}$ space. The resultant boundary is displayed in Fig 6.8. From Fig 6.8 it can be seen that the addition of drag is in general destabilising. The unstable regimes exist in the narrow region between the blue and red lines.

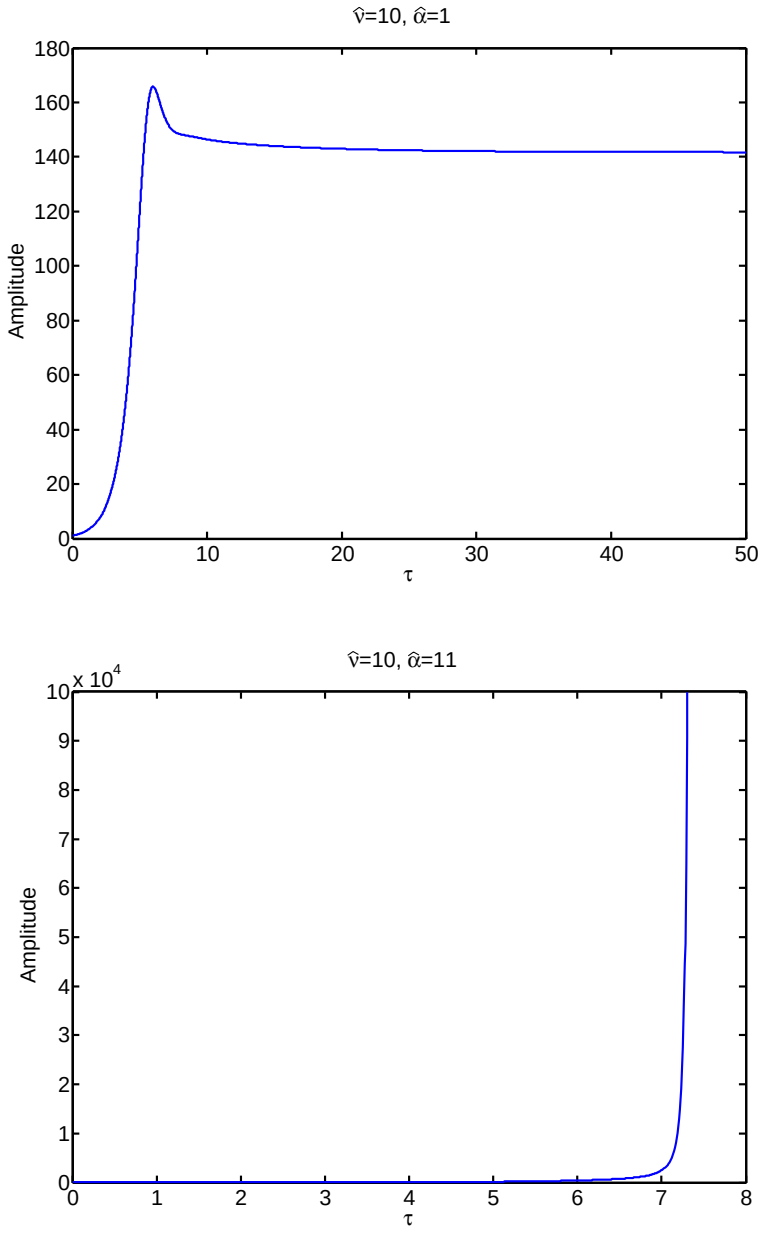

Figure 6.6: *Numerical solution of Eq 6.14 showing the amplitude evolution for the drag + diffusive case, with initial perturbation* $A = 1$ *and time step* $\Delta\tau = 0.01$*, showing steady state behaviour (top) and explosive behaviour (bottom).*

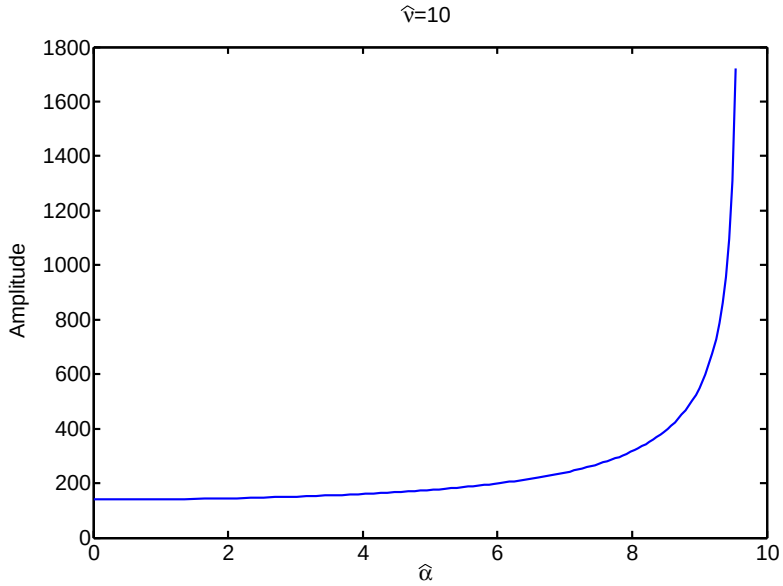

Figure 6.7: *Amplitude for the diffusive + drag case in Eq 6.22, which increases as a function of* $\hat{\alpha}$

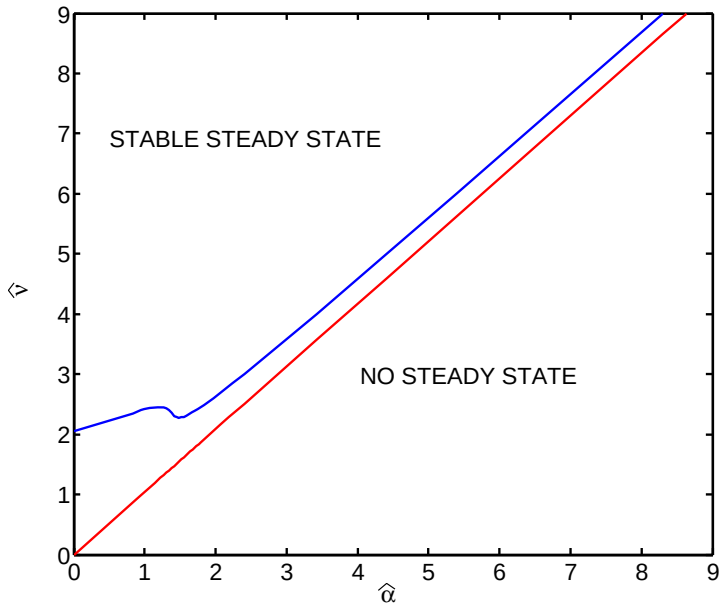

Figure 6.8: *Displays the boundaries in parameter space that give stable, unstable and no steady state solution to Eq 6.14*

Solving 6.14 numerically confirms that amplitude modulated regimes do exist in the diffusion + drag case (figure 6.9). However the chaotic regimes have yet to be confirmed, as the inclusion of the oscillatory dependence from the drag term necessitates very small time steps to resolve the chaotic regime.

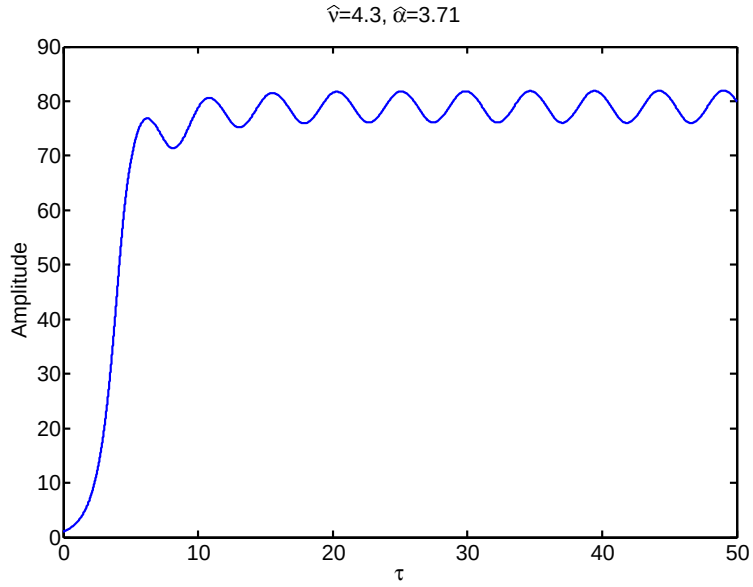

Figure 6.9: *Numerical solution of Eq 6.14 showing amplitude evolution for the drag + diffusive case, with initial perturbation* $A = 1$ *and time step* $\Delta\tau = 0.005$*, showing modulated amplitude behaviour.*

The destabilising effect of drag can also be seen from the perturbed distribution function. For convenience Eq 6.13 is expressed in terms of the normalised parameters in Eq 6.14, including $\hat{u} = u/(\gamma_l - \gamma_d)$, $\hat{F} = F(\gamma_l - \gamma_d)^2/(mk/2\pi^2 e^2\omega)$ and $f_1 = -Af$ to give the steady state distribution function equations

$$-\hat{\alpha}^2\frac{\partial \hat{f}_0}{\partial \hat{u}} - \hat{\nu}^3\frac{\partial^2 \hat{f}_0}{\partial u^2} = |A_0|^2 \,\mathrm{Re}\left(\frac{\partial \hat{f}}{\partial \hat{u}}\right) \tag{6.24a}$$

$$i\hat{u}\hat{f} - \hat{\alpha}^2\frac{\partial \hat{f}}{\partial \hat{u}} - \hat{\nu}^3\frac{\partial^2 \hat{f}}{\partial \hat{u}^2} = \frac{1}{2}. \tag{6.24b}$$

where $\partial/\partial\tau = 0$ has been taken for simplicity (inclusion simply shifts the origin).

The solutions to Eq 6.24 are found to be (see appendix B)

$$\hat{f}_0 = -\frac{|A_0|^2}{2\hat{\nu}^3}\mathrm{Re}\left\{\int_0^\infty e^{-y^3/3-iy^2\hat{\alpha}^2/2\hat{\nu}^2}\left[\frac{e^{-iy\hat{u}/\hat{\nu}}}{\hat{\alpha}^2/\hat{\nu}^2-iy}\right]dy\right\} \tag{6.25}$$

$$\hat{f} = \frac{1}{2\hat{\nu}}\int_0^\infty e^{-iy(\hat{u}/\hat{\nu})-iy^2\hat{\alpha}^2/2\hat{\nu}^2-y^3/3}\,dy. \tag{6.26}$$

Since the above equations describe the behaviour of the Fourier coefficients of F, the actual distribution will contain the equilibrium part F_0, a rapidly oscillating part from the f term, and a slowly varying part from f_0. Therefore over long time-scales compared to the wave period, $F = F_0 + f_0$ provides information about the form of the steady state distribution function in the presence of the wave.

PURE DIFFUSION Considering firstly the case when the collisions are dominated by a purely diffusive process ($\hat{\alpha} = 0$), Eq 6.22 can be evaluated explicitly to be $|A_0|^2 = 2^{4/3}\times 3^{2/3}\times\hat{\nu}^4/\Gamma(1/3)$, where Γ here is the gamma function ($\Gamma(1/3) \approx 2.68$). Given this fact $\hat{f}_0$ is reduced to

$$\hat{f}_0 = -\frac{2^{1/3}\times 3^{2/3}\hat{\nu}}{\Gamma(1/3)}\int_0^\infty e^{-y^3/3}\frac{\sin(y\hat{u}/\hat{\nu})}{y}\,dy, \tag{6.27}$$

from which it can be seen that $\hat{f}_0 \to \mp 3^{2/3}\hat{\nu}\pi/2^{2/3}\Gamma(1/3)$ as $\hat{u} \to \pm\infty$, which is confirmed by a numerical evaluation of Eq 6.27 displayed in Fig 6.10

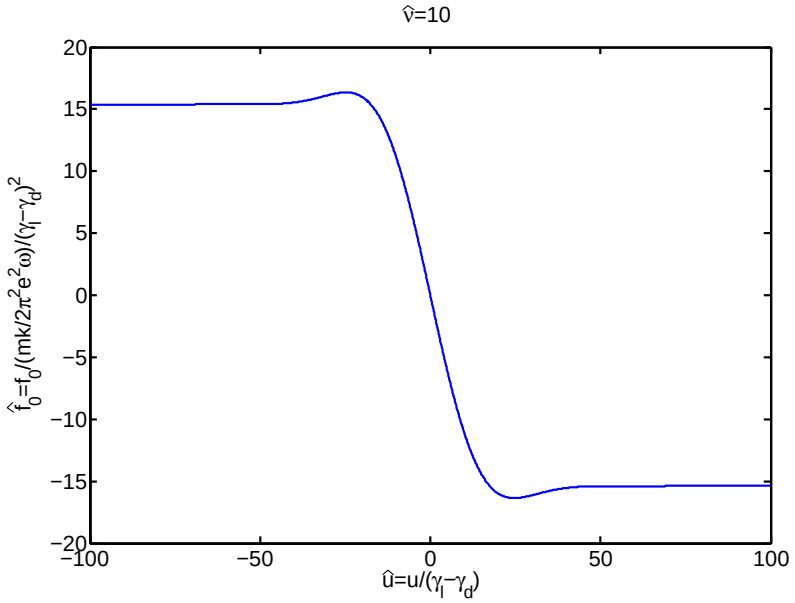

Figure 6.10: *Numerical evaluation of Eq 6.27*

For the bump on tail case, F_0 close to the resonance is a straight line with constant gradient of $\partial\hat{F}_0/\partial\hat{u} = \gamma_l/\left(\gamma_l - \gamma_d\right)$ in the chosen normalisation. $\hat{F}\left(=\hat{F}_0+\hat{f}_0\right)$ is calculated for two cases; 1: $\hat{\nu} = 10, 20, 40$, $\gamma_l = 0.1s^{-1}$, $\gamma_l - \gamma_d = 0.5\gamma_l$ (Fig 6.11 top), and case 2: $\hat{\nu} = 10$, $\gamma_l = 0.1s^{-1}$, $\gamma_l - \gamma_d = 0.5\gamma_l, 0.7\gamma_l, 0.9\gamma_l$ (Fig 6.11 bottom).

As previously discussed the effect of the wave is to flatten the distribution function close to the resonance point. Fig 6.11 (top) confirms this and is consistent with a system driven to saturation. As $\hat{\nu}$ is increased the flattened region increases but the shape of F remains unchanged, demonstrating a stable saturation. Fig 6.11 (bottom) however shows that increasing the drive of the wave eventually results in the distribution function reversing its gradient at the resonance point. In this case the theory of marginal stability breaks down signifying the onset of a hard non-linear regime. This is confirmed by using Eq 6.27 to find that the gradient reverses sign at the resonance when $\gamma/\gamma_l > 2^{-1/3}$ is satisfied.

DIFFUSION + DRAG To understand the effect of drag on the distribution function an artificially large drag coefficient is used to produce the perturbed f_0 shown in Fig 6.12. One can view the the effect of drag as that of a flowing river and the resonance as that of a rock in the flow. Upstream the flow is unperturbed

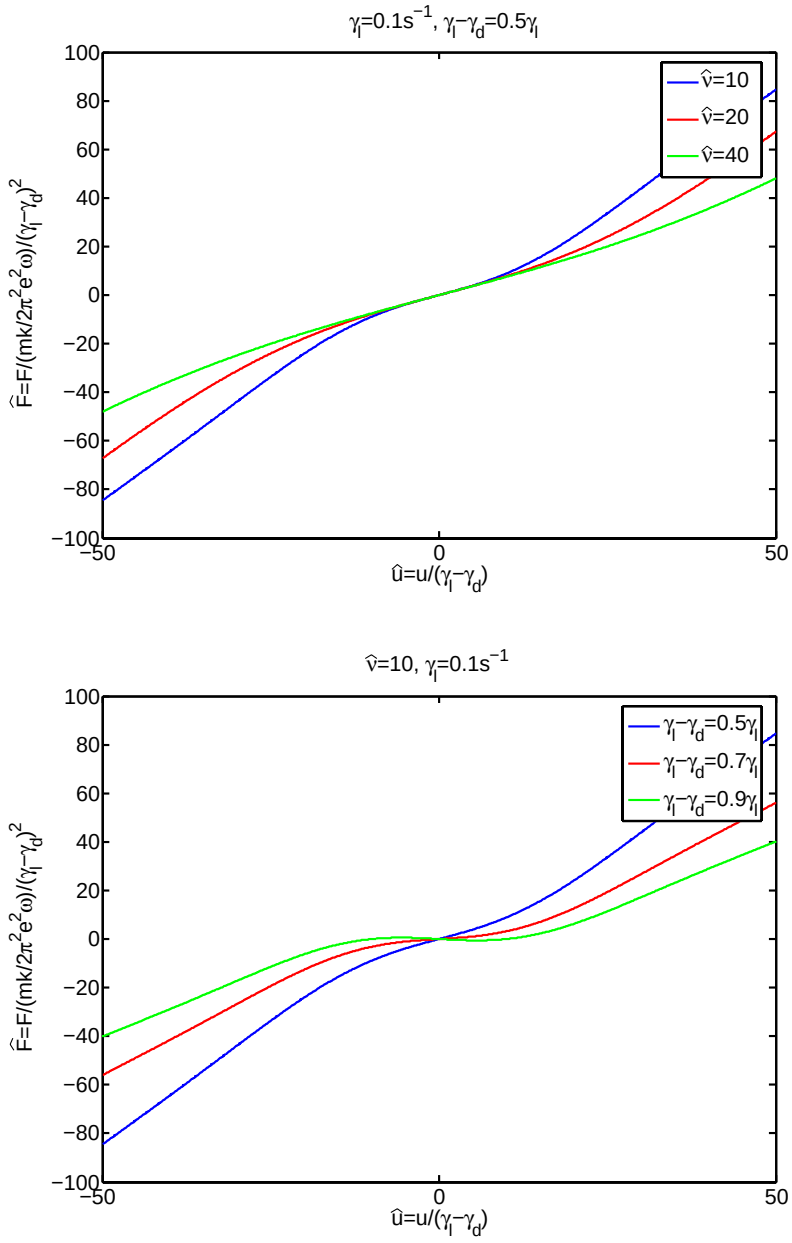

Figure 6.11: *Saturated distribution function for the pure diffusion case*

($u > 0$ in Fig 6.12) and downstream of the rock the flow is significantly perturbed ($u < 0$ in Fig 6.12).

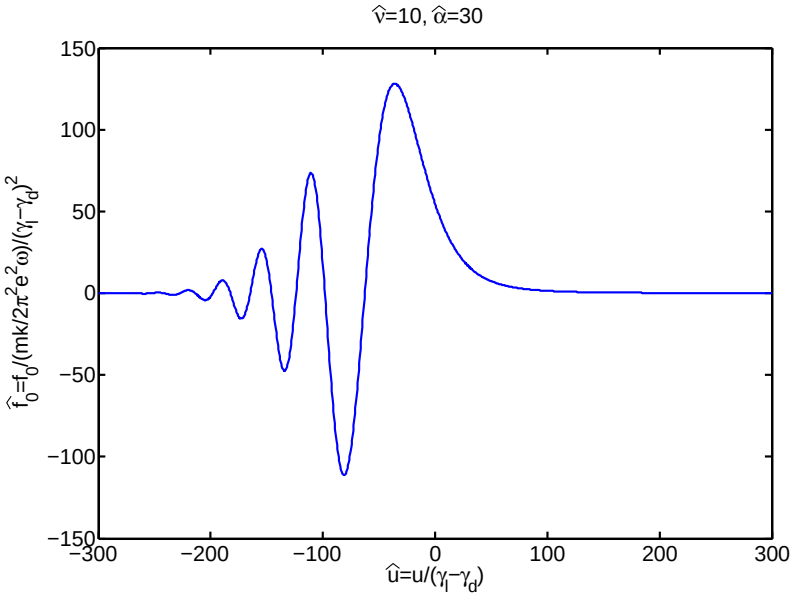

Figure 6.12: *f_0 for diffusion and an artificially large amount of drag to illustrate the oscillatory behaviour of the drag.*

Using more realistic parameters $\hat{\nu} = 10$, $\hat{\alpha} = 0, 3.2, 4.5, 6.3$, $\gamma_l = 0.1s^{-1}$, $\gamma_l - \gamma_d = 0.5\gamma_l$, (Figure 6.13) demonstrates that, by adding a significant slowing down component to the collision term, large perturbations in the distribution are formed. As $|\hat{\alpha}|$ increases, these perturbations deepen. By comparing this to the purely diffusive case with increasing γ one can conclude that the perturbative approach of this analysis breaks down and indicates that the system is being driven towards a hard non-linear regime.

6.4.6 Drag and Krook

The addition of Krook collisions to the drag collision operator is dealt with using the procedures developed for the 'diffusive and drag' case in section 6.4.5, and the results are qualitatively very similar. The existence of steady state solutions to Eq 6.14 is prohibited for $\hat{\beta}/\hat{\alpha} < 1.02$. For the steady state solutions that do exist their

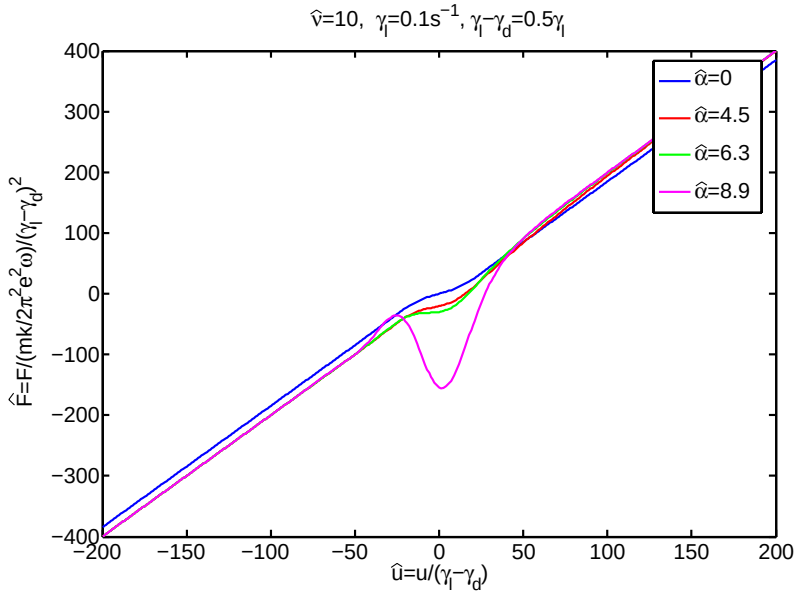

Figure 6.13: *Saturated distribution function for the diffusive + drag case varying the drag parameter* $\hat{\alpha}$

amplitude satisfies

$$|A_0|^{-2} = \frac{1}{2}\mathrm{Re}\left\{\int_0^\infty \frac{z^2}{\beta - i\hat{\alpha}z} e^{-2\hat{\beta}z + i\hat{\alpha}z^2}\, dz\right\}, \tag{6.28}$$

and the dependence of the amplitude on the drag parameter can be illustrated in Fig 6.14. The stability properties of the steady state with Krook and drag collisions are governed by the following dispersion relation

$$\begin{aligned} 0 = &\left\{\lambda + ib - 1 + \frac{|A_0|^2}{2}\int_0^\infty dz\, P(z)\left[\frac{e^{-\lambda z}}{\hat{\beta} - i\hat{\alpha}^2 z + \lambda} + \frac{e^{-\lambda z}}{\hat{\beta} - i\hat{\alpha}^2 z}\right]\right\} \\ &\times\left\{\lambda - ib - 1 + \frac{|A_0|^2}{2}\int_0^\infty dz\, P^*(z)\left[\frac{e^{-\lambda z}}{\hat{\beta} + i\hat{\alpha}^2 z + \lambda} + \frac{e^{-\lambda z}}{\hat{\beta} + i\hat{\alpha}^2 z}\right]\right\} \\ &-\left\{\frac{|A_0|^2}{2}\int_0^\infty dz\, P(z)\frac{e^{-2\lambda z}}{\hat{\beta} - i\hat{\alpha}^2 z + \lambda}\right\}\times\left\{\frac{|A_0|^2}{2}\int_0^\infty dz\, P^*(z)\frac{e^{-2\lambda z}}{\hat{\beta} + i\hat{\alpha}^2 z + \lambda}\right\}. \end{aligned} \tag{6.29}$$

where $P(z) = z^2 \exp\left(-2\hat{\beta}z + i\hat{\alpha}^2 z^2\right)$. From this a stability boundary is obtained

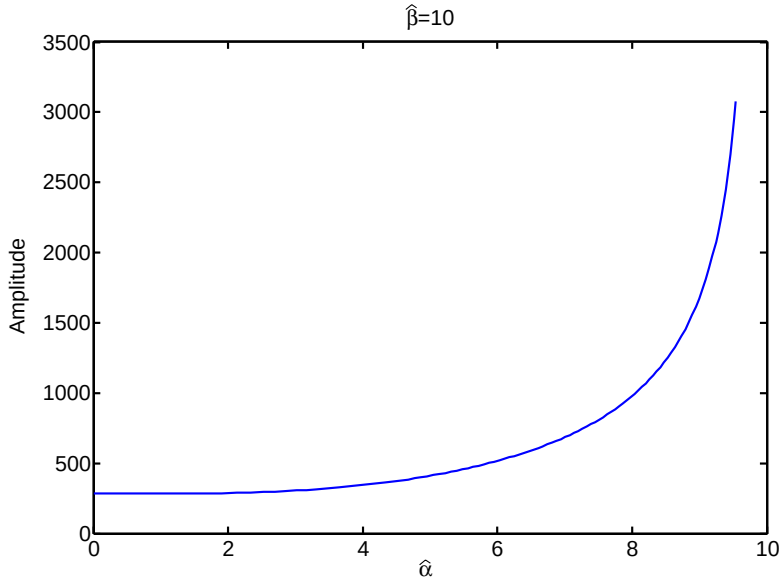

Figure 6.14: *Amplitude for the krook + drag case in Eq 6.22, which increases as a function of* $\hat{\alpha}$

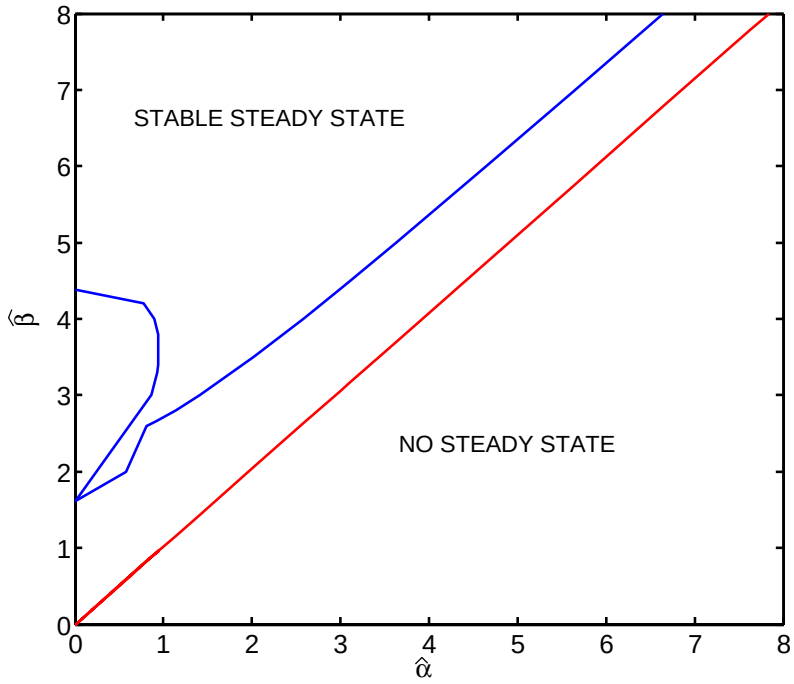

Figure 6.15: *Displays the boundaries in parameter space for Krook + drag that give stable, unstable and no steady state solution to Eq 6.14*

in the same way as in section 6.4.5 to yield Fig 6.15. As with section 6.4.5 Eq 6.13 is re-expressed in terms of normalised parameters, to give the steady state distribution function equations

$$-\hat{\alpha}^2\frac{\partial \hat{f}_0}{\partial \hat{u}} + \hat{\beta}\hat{f}_0 = |A_0|^2 \,\mathrm{Re}\left(\frac{\partial \hat{f}}{\partial \hat{u}}\right) \tag{6.30a}$$

$$i\hat{u}\hat{f} - \hat{\alpha}^2\frac{\partial \hat{f}}{\partial \hat{u}} + \hat{\beta}\hat{f} = \frac{1}{2}. \tag{6.30b}$$

the solutions of which are given by

$$\hat{f}_0 = \mathrm{Re}\left\{-\frac{1}{2}|A_0|^2 \int_0^\infty \frac{iy}{\hat{\beta} + i\hat{\alpha}^2 y} e^{-\hat{\beta}y - i\hat{u}y - i\hat{\alpha}^2 y^2/2} dy\right\} \tag{6.31}$$

$$\hat{f} = \frac{1}{2}\int_0^\infty e^{-\hat{\beta}y - i\hat{u}y - i\hat{\alpha}^2 y^2/2} dy \tag{6.32}$$

PURE KROOK Considering firstly the case when the collisions are dominated by a purely Krook process ($\hat{\alpha} = 0$) Eq 6.28 is evaluated explicitly to give $|A_0|^2 = 8\hat{\beta}^4$. Given this fact $\hat{f}_0$ is then be reduced to

$$\hat{f}_0 = -\frac{8\hat{u}\hat{\beta}^4}{\left(\hat{\beta}^2 + \hat{u}^2\right)^2} \tag{6.33}$$

from which it can be seen that $\hat{f}_0$ has extrema of $\hat{f}_0(\hat{u}_0) = \mp 3\hat{\beta}\sqrt{3}/2$ at $\hat{u}_0 = \pm\hat{\beta}/\sqrt{3}$, which is confirmed by a numerical evaluation of Eq 6.33 displayed in Fig 6.16.

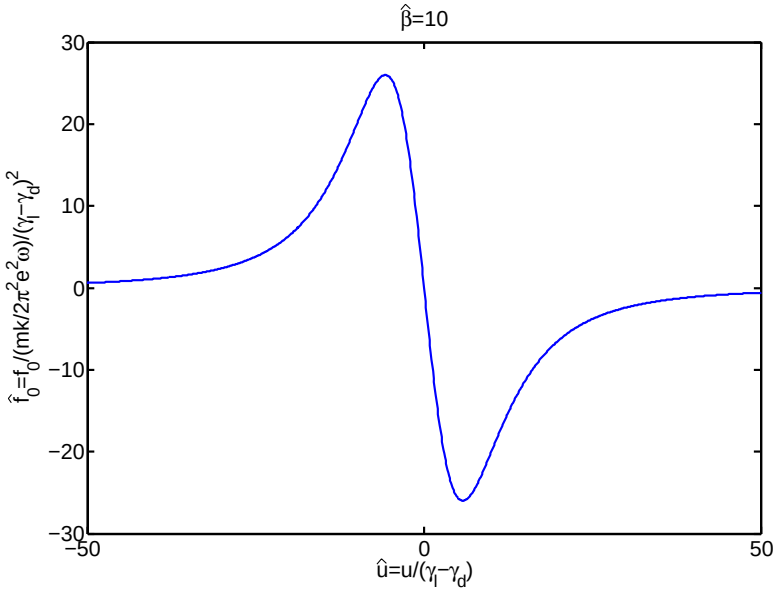

Figure 6.16: *Numerical evaluation of Eq 6.33*

As with section 6.4.5 the slowing varying saturated distribution function $\hat{F}\left(=\hat{F}_0+\hat{f}_0\right)$ is calculated for the pure Krook for two cases; 1: $\hat{\beta}=10,20,40$, $\gamma_l=0.05s^{-1}$, $\gamma_l-\gamma_d=0.05\gamma_l$ (Fig 6.17 top), and case 2: $\hat{\beta}=10$, $\gamma_l=0.05s^{-1}$, $\gamma=0.05\gamma_l,0.1\gamma_l,0.2\gamma_l,0.4\gamma_l$ (Fig 6.17 bottom). As with the diffusive + drag case, the distribution function reverses its gradient at the origin when $\gamma/\gamma_l>8^{-1}$. A comparison with the pure diffusive case shows that marginally unstable modes evolving due to Krook collisions depart from the applicability conditions of this model before those evolving due to diffusive collisions.

KROOK + DRAG As with the diffusive case, the effect of drag is seen to significantly perturb the distribution function downstream as shown in Fig 6.18 and the resulting distribution function for more realistic parameters $\hat{\beta}=10$, $\hat{\alpha}=4.5,6.3,8.9$, $\gamma_l=0.05s^{-1}$, $\gamma_l-\gamma_d=0.05\gamma_l$, (Fig 6.19) demonstrates that drag continues to provide a destabilising influence.

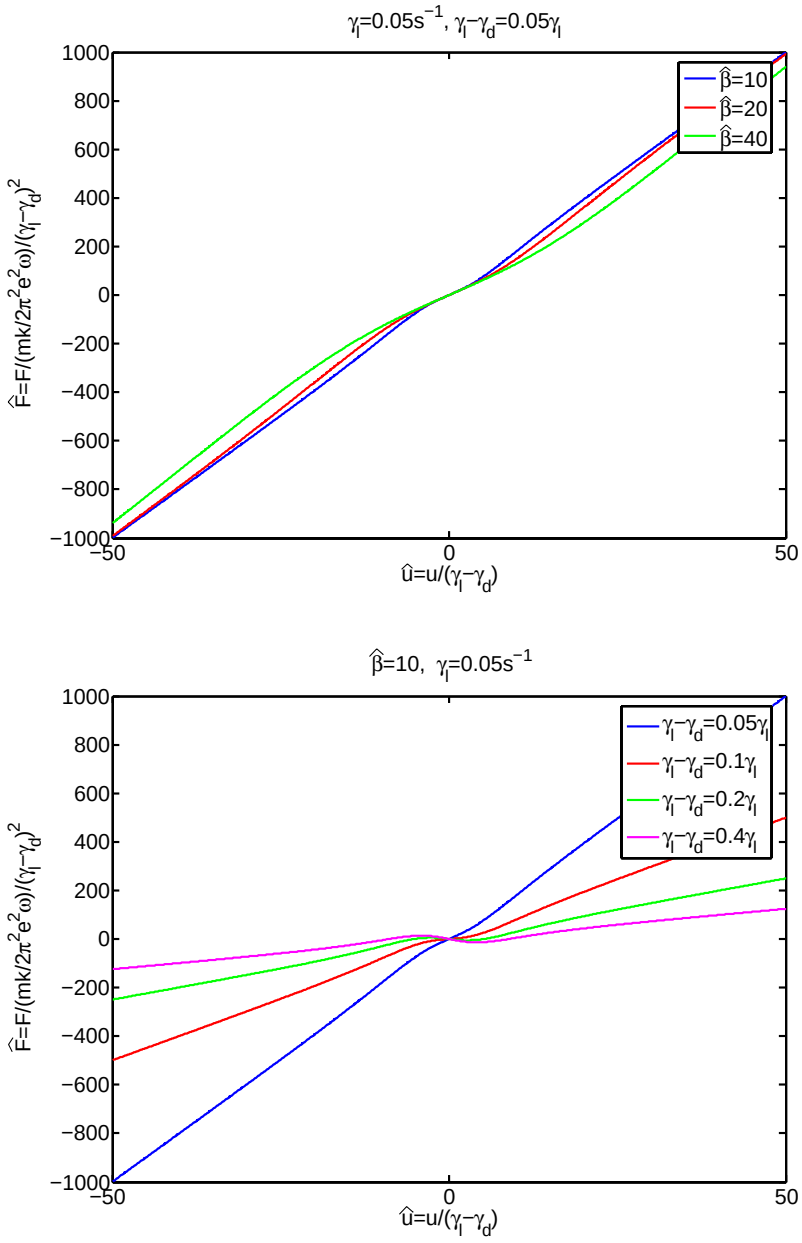

Figure 6.17: *Saturated distribution function for the pure Krook case*

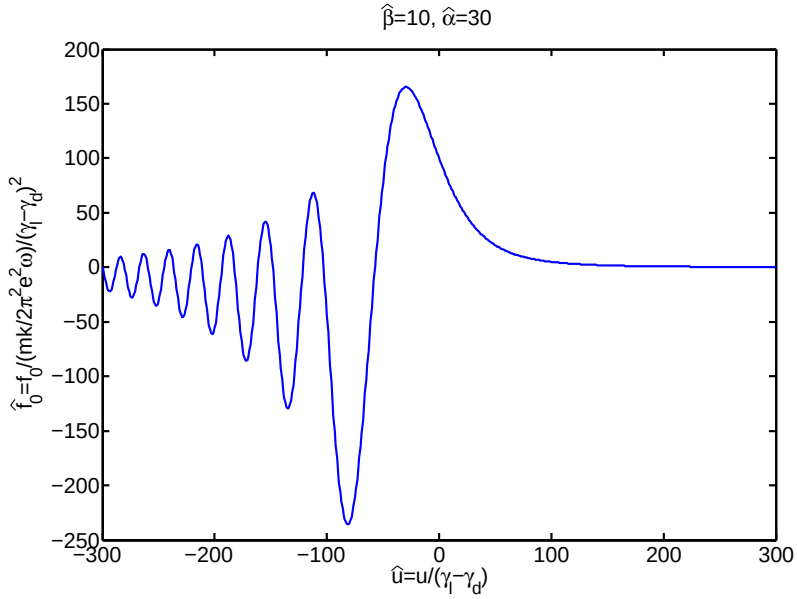

Figure 6.18: *f_0 for Krook and an artificially large amount of drag to illustrate the oscillatory behaviour of the drag.*

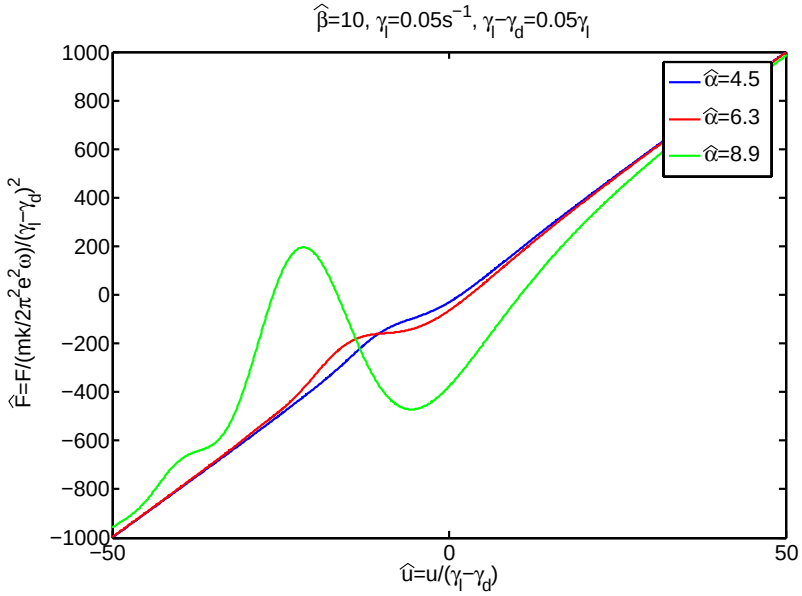

Figure 6.19: *Saturated distribution function for the Krook + drag case varying $\hat{\alpha} = 4.5, 6.3, 8.9$*

6.5 Generalisation to toroidal systems

Although the results obtained in section 6.4 were derived for a fast particle driven electrostatic wave in a 1-D velocity space, the theory can be generalised to fast particle driven instabilities in an arbitrary geometry [26]. This universality rests on the fact that the system is close to marginal stability, which still allows the linear properties of the mode to depend on the distribution of fast particles [26].

For the bump on tail case the competition between the wave electric field, distorting the distribution function, and the fast particle source, resorting the unstable distribution, gives rise to the interesting non-linear behaviour. For a general instability the effect of the wave is more complicated and to describe the 'competition' in the same framework as the bump on tail case, the correct projection in phase space must be taken. Specifically a transformation to a convenient set of canonical action-angle variables is necessary in order to 'flatten' the resonance surface locally, so that transport of particles across this surface can be reduced to the 1-D model outlined by the simple bump on tail case [26]. To illustrate this more clearly Fig 6.20 shows a reduced phase space of 3 dimensions and a resonance surface in that phase space. Transformation to the correct set of coordinates transforms this irregular surface into one which is flat and the motion of particles across this surface is then 1-D.

It can be shown that it is appropriate to express the periodic motion of objects in terms of conserved quantities or adiabatic invariants of the unperturbed motion [75]. For a toroidal system these conserved quantities are the energy E, and magnetic moment μ and the toroidal canonical momentum P_ϕ. For a low frequency perturbation such as the TAE, μ can be treated as constant and moreover, since the system is toroidally symmetric, $E - (\omega/n)\, P_\phi$ is conserved [76] and hence the wave predominantly affects P_ϕ and not the energy. From this one can infer that the correct projection, as descried above, is onto the P_ϕ direction. For the TAE the wave-particle resonance condition is $\Omega \equiv \omega - n \langle \omega_\phi \rangle - l \langle \omega_\theta \rangle = 0$, where $\omega \equiv \omega_{\mathrm{TAE}} \simeq v_A / (Rq(r))$, $\langle \omega_\phi \rangle \equiv \langle \partial\phi/\partial t \rangle$ and $\langle \omega_\theta \rangle \equiv \langle \partial\theta/\partial t \rangle$ are the orbit frequencies of energetic ions along toroidal, ϕ, and poloidal, θ coordinates, $\langle ... \rangle$ represents

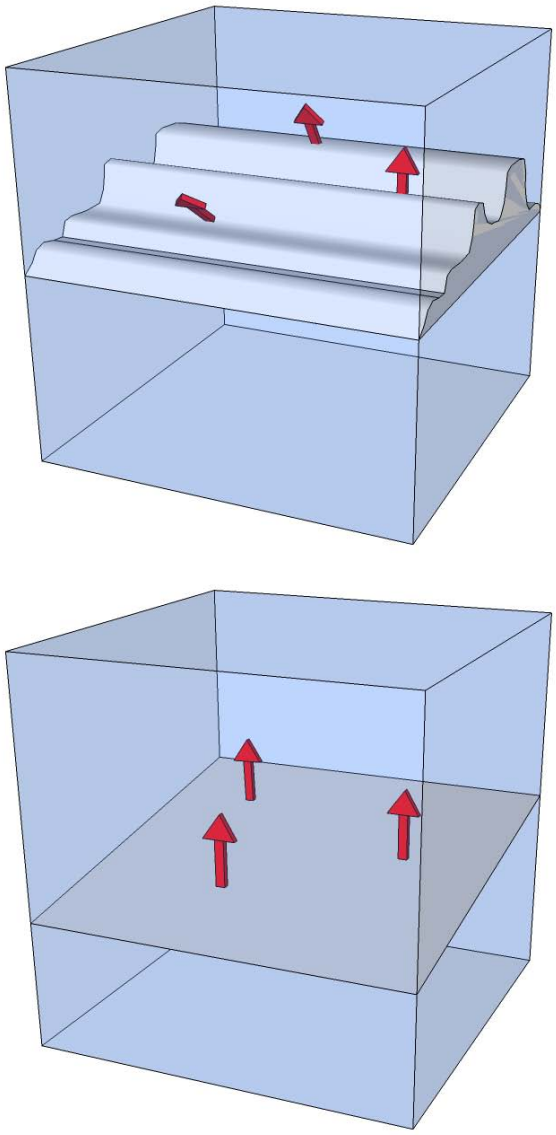

Figure 6.20: *Representation of the effect of the action-angle variable transformation on the resonance surface in a reduced 3-D phase space. The transformation takes the resonance surface in the top plot and produces the flat surface in the bottom plot.*

the orbit averaging, n is toroidal mode number of the TAE, and l is an integer value. For describing the fast particle motion across this resonance in phase space, due to the drag and diffusion, the Fokker-Planck operator is represented in the form

$$\left.\frac{dF}{dt}\right|_{coll} = \frac{\partial}{\partial \mathbf{v}} \cdot \mathbf{D} \cdot \frac{\partial f}{\partial \mathbf{v}} + \frac{\partial}{\partial \mathbf{v}} \cdot \mathbf{b} f = \left\langle \frac{\partial P_\phi}{\partial \mathbf{v}} \cdot \mathbf{D} \cdot \frac{\partial P_\phi}{\partial \mathbf{v}} \right\rangle \left(\frac{\partial \Omega}{\partial P_\phi} \right)^2 \frac{\partial^2 f}{\partial \Omega^2} + \left\langle \frac{\partial P_\phi}{\partial \mathbf{v}} \cdot \mathbf{b} \right\rangle \left(\frac{\partial \Omega}{\partial P_\phi} \right) \frac{\partial f}{\partial \Omega} \quad (6.34)$$

where derivatives $\partial\Omega/\partial P_\phi$ are taken at a constant value of $E-(\omega/n)\,P_\phi$. Considering TAEs driven by strongly passing beam ions with the resonance condition [42]

$$\Omega \equiv \omega - n\frac{v_\parallel}{R} - l\frac{v_\parallel}{Rq\,(r)} = 0 \tag{6.35}$$

where R is the major radius, r is the minor radius, q is the safety factor and $v_\parallel$ is the velocity parallel to the equilibrium magnetic field, one can estimate, from Eq 6.34 and 6.13b, the width of the resonance due to diffusion ($\Delta\Omega_{\rm Diff}$) and drag ($\Delta\Omega_{\rm Drag}$) similar to Δu_ν and Δu_α. The ratio of the two gives an estimate for which process dominates at the resonance

$$\frac{\left(\Delta\Omega_{\rm Diff}\right)^6}{\left(\Delta\Omega_{\rm Drag}\right)^6} \approx \left\langle \frac{\partial P_\phi}{\partial \mathbf{v}} \cdot \mathbf{D} \cdot \frac{\partial P_\phi}{\partial \mathbf{v}} \right\rangle^2 \left(\frac{\partial \Omega}{\partial P_\phi}\right) \left\langle \frac{\partial P_\phi}{\partial \mathbf{v}} \cdot \mathbf{b} \right\rangle^{-3} \tag{6.36}$$

and upon substituting the appropriate $\mathbf{D}$ and $\mathbf{b}$ [77], Eq 6.36 becomes (see appendix B)

$$\frac{\left(\Delta\Omega_{\rm Diff}\right)^6}{\left(\Delta\Omega_{\rm Drag}\right)^6} \approx mS\tau\frac{c}{eB_0}\frac{E_{\rm A}}{r^2}\frac{\theta_b^4}{2}\,\frac{27}{64}\left(\frac{\pi m_b}{m_e}\right)^{3/2}\left(\frac{T_e}{E_{\rm A}}\right)^{9/2} \tag{6.37}$$

where m is the poloidal mode number (of order unity), m_b is the mass of the beam species (deuterium in this case), $r \approx 50$cm is the minor radius, $B_0 \approx 5$kG, $T_e \approx 0.1-1$keV is the electron temperature, $E_{\rm A} \approx 10$keV is the resonant Alfvénic energy, $\theta_b \approx 0.6$rad, $S \approx 10^{-2}-10^{-1}$ is the magnetic shear, $\tau \equiv E_A^{3/2} m_b^{1/2}/\pi Z_b^2 e^4 n_e \ln\Lambda\sqrt{2} \approx 0.025s$. Using these parameters the collisional diffusion vs. drag is calculated to be $\Delta\Omega_{\rm Diff}/\Delta\Omega_{\rm Drag} \approx 0.2-1.6$, demonstrating that drag can dominate over the collisional diffusion in the vicinity of the TAE resonance.

From this one would expect that steady-state non-linear TAE behaviour is hardly possible for the case of NBI-produced slowing-down distribution functions, as is indeed observed in the bursting TAE experiments with NBI. In contrast, ICRH accelerated ions have a distribution function for which the dominant relaxation process is a quasi-linear diffusion due to the ICRH wave field. Here $\nu_{\rm eff}$ due to the wave exceeds the Coulomb collision frequency by an order of magnitude [23]. With such strong diffusion dominating over the drag, the marginally unstable TAEs are expected to exhibit the set of the four regimes [25], as is indeed the case [23, 24].

Finally, for nominal ITER parameters [55], the alpha particle excited TAEs are expected to be dominated by diffusion with $\Delta\Omega_{\rm Diff}/\Delta\Omega_{\rm Drag} \approx 1.4$ ($\theta_b \sim 1$). Since

drag is not negligibly small its effect should still be included in any predictive ITER calculations. The relevance of drag is further emphasised by noting the sensitivity of this estimate to the electron temperature, more specifically $\Delta\Omega_{\mathrm{Diff}}/\Delta\Omega_{\mathrm{Drag}}$ scales as $T_e^{3/4}$.

6.6 Discussion

The destabilising effect of dynamical friction, leading to an explosive behaviour, has been demonstrated in this chapter in the framework of the near-threshold non-linear theory. These results indicate that the non-linear evolution of, e.g., Alfvénic instabilities driven by super-Alfvénic neutral beam injection (NBI), or by fusion-born alpha-particles with drag-determined distribution functions should be more prone to the 'hard' regime than those driven by ion-cyclotron resonance heating (ICRH) with dominant RF quasi-linear diffusion. This has led to an interpretation of the experimentally observed differences between the steady-state, amplitude modulation and chaotic regimes of ICRH-driven TAE instabilities on the Join European Torus (JET) and the bursting frequency-chirping TAEs on MAST. A description of the mode evolution beyond the early explosive phase, i.e. in the strongly non-linear regime, with the addition of dynamical friction will be the subject of further study. The non-linear CAE behaviour, such as that seen in the recent MAST experiments, with both bursting and steady state behaviour, should also be fully interpreted. A first insight can be found by recalling that CAEs are driven by velocity space gradients such as temperature anisotropy. In this case pitch angle scattering (a diffusive process) is likely to play the dominant role.

Chapter 7

Conclusion

The final section summarises this thesis and enumerates the principle results and conclusions, indicating their significance. A summary of the author's understanding of the resonant interaction of fast particles with Alfvén waves in spherical tokamaks is given.

The existence of CAEs and ion-ion hybrid modes in a STPP: Chapter 2 described a relatively simple 1-D model, which successfully reproduced the key elements of STPP equilibria and allowed investigation of Alfvén eingemodes over a broad range of plasma parameters and $k_{\|}$ values. The model was able to identify compressional Alfvén eingemodes (CAEs) and ion-ion hybrid eingenmodes in a STPP with frequencies $\omega > \omega_{cD}$ and $\omega_{cT} < \omega < \omega_{cD}$ respectively. An assessment of the diagnostic capability of these modes for measuring the D-T ratio was performed and a positive outcome was obtained. This result may be used to diagnose the D-T concentration in next step burning plasma devices that cannot be accessed directly. The results motivated additional MAST experiments in order to assess the applicability of the 1-D model to current ST machines. These experiments were subsequently carried out by the author and the MAST team, and the results further validated the model. A principle extension to this work will include the poloidal nature of the magnetic field, which will link $k_{\|}$ and k_z explicitly.

The experimental validation of the Doppler resonance with counter propagating particles and waves with different polarisations: Chapter 3 presented a description of the fundamental physics issues for resonant wave-particle interactions and described experimental studies of some key points relevant for this thesis on the LAPD device. The key points investigated were the efficiency of the Dopper resonance for counter propagating Alfvén waves and fast particles, relevant for explaining high frequency modes observed on MAST, and the importance of the wave polarisation in the interaction. As a result of the LAPD experiments, the counter propagating waves and particles (also seen on MAST) satisfying the Doppler resonance condition were indeed found to interact efficiently. Further study of wave particle resonance in LAPD, e.g. the study of anomalous Doppler effect for super-Alfvénic probe ions, does require an additional modification of the LAPD set-up, and may be performed in future experiments.

Experimental and theoretical studies of CAEs on MAST: Chapter 4 described the experimental scenario, developed by the author and the MAST team, for the study of CAEs driven by NBI. The Doppler shifted cyclotron resonance was shown to be the appropriate resonance for these modes, and the inaccessibility of the anomalous resonance has been suggested as an explanation for the lack of observed $n_{\text{exp}} > 0$ modes. The results have motivated additional MAST experiments to achieve sufficient conditions for $n_{\text{exp}} > 0$ to be observed. The continual investigation of CAEs is also of interest due to their potential effect on the efficiency of beam driven current in tokamaks, necessary for steady state operation.

Determination of the free energy sources driving CAEs: Chapter 5 performed an analytical study of a typical NBI distribution function with the aim of identifying the free energy sources driving CAEs. By combining the experimentally observed frequency and toroidal mode numbers, together with the Doppler resonance condition, the linear drive for CAEs was calculated using the 1-D model. Temperature anisotropy and 'bump-on-tail' have been identified as the appropriate free energy sources for CAEs. Further investigation is required with improved TRANSP runs and with finite Larmor radius effects taken into account.

The destabilising effect of dynamical friction: Chapter 6 was motivated by

the non-linear behaviour of beam driven CAEs observed on MAST. Dynamical friction (drag) was included into an existing theory of marginally unstable modes, the result of which was profoundly different to the previously studied Krook and velocity space diffusion cases. When drag is the dominant collisional process, only an explosive wave evolution is obtained, in contrast to the previous cases where four non-linear regimes are possible. It was subsequently shown that, in MAST experiments, drag can indeed dominate over velocity space diffusion in the vicinity of the wave particle resonance for NBI driven TAEs. This is in contrast to ICRH driven TAEs on JET where RF wave diffusion is dominant. Interpretation of these experimental differences has now been given in this thesis in the context of this extended marginal stability theory. The implication for the non-linear evolution of fast particle driven instabilities in burning plasmas, such as a STPP and ITER, is that alpha particles could quite possibly cause explosive, bursting TAE events, which have so far not been considered. This in itself will require further study, including the effect of full non-linearity, however further study of CAEs in the context of this theory should also be performed to create a more complete picture of fast particle driven instabilities.

It is clear, from the content of this thesis, that spherical tokamaks are not only significant in their own right but have an important role to play when considering the effects of fast particles in burning plasmas in general. The ability of the MAST spherical tokamak to operate in regimes with super Alfvénic fast ions has enabled access to physics similar to a burning plasma environment. As such it has and continues to stimulate research into the area of fast particle driven instabilities that are likely to play a significant role in future devices with super Alfvénic fusion born alpha particles.

Appendix A

Anomalous Doppler resonance

A.1 Parallel propagating CAWs

The anomalous Doppler resonance can be represented by

$$\omega = k_{\|} v_{\|} - \omega_{cb}, \qquad \frac{\partial \omega}{\partial k_{\|}} = v_{\|} = \frac{\omega + \omega_{cb}}{k_{\|}} \tag{A.1}$$

where ω_{cb} is the cyclotron frequency of the injected beam ions. The dispersion relation for parallel propagating CAWs is given by

$$N_{\|}^2 = 1 + \frac{\omega_{pi}^2}{\omega_{ci}\left(\omega + \omega_{ci}\right)}, \qquad \frac{\partial \omega}{\partial k_{\|}} = \frac{\dfrac{2}{k_{\|}}\left[1 + \dfrac{\omega_{pi}^2}{\omega_{ci}\left(\omega + \omega_{ci}\right)}\right]}{\dfrac{2}{\omega}\left[1 + \dfrac{\omega_{pi}^2}{\omega_{ci}\left(\omega + \omega_{ci}\right)}\right] - \dfrac{\omega_{pi}^2}{\omega_{ci}\left(\omega + \omega_{ci}\right)^2}} \tag{A.2}$$

The intersection between the curves in Eq A.1 and Eq A.2 gives a resonance between CAWs and fast particles via the anomalous Doppler resonance. From Fig A.1 It can be seen that below a critical $v_{\|}$ the two lines do not intersect and no resonance is possible.

This is due to the finite frequency correction of the CAW dispersion relation. This critical velocity can be determined by insisting that the resonance line is a tangent to the CAW dispersion curve. A necessary condition for this is represented by the gradient matching condition

$$\frac{2\left[1 + \dfrac{\omega_{pi}^2}{\omega_{ci}\left(\omega + \omega_{ci}\right)}\right]}{\dfrac{2}{\omega}\left[1 + \dfrac{\omega_{pi}^2}{\omega_{ci}\left(\omega + \omega_{ci}\right)}\right] - \dfrac{\omega_{pi}^2}{\omega_{ci}\left(\omega + \omega_{ci}\right)^2}} = \omega + \omega_{cb} \tag{A.3}$$

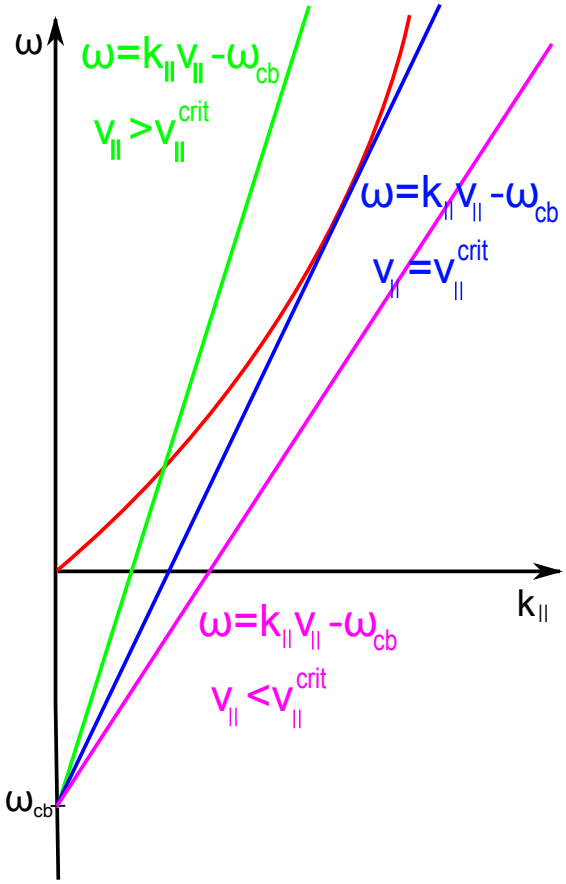

Figure A.1: *Red lines shows the CAE dispersion relation, coloured lines show the resonance line for different velocities.*

which leads to the following quadratic

$$x^2\left[2\omega_{ci}\omega_{cb}-\omega_{pi}^2\right]+x\left[2\omega_{cb}\omega_{pi}^2+\omega_{pi}^2\left(\Delta\omega+\omega_{ci}\right)\right]-\omega_{pi}^2\omega_{ci}\Delta\omega=0, \tag{A.4}$$

where $x=\omega+\omega_{ci}$ and $\Delta\omega=\omega_{ci}-\omega_{cb}$. For the case when $\omega_{ci}\approx\omega_{cb}$ the solution for ω is approximately

$$\omega\approx\frac{2\omega_{cb}\omega_{ci}^2+2\omega_{pi}^2\omega_{cb}}{\omega_{pi}^2-2\omega_{ci}\omega_{cb}} \tag{A.5}$$

with equality when $\omega_{ci}=\omega_{cb}$. By noting that $\omega_{pi}^2/\omega_{ci}^2=c^2/v_{\mathrm{A}}^2$, and by assuming that $c^2/v_{\mathrm{A}}^2\gg1$, the parallel wave vector $k_{\|}$ can be approximated by

$$k_{\|}=\frac{\omega}{c}\left(1+\frac{\omega_{pi}^2}{\omega_{ci}\left(\omega+\omega_{ci}\right)}\right)^{\frac{1}{2}}\approx\frac{\omega}{c}\left(\frac{\omega_{pi}^2}{\omega_{ci}\left(\omega+\omega_{ci}\right)}\right)^{\frac{1}{2}}. \tag{A.6}$$

By substituting Eqs A.5 and A.6 into Eq A.1 the tangent condition is ensured. The

critical velocity is then found to be

$$v_{\parallel} = \frac{\dfrac{2\omega_{cb}\omega_{ci}^2 + 2\omega_{pi}^2\omega_{cb}}{\omega_{pi}^2 - 2\omega_{ci}\omega_{cb}} + \omega_{cb}}{\dfrac{1}{c}\dfrac{2\omega_{cb}\omega_{ci}^2 + 2\omega_{pi}^2\omega_{cb}}{\omega_{pi}^2 - 2\omega_{ci}\omega_{cb}}\left(\dfrac{\omega_{pi}^2}{\omega_{ci}\left(\dfrac{2\omega_{cb}\omega_{ci}^2 + 2\omega_{pi}^2\omega_{cb}}{\omega_{pi}^2 - 2\omega_{ci}\omega_{cb}} + \omega_{ci}\right)}\right)^{\frac{1}{2}}} \tag{A.7}$$

$$\Rightarrow v_{\parallel} = \frac{c\left[1 + \dfrac{\omega_{pi}^2 - 2\omega_{ci}\omega_{cb}}{2\left(\omega_{ci}^2 + \omega_{pi}^2\right)}\right]}{\dfrac{\omega_{pi}}{\omega_{ci}}\left(\dfrac{1}{\left(\dfrac{2\dfrac{\omega_{cb}}{\omega_{ci}}\left(\omega_{ci}^2 + \omega_{pi}^2\right)}{\omega_{pi}^2 - 2\omega_{ci}\omega_{cb}} + 1\right)}\right)^{\frac{1}{2}}} \tag{A.8}$$

$$v_{\parallel} = v_{\mathrm{A}}\left[1 + \frac{\omega_{pi}^2 - 2\omega_{ci}\omega_{cb}}{2\left(\omega_{ci}^2 + \omega_{pi}^2\right)}\right]\left[1 + \frac{2\dfrac{\omega_{cb}}{\omega_{ci}}\left(\omega_{ci}^2 + \omega_{pi}^2\right)}{\omega_{pi}^2 - 2\omega_{ci}\omega_{cb}}\right]^{\frac{1}{2}} \tag{A.9}$$

By again using $c^2/v_{\mathrm{A}}^2 \gg 1$ the critical velocity can be reduced to

$$\frac{v_{\parallel}^{\mathrm{crit}}}{v_{\mathrm{A}}} = \frac{3}{2}\sqrt{1 + \frac{2\omega_{cb}}{\omega_{ci}}} \tag{A.10}$$

which, in the case that the beam and background species are identical, reduces to $v_{\parallel}^{\mathrm{crit}}/v_{\mathrm{A}} \approx 2.6$.

A.2 Arbitrary propagation of CAWs

For an arbitrary propagation angle, the low frequency CAW dispersion relation is taken

$$\omega = kv_{\mathrm{A}}, \qquad \frac{\partial\omega}{\partial k_{\parallel}} = v_{\mathrm{A}}\frac{\partial k}{\partial k_{\parallel}} \qquad \text{with} \qquad k_{\perp} = a - bk_{\parallel} \tag{A.11}$$

where $a = nq/r$ and $b = Rq/r$. The choice of $k_{\perp}$ is based on Eq 4.1, with $k_{\theta} = k_{\perp}$. The same procedure outlined in section A is followed here. The gradient matching

condition is

$$\frac{\left[k_\parallel - b\left(a - bk_\parallel\right)\right] v_\mathrm{A}}{\left[k_\parallel^2 + \left(a - bk_\parallel\right)^2\right]^{\frac{1}{2}}} = \frac{\left[k_\parallel^2 + \left(a - bk_\parallel\right)^2\right]^{\frac{1}{2}} v_\mathrm{A} + \omega_{cb}}{k_\parallel} \tag{A.12}$$

which reduces to the following equation that must be solved for $k_\parallel$

$$\omega_{cb}\left[k_\parallel^2 + \left(a - bk_\parallel\right)^2\right]^{\frac{1}{2}} = -\left[k_\parallel^2 + \left(a - bk_\parallel\right)^2\right] v_\mathrm{A} + \left[k_\parallel - b\left(a - bk_\parallel\right)\right] k_\parallel v_\mathrm{A}. \tag{A.13}$$

Recalling that $k_\perp = a - bk_\parallel$ the equation can be rewritten as

$$\omega_{cb} k = a v_\mathrm{A} \left|k_\perp\right| \tag{A.14}$$

which, upon solving for $k_\perp$ (and hence $k_\parallel$), gives

$$k_\parallel = \frac{a}{b} - \frac{\frac{a}{b^3}\omega_{cb}^2 \mp \frac{\omega_{cb} a}{b^2}\sqrt{a^2 v_\mathrm{A}^2 - \omega_{cb}^2}}{\left[\omega_{cb}^2 + \frac{\omega_{cb}^2}{b^2} - a^2 v_\mathrm{A}^2\right]}. \tag{A.15}$$

and hence

$$k_\parallel = \frac{a\left[\omega_{cb}^2 - a^2 v_\mathrm{A}^2\right] \pm \frac{\omega_{cb} a}{b}\sqrt{a^2 v_\mathrm{A}^2 - \omega_{cb}^2}}{b\left[\omega_{cb}^2 + \frac{\omega_{cb}^2}{b^2} - a^2 v_\mathrm{A}^2\right]} \tag{A.16}$$

Using Eq A.14 the critical velocity can then be written as

$$v_\parallel = \frac{\omega + \omega_{cb}}{k_\parallel} = \frac{k v_\mathrm{A} + \omega_{cb}}{k_\parallel} = \frac{\frac{a v_\mathrm{A}}{\omega_{cb}}\left|k_\perp\right| v_\mathrm{A} + \omega_{cb}}{k_\parallel} = \frac{\frac{a v_\mathrm{A}}{\omega_{cb}}\left|a - bk_\parallel\right| v_\mathrm{A} + \omega_{cb}}{k_\parallel}. \tag{A.17}$$

Using Eq A.16

$$v_\parallel = \frac{\frac{a v_\mathrm{A}^2}{\omega_{cb}}\left|a - \frac{a\left[\omega_{cb}^2 - a^2 v_\mathrm{A}^2\right] \pm \frac{\omega_{cb} a}{b}\sqrt{a^2 v_\mathrm{A}^2 - \omega_{cb}^2}}{\left[\omega_{cb}^2 + \frac{\omega_{cb}^2}{b^2} - a^2 v_\mathrm{A}^2\right]}\right| + \omega_{cb}}{\frac{a\left[\omega_{cb}^2 - a^2 v_\mathrm{A}^2\right] \pm \frac{\omega_{cb} a}{b}\sqrt{a^2 v_\mathrm{A}^2 - \omega_{cb}^2}}{b\left[\omega_{cb}^2 + \frac{\omega_{cb}^2}{b^2} - a^2 v_\mathrm{A}^2\right]}} \tag{A.18}$$

and assuming $a > 0$ then

$$v_\parallel = \frac{\frac{a v_\mathrm{A}^2}{\omega_{cb}}\left|1 - \frac{\left[\omega_{cb}^2 - a^2 v_\mathrm{A}^2\right] \pm \frac{\omega_{cb}}{b}\sqrt{a^2 v_\mathrm{A}^2 - \omega_{cb}^2}}{\left[\omega_{cb}^2 + \frac{\omega_{cb}^2}{b^2} - a^2 v_\mathrm{A}^2\right]}\right| + \frac{\omega_{cb}}{a}}{\frac{\left[\omega_{cb}^2 - a^2 v_\mathrm{A}^2\right] \pm \frac{\omega_{cb}}{b}\sqrt{a^2 v_\mathrm{A}^2 - \omega_{cb}^2}}{b\left[\omega_{cb}^2 + \frac{\omega_{cb}^2}{b^2} - a^2 v_\mathrm{A}^2\right]}} \tag{A.19}$$

By neglecting term of order $\omega_{cb}^2/a^2v_{\rm A}^2$ then

$$v_\parallel = \frac{v_{\rm A} + \dfrac{b\omega_{cb}}{a}}{1 \mp \dfrac{\omega_{cb}}{abv_{\rm A}}} \tag{A.20}$$

which leads to

$$v_\parallel = v_{\rm A}\left[1 + \frac{b\omega_{cb}}{v_{\rm A}a} \pm \frac{\omega_{cb}}{v_{\rm A}ab}\right] \tag{A.21}$$

the assumption that $a > 0$ implies that the toroidal mode number $n > 0$, which implies $k_\parallel > 0$. In this case the bottom sign in Eq A.16 should be taken. This reduces the critical velocity to

$$v_\parallel^{\rm crit} = v_{\rm A}\left[1 + \frac{\omega_{cb}}{v_{\rm A}a}\left(\frac{b^2-1}{b}\right)\right]. \tag{A.22}$$

The assumption that $\omega_{cb} < av_{\rm A}$ may not always be satisfied, and in the case of MAST this condition can be violated. By observing that as $k_\parallel \to \infty$ $k_\perp \to -bk_\parallel$ and so the dispersion becomes a straight line

$$\omega \approx k_\parallel v_{\rm A}\sqrt{1+b^2} - \frac{ab}{\sqrt{1+b^2}}v_{\rm A}, \tag{A.23}$$

one can infer that if $\omega_{cb} > abv_{\rm A}/\sqrt{1+b^2}$ the dispersion curve can only be intersected by the resonance line if

$$v_\parallel > v_\parallel^{\rm crit} = v_{\rm A}\sqrt{1+b^2}. \tag{A.24}$$

This approximation does not neglect terms of order $\omega_{cb}^2/a^2v_{\rm A}^2$, but does assume that ω_{cb} is large enough so that the intersection occurs in the large $k_\parallel$ region, which for the case of MAST is well satisfied.

Appendix B

Marginal stability

Since f_1 appears in the wave equation, the following equation

$$\frac{\partial f_1}{\partial t} + iuf_1 - \nu^3 \frac{\partial^2 f_1}{\partial u^2} - \alpha^2 \frac{\partial f_1}{\partial u} + \beta f_1 = -\frac{ek}{2m}\hat{E}\frac{\partial}{\partial u}\left(F_0 + f_0 + f_2\right) \tag{B.1}$$

is solved iteratively for a solution of the form $f_1 = f_1^1 + f_1^3$, where f_1^1 is the linear contribution and f_1^3 is the first (cubic) non-linear contribution.

B.1 Linear contribution

Since F_0 is the largest term ($F_0 \gg f_1 \gg f_0, f_2$), Eq B.1 is solved by first taking the terms that are linear in the wave amplitude, i.e

$$\frac{\partial f_1^1}{\partial t} + iuf_1^1 - \nu^3 \frac{\partial^2 f_1^1}{\partial u^2} - \alpha^2 \frac{\partial f_1^1}{\partial u} + \beta f_1^1 = -\frac{ek}{2m}\hat{E}\frac{\partial F_0}{\partial u}. \tag{B.2}$$

Fourier transforming Eq B.2 (assuming that $\partial F_0/\partial u$ is constant) gives

$$\frac{\partial \mathscr{F}_1^1}{\partial t} + \frac{i}{-2\pi i}\frac{\partial \mathscr{F}_1^1}{\partial p} + 4\pi^2 p^2 \nu^3 \mathscr{F}_1^1 - 2\pi i p \alpha^2 \mathscr{F}_1^1 + \beta \mathscr{F}_1^1 = -\frac{ek}{2m}\hat{E}\frac{\partial F_0}{\partial u}\delta\left(p\right). \tag{B.3}$$

The following variables are defined

$$\begin{aligned} t' &= t \\ p_0 &= 2\pi p + t \end{aligned} \tag{B.4}$$

so that

$$\frac{\partial \mathscr{F}_1^1}{\partial t} + \mathscr{F}_1^1\left[\nu^3\left(p_0 - t\right)^2 - i\alpha^2\left(p_0 - t\right) + \beta\right] = -\frac{ek}{2m}\hat{E}\frac{\partial F_0}{\partial u}2\pi\delta\left(p_0 - t\right) \tag{B.5}$$

where t has been used for notational convenience and will be used from now on. Solving using an integrating factor method gives

$$\mathscr{F}_1^1(p_0,t) = e^{\frac{\nu^3}{3}(p_0-t)^3-\frac{i\alpha^2}{2}(p_0-t)^2-\beta t}\int_0^t -\frac{ek}{2m}\hat{E}(t')\frac{\partial F_0}{\partial u}2\pi\delta(p_0-t')\times e^{-\frac{\nu^3}{3}(p_0-t')^3+\frac{i\alpha^2}{2}(p_0-t')^2+\beta t'}dt' \quad \text{(B.6)}$$

and transforming back into the original Fourier variables gives

$$\mathscr{F}_1^1(p,t) = e^{\frac{\nu^3}{3}8\pi^3p^3-\frac{i\alpha^2}{2}4\pi^2p^2-\beta t}\int_0^t -\frac{ek}{2m}\hat{E}(t')\frac{\partial F_0}{\partial u}2\pi\delta(2\pi p+t-t')\times e^{-\frac{\nu^3}{3}(2\pi p+t-t')^3+\frac{i\alpha^2}{2}(2\pi p+t-t')^2+\beta t'}dt'. \quad \text{(B.7)}$$

The wave equation requires $\int_{-\infty}^{\infty} f_1 du$. Using the Fourier representation this integration is simplified to

$$\int_{-\infty}^{\infty} f_1 du = \int_{-\infty}^{\infty}\int_{-\infty}^{\infty} e^{-2\pi ipu}\mathscr{F}_1 dp du = \int_{-\infty}^{\infty}\delta(p)\mathscr{F}_1 dp = \mathscr{F}_1(p=0). \quad \text{(B.8)}$$

From this, Eq B.7 and Eq 6.12 then lead to the following wave equation

$$\frac{\partial\omega_B^2}{\partial t} = (\gamma_l-\gamma_d)\omega_B^2 \quad \text{(B.9)}$$

where $\gamma_l = 2\pi^2(e^2\omega/mk^2)\partial F_0(\omega/k)/\partial v$ is the linear growth rate and $\omega_B^2 = ek\hat{E}/m$ is the non-linear bounce frequency.

B.2 f_0 non-linear contribution

The first non-linear correction to f_1 arising from the f_0 part is found by solving the following equation

$$\frac{\partial f_1^3}{\partial t} + iuf_1^3 - \nu^3\frac{\partial^2 f_1^3}{\partial u^2} - \alpha^2\frac{\partial f_1^3}{\partial u} + \beta f_1^3 = -\frac{ek}{2m}\hat{E}\frac{\partial f_0}{\partial u}. \quad \text{(B.10)}$$

Fourier transforming and using the variables in Eq B.4 gives

$$\frac{\partial\mathscr{F}_1^3}{\partial t} + \mathscr{F}_1^3\left[\nu^3(p_0-t)^2 - i\alpha^2(p_0-t)+\beta\right] = -\frac{ek}{2m}\hat{E}i(p_0-t)\mathscr{F}_0 \quad \text{(B.11)}$$

the solution of which is given by

$$\mathscr{F}_1^3(p_0,t) = e^{\frac{\nu^3}{3}(p_0-t)^3-\frac{i\alpha^2}{2}(p_0-t)^2-\beta t}\int_0^t -\frac{ek}{2m}\hat{E}(t')\,i(p_0-t')\times e^{-\frac{\nu^3}{3}(p_0-t')^3+\frac{i\alpha^2}{2}(p_0-t')^2+\beta t'}\mathscr{F}_0(p_0,t')\,dt' \quad \text{(B.12)}$$

which in standard Fourier variables is represented by

$$\mathscr{F}_1^3(p,t) = e^{\frac{\nu^3}{3}8\pi^3p^3-\frac{i\alpha^2}{2}4\pi^2p^2-\beta t}\int_0^t -\frac{ek}{2m}\hat{E}(t')\,i(2\pi p+t-t')\times e^{-\frac{\nu^3}{3}(2\pi p+t-t')^3+\frac{i\alpha^2}{2}(2\pi p+t-t')^2+\beta t'}\mathscr{F}_0(t')\,dt'. \quad \text{(B.13)}$$

The non-linear correction to f_1 requires f_0, which is determined by the equation below

$$\frac{\partial f_0}{\partial t}-\nu^3\frac{\partial^2 f_0}{\partial u^2}-\alpha^2\frac{\partial f_0}{\partial u}+\beta f_0 = -\frac{ek}{2m}\left(\hat{E}\frac{\partial f_1^{1*}}{\partial u}+\text{c.c}\right). \quad \text{(B.14)}$$

Fourier transforming this equation gives

$$\frac{\partial\mathscr{F}_0}{\partial t}+\mathscr{F}_0\left(4\pi^2\nu^3p^2-2\pi i\alpha^2p+\beta\right) = -\frac{ek}{2m}2\pi ip\left(\hat{E}\mathscr{F}_1^{1*}(-p)+\hat{E}^*\mathscr{F}_1^1(p)\right) \quad \text{(B.15)}$$

the solution of which is given by

$$\mathscr{F}_0 = e^{-4\pi^2\nu^3p^2t+2\pi i\alpha^2pt-\beta t}2\pi ip\int_0^t -\frac{ek}{2m}e^{4\pi^2\nu^3p^2t'-2\pi i\alpha^2pt'+\beta t'}\left[\hat{E}(t')\,\mathscr{F}_1^{1*}(-p,t')+\hat{E}^*(t')\,\mathscr{F}_1^1(p,t')\right]dt'. \quad \text{(B.16)}$$

When $\mathscr{F}_1^1$ is substituted the result becomes

$$\mathscr{F}_0 = e^{-4\pi^2\nu^3p^2t+2\pi i\alpha^2pt-\beta t}2\pi ip\int_0^t -\frac{ek}{2m}\hat{E}(t')\frac{\partial F_0}{\partial u}e^{4\pi^2\nu^3p^2t'-2\pi i\alpha^2pt'}e^{-\frac{\nu^3}{3}8\pi^3p^3+\frac{i\alpha^2}{2}4\pi^2p^2}\times$$
$$\int_0^{t'} -\frac{ek}{2m}\hat{E}^*(t'')\,2\pi\delta(-2\pi p+t'-t'')\,e^{-\frac{\nu^3}{3}(-2\pi p+t'-t'')^3-\frac{i\alpha^2}{2}(-2\pi p+t'-t'')^2+\beta t''}dt''dt'+$$
$$e^{-4\pi^2\nu^3p^2t+2\pi i\alpha^2pt-\beta t}2\pi ip\int_0^t -\frac{ek}{2m}\hat{E}(t')\frac{\partial F_0}{\partial u}e^{+4\pi^2\nu^3p^2t'-2\pi i\alpha^2pt'}e^{\frac{\nu^3}{3}8\pi^3p^3-\frac{i\alpha^2}{2}4\pi^2p^2}\times$$
$$\int_0^{t'} -\frac{ek}{2m}\hat{E}^*(t'')\,2\pi\delta(2\pi p+t'-t'')\,e^{-\frac{\nu^3}{3}(2\pi p+t'-t'')^3+\frac{i\alpha^2}{2}(2\pi p+t'-t'')^2+\beta t''}dt''dt'. \quad \text{(B.17)}$$

This $\mathscr{F}_0$ must be substituted into Eq B.12 with $p = (p_0 - t')/2\pi$. Recalling that $\mathscr{F}_1^3(p=0)$ gives the required velocity integral for the wave equation, then substituting $p = (t-t')/2\pi$ into Eq B.17 and substituting this result into Eq B.13 with $p = 0$ gives the required non-linear contribution to the wave equation

$$\mathscr{F}_1^3(p=0) = -e^{-\beta t}\frac{\partial F_0}{\partial u}\int_0^t -\frac{ek}{2m}\hat{E}(t')(t-t')^2 e^{-\frac{\nu^3}{3}(t-t')^3+\frac{i\alpha^2}{2}(t-t')^2} e^{-\nu^3(t-t')^2t'+i\alpha^2(t-t')t'}\times$$
$$\int_0^{t'} -\frac{ek}{2m}\hat{E}(t'')\, e^{\nu^3(t-t')^2t''-i\alpha^2(t-t')t''} e^{-\frac{\nu^3}{3}(t-t')^3+\frac{i\alpha^2}{2}(t-t')^2}\times$$
$$\int_0^{t''} -\frac{ek}{2m}\hat{E}^*(t''')\, 2\pi\delta(-t+t'+t''-t''')\, e^{-\frac{\nu^3}{3}(-t+t'+t''-t''')^3-\frac{i\alpha^2}{2}(-t+t'+t''-t''')^2+\beta t'''} dt'''dt''dt'$$
$$-e^{-\beta t}\frac{\partial F_0}{\partial u}\int_0^t -\frac{ek}{2m}\hat{E}(t')(t-t')^2 e^{-\frac{\nu^3}{3}(t-t')^3+\frac{i\alpha^2}{2}(t-t')^2} e^{-\nu^3(t-t')^2t'+i\alpha^2(t-t')t'}\times$$
$$\int_0^{t'} -\frac{ek}{2m}\hat{E}(t'')\, e^{\nu^3(t-t')^2t''-i\alpha^2(t-t')t''} e^{\frac{\nu^3}{3}(t-t')^3-\frac{i\alpha^2}{2}(t-t')^2}\times$$
$$\int_0^{t''} -\frac{ek}{2m}\hat{E}^*(t''')\, 2\pi\delta(t-t'+t''-t''') e^{-\frac{\nu^3}{3}(t-t'+t''-t''')^3+\frac{i\alpha^2}{2}(t-t'+t''-t''')^2+\beta t'''} dt'''dt''dt'. \tag{B.18}$$

Since $t > t'$, the t''' integral is identically zero for the second term. The first term only contributes when $t' > t/2$ and $t'' > t - t'$, leaving only

$$\mathscr{F}_1^3(p=0) = -e^{-\beta t}\frac{\partial F_0}{\partial u}\int_{t/2}^t -\frac{ek}{2m}\hat{E}(t')(t-t')^2 e^{-\frac{\nu^3}{3}(t-t')^3+\frac{i\alpha^2}{2}(t-t')^2} e^{-\nu^3(t-t')^2t'+i\alpha^2(t-t')t'}\times$$
$$\int_{t-t'}^{t'} -\frac{ek}{2m}\hat{E}(t'')\, e^{\nu^3(t-t')^2t''-i\alpha^2(t-t')t''} e^{-\frac{\nu^3}{3}(t-t')^3+\frac{i\alpha^2}{2}(t-t')^2}(-)\frac{ek}{2m}\hat{E}^*(-t+t'+t'')$$
$$2\pi e^{\beta(-t+t'+t'')} dt''dt'. \tag{B.19}$$

This can be reduced further to

$$\mathscr{F}_1^3(p=0) = 2\pi\frac{\partial F_0}{\partial u}\int_{t/2}^{t}\frac{ek}{2m}\hat{E}(t')(t-t')^2\int_{t-t'}^{t'}\frac{ek}{2m}\hat{E}(t'')\,e^{\nu^3(t-t')^2(t''-t')-i\alpha^2(t-t')(t''-t')}\times$$
$$e^{-\frac{2}{3}\nu^3(t-t')^3+i\alpha^2(t-t')^2}\frac{ek}{2m}\hat{E}^*(-t+t'+t'')\,e^{\beta(-2t+t'+t'')}dt''dt'. \quad \text{(B.20)}$$

By changing variables to $z = t - t'$ and $x = t - z - t''$ the non-linear contribution becomes

$$\mathscr{F}_1^3(p=0) = 2\pi\frac{\partial F_0}{\partial u}\int_{0}^{t/2}\frac{ek}{2m}\hat{E}(t-z)\,z^2\int_{0}^{t-2z}\frac{ek}{2m}\hat{E}(t-z-x)\frac{ek}{2m}\hat{E}^*(t-z-2x)\times$$
$$e^{-\nu^3z^2(2z/3+x)+i\alpha^2z(z+x)-\beta(2z+x)}dxdz. \quad \text{(B.21)}$$

When this is substituted into the wave equation, including the linear terms, we have the following

$$\frac{\partial\omega_B^2}{\partial t} = (\gamma_l-\gamma_d)\,\omega_B^2 - \frac{\gamma_l}{2}\int_{0}^{t/2}z^2\omega_B^2(t-z)\int_{0}^{t-2z}e^{-\nu^3z^2(2z/3+x)+i\alpha^2z(z+x)-\beta(2z+x)}\times$$
$$\omega_B^2(t-z-x)\,\omega_B^{2*}(t-z-2x)\,dxdz. \quad \text{(B.22)}$$

This is in fact the complete non-linear equation up to cubic non-linearity. The contribution from f_2 is identically zero, which can be seen in the following section.

B.3 f_2 non-linear contribution

The f_2 non-linear contribution to the wave equation is identically zero up to cubic order in the wave amplitude as can be seen from the f_2 equation below

$$\frac{\partial f_2}{\partial t} + 2iuf_2 - \nu^3\frac{\partial^2 f_2}{\partial u^2} - \alpha^2\frac{\partial f_2}{\partial u} + \beta f_2 = -\frac{ek}{2m}\hat{E}^*\frac{\partial f_1^1}{\partial u}. \quad \text{(B.23)}$$

The contribution from the f_1^1 term is identical to the second term in Eq B.14. Recall that this term did not contribute to the t''' integral in Eq B.18. Hence the f_2 contribution is also identically zero.

B.4 Drag and diffusion stability

For the case of diffusive + drag the amplitude evolution equation is

$$\frac{dA}{d\tau} = A(\tau) - \frac{1}{2}\int_0^{\tau/2} dz\, z^2 A(\tau - z) \int_0^{\tau-2z} dx\, e^{-\hat{\nu}^3 z^2(2z/3+x)+i\hat{\alpha}z(z+x)} A(\tau - z - x) A^*(\tau - 2z - x) \quad \text{(B.24)}$$

Let $A = A_0(1 + \delta A)$, where $A_0 = |A_0|\exp(ib\tau)$. For long times $\tau \to \infty$, Eq B.24 becomes

$$\frac{d(\delta A A_0)}{d\tau} + ibA_0 = A_0 + \delta A A_0 - \frac{1}{2}\int_0^{\infty} dz\, z^2 (A_0(\tau - z) + \delta A(\tau - z) A_0(\tau - z)) \times \int_0^{\infty} dx\, e^{-\hat{\nu}^3 z^2(2z/3+x)+i\hat{\alpha}z(z+x)} (A_0(\tau - z - x) + \delta A(\tau - z - x) A_0(\tau - z - x)) (A_0^*(\tau - 2z - x) + \delta A^*(\tau - 2z - x) A_0^*(\tau - 2z - x)) \quad \text{(B.25)}$$

By noting that in steady state

$$ibA_0 = A_0 - A_0|A_0|^2 I \quad \text{(B.26)}$$

$$I = \frac{1}{2}\int_0^{\infty} dz\, z^2 \int_0^{\infty} dx\, Q(x, z)$$

$$Q(x, z) = e^{-\hat{\nu}^3 z^2(2z/3+x)+i\hat{\alpha}z(z+x)}$$

$$\Rightarrow I = \frac{1}{2}\int_0^{\infty} dz\, \frac{1}{\hat{\nu}^3 z^2 - i\hat{\alpha}z} P(z)$$

$$P(z) = z^2 e^{-2\hat{\nu}^3 z^3/3 + i\hat{\alpha}z^2}$$

the linearised version of Eq B.25 becomes

$$\frac{d(\delta A A_0)}{d\tau} = \delta A A_0 - \frac{1}{2}A_0|A_0|^2 \int_0^{\infty} dz\, z^2 \int_0^{\infty} dx\, Q(x, z) \times (\delta A(\tau - z) + \delta A(\tau - z - x) + \delta A^*(\tau - 2z - x)) \quad \text{(B.27)}$$

This can be further simplified to

$$\frac{d\left(\delta A\right)}{d\tau}+ib\delta A=\delta A-\frac{1}{2}|A_0|^2\int_0^\infty dz\,z^2\int_0^\infty dx\,Q\left(x,z\right)\times \\ \left(\delta A\left(\tau-z\right)+\delta A\left(\tau-z-x\right)+\delta A^*\left(\tau-2z-x\right)\right) \quad \text{(B.28)}$$

Now let $\delta A=C\exp\left(\lambda\tau\right)+D\exp\left(\lambda^*\tau\right)$ in Eq B.28 to give

$$e^{\lambda\tau}\left\{\lambda C+ibC-C+\frac{1}{2}|A_0|^2\int_0^\infty dz\,z^2\int_0^\infty dx\,Q\left(x,z\right)\left[Ce^{-\lambda(z+x)}+Ce^{-\lambda z}+D^*e^{-\lambda(2z+x)}\right]\right\}+ \\ e^{\lambda^*\tau}\left\{\lambda^* D+ibD-D+\frac{1}{2}|A_0|^2\int_0^\infty dz\,z^2\int_0^\infty dx\,Q\left(x,z\right)\left[De^{-\lambda^*(z+x)}+De^{-\lambda^* z}+C^*e^{-\lambda^*(2z+x)}\right]\right\} \\ =0 \quad \text{(B.29)}$$

In order to solve this equation for long times we must insist that the bracket terms be equal to zero separately. The second bracket yields

$$D^*=\frac{-C\frac{1}{2}|A_0|^2\int_0^\infty dz\,z^2\int_0^\infty dx\,Q^*\left(x,z\right)e^{-\lambda(2z+x)}}{\lambda-ib-1+\frac{1}{2}|A_0|^2\int_0^\infty dz\,z^2\int_0^\infty dx\,Q^*\left(x,z\right)\left[e^{-\lambda(z+x)}+e^{-\lambda z}\right]} \quad \text{(B.30)}$$

which is turn leads to the dispersion relation for λ

$$0=\left\{\lambda+ib-1+\frac{|A_0|^2}{2}\int_0^\infty dz\,z^2\int_0^\infty dx\,Q\left(x,z\right)\left[e^{-\lambda(z+x)}+e^{-\lambda z}\right]\right\}\times \\ \left\{\lambda-ib-1+\frac{|A_0|^2}{2}\int_0^\infty dz\,z^2\int_0^\infty dx\,Q^*\left(x,z\right)\left[e^{-\lambda(z+x)}+e^{-\lambda z}\right]\right\}- \\ \left\{\frac{|A_0|^2}{2}\int_0^\infty dz\,z^2\int_0^\infty dx\,Q\left(x,z\right)e^{-\lambda(2z+x)}\right\}\times\left\{\frac{|A_0|^2}{2}\int_0^\infty dz\,z^2\int_0^\infty dx\,Q^*\left(x,z\right)e^{-\lambda(2z+x)}\right\}. \quad \text{(B.31)}$$

The x integral can be explicitly performed to give

$$0 = \left\{ \lambda + ib - 1 + \frac{|A_0|^2}{2} \int_0^\infty dz\, P(z) \left[\frac{e^{-\lambda z}}{\hat{\nu}^3 z^2 - i\hat{\alpha}^2 z + \lambda} + \frac{e^{-\lambda z}}{\hat{\nu}^3 z^2 - i\hat{\alpha}^2 z} \right] \right\}$$
$$\times \left\{ \lambda - ib - 1 + \frac{|A_0|^2}{2} \int_0^\infty dz\, P^*(z) \left[\frac{e^{-\lambda z}}{\hat{\nu}^3 z^2 + i\hat{\alpha}^2 z + \lambda} + \frac{e^{-\lambda z}}{\hat{\nu}^3 z^2 + i\hat{\alpha}^2 z} \right] \right\}$$
$$- \left\{ \frac{|A_0|^2}{2} \int_0^\infty dz\, P(z) \frac{e^{-2\lambda z}}{\hat{\nu}^3 z^2 - i\hat{\alpha}^2 z + \lambda} \right\} \times \left\{ \frac{|A_0|^2}{2} \int_0^\infty dz\, P^*(z) \frac{e^{-2\lambda z}}{\hat{\nu}^3 z^2 + i\hat{\alpha}^2 z + \lambda} \right\}. \tag{B.32}$$

B.5 Steady state distribution function

For drag and diffusion the steady state distribution function is obtained by solving the following equations

$$-\hat{\alpha}^2 \frac{\partial \hat{f}_0}{\partial \hat{u}} - \hat{\nu}^3 \frac{\partial^2 \hat{f}_0}{\partial u^2} = |A_0|^2 \,\mathrm{Re}\left(\frac{\partial \hat{f}}{\partial \hat{u}} \right) \tag{B.33a}$$

$$i\hat{u}\hat{f} - \hat{\alpha}^2 \frac{\partial \hat{f}}{\partial \hat{u}} - \hat{\nu}^3 \frac{\partial^2 \hat{f}}{\partial \hat{u}^2} = \frac{1}{2}. \tag{B.33b}$$

$\hat{f}$ is obtained by transforming into Fourier space and is found to be

$$\hat{f}(\hat{u}) = \pi \int_{-\infty}^0 e^{2\pi i \hat{u} p - 4\pi^2 i p^2 \hat{\alpha}/2 + 8\pi^3 p^3 \hat{\nu}^3/3}\, dp \tag{B.34}$$

which can be simplified using $y = -2\pi\hat{\nu}p$ to give

$$\hat{f}(\hat{u}) = \frac{1}{2\hat{\nu}} \int_0^\infty e^{-iy(\hat{u}/\hat{\nu}) - iy^2\hat{\alpha}/2\hat{\nu}^2 - y^3/3}\, dy \tag{B.35}$$

The $\hat{f}_0$ equation can be integrated once to give

$$\frac{\hat{\alpha}}{\hat{\nu}^3}\hat{f}_0 + \frac{\partial \hat{f}_0}{\partial \hat{u}} = -\frac{|A_0|^2}{\hat{\nu}^3} \mathrm{Re}\left(\hat{f} \right) \tag{B.36}$$

Upon substituting $\hat{f}$, the $\hat{f}_0$ equation is solved using an integrating factor method to give

$$\hat{f}_0 = -\frac{|A_0|^2}{2\hat{\nu}^3}\mathrm{Re}\left(\int_0^\infty e^{-y^3/3-iy^2\hat{\alpha}/2\hat{\nu}^2}\left[\frac{e^{-iy\hat{u}/\hat{\nu}}}{\hat{\alpha}/\hat{\nu}^2-iy}\right]dy\right)+ \frac{|A_0|^2}{2\hat{\nu}^3}e^{-\hat{\alpha}\hat{u}/\hat{\nu}^3}\mathrm{Re}\left(\int_0^\infty e^{-y^3/3-iy^2\hat{\alpha}/2\hat{\nu}^2}\left[\frac{1}{\hat{\alpha}/\hat{\nu}^2-iy}\right]dy\right) \quad \text{(B.37)}$$

This solution decays to zero at large positive u, but blows up at negative u. In order to satisfy the boundary conditions at infinity one can simplify subtract an exponential term (which is a solution to the homogeneous equation) to eliminate the exponential term. Upon doing this the final result for $\hat{f}_0$ takes the following form:

$$\hat{f}_0 = -\frac{|A_0|^2}{2\hat{\nu}^3}\mathrm{Re}\left\{\int_0^\infty e^{-y^3/3-iy^2\hat{\alpha}^2/2\hat{\nu}^2}\left[\frac{e^{-iy\hat{u}/\hat{\nu}}}{\hat{\alpha}^2/\hat{\nu}^2-iy}\right]dy\right\} \quad \text{(B.38)}$$

B.6 Drag vs. diffusion in toroidal geometry

Consider then temporal evolution of an energetic particle beam distribution function, $F(v_x, v_y, v_z)$, due to the Coulomb collisions with a thermal plasma species. An axial symmetry of the distribution function is assumed during the evolution:

$$F(v_x, v_y, v_z) = F(v, \theta) \quad \text{(B.39)}$$

where $v = \sqrt{v_\parallel^2 + v_\perp^2}$, $\theta = \tan^{-1}\left(v_\perp/v_\parallel\right)$, $v_\perp = \sqrt{v_x^2+v_y^2}$, $v_\parallel = v_z$. The Fokker-Planck equation for fast ion distribution function $F(v,\theta)$ with velocities $v_{Ti} \ll v \ll v_{Te}$ can be expressed in the form

$$\frac{\partial F}{\partial t} = \frac{V_0^3}{\tau v^2}\left\{\frac{\partial}{\partial v}\left[\frac{V_0^2 a(v)}{2v}\frac{\partial F}{\partial v} + b(v)F\right] + \frac{c(v)}{V_0}\cdot\frac{1}{\sin\theta}\frac{\partial}{\partial\theta}\left[\sin\theta\frac{\partial F}{\partial\theta}\right]\right\} - \nu F + pF \quad \text{(B.40)}$$

where

$$a\left(v\right)=\frac{T_e}{E_0}\left\{\tilde{Z}_2+\frac{4}{3\sqrt{\pi}}\frac{m_0}{m_e}\left(\frac{v}{v_{Te}}\right)^3\right\} \tag{B.41}$$

$$b\left(v\right)=\tilde{Z}_1+\frac{4}{3\sqrt{\pi}}\frac{m_0}{m_e}\left(\frac{v}{v_{Te}}\right)^3 \tag{B.42}$$

$$c\left(v\right)=Z_{\text{eff}}\frac{V_0}{2v}+\frac{2}{3\sqrt{\pi}}\frac{V_0}{v_{Te}}=Z_{\text{eff}}\frac{V_0}{2v}\left(1+\frac{4}{3\sqrt{\pi}}\frac{v}{v_{Te}}\right) \tag{B.43}$$

$$\tau=\frac{1}{\pi\sqrt{2}}\frac{E_0^{3/2}m_0^{1/2}}{Z_b^2e^4n_e\ln\Lambda}, \tag{B.44}$$

$\ln\Lambda$ is the Coulomb logarithm, m_0 is the mass of the fast ion species, V_0 and E_0 are convenient velocity and energy normalisations,

$$\tilde{Z}_1=\frac{m_0}{n_e}\sum_i\frac{Z_i^2n_i}{m_i} \tag{B.45}$$

$$\tilde{Z}_2=\frac{m_0}{n_eT_e}\sum_i\frac{Z_i^2n_iT_i}{m_i} \tag{B.46}$$

$$Z_{\text{eff}}=\left(1/n_e\right)\sum_i Z_i^2n_i \tag{B.47}$$

and two last terms in the right-hand-side of Eq B.40 represent a sink and source of energetic ions. The effect of the diffusion on the temporal evolution of $F\left(v,\theta\right)$ is given by two terms proportional to $a\left(v\right)$ and $c\left(v\right)$ in Eq B.40, while the effect of the drag is represented by the term proportional to $b\left(v\right)$. In establishing the distribution function on a global scale, the relative importance of the drag and diffusion depends on the ratio E_0/T_e. However, for assessing the relative importance of drag diffusion in the problem of a resonant interaction between, e.g. Toroidal Alfvén Eigenmodes (TAEs) and energetic ions, the drag and diffusion have to be compared locally in the narrow region of phase space close to the resonance.

Consider deeply passing NBI-produced ions with $\mu\equiv m_0v_\perp^2/2B=0$, with the resonance condition

$$\Omega\equiv\omega-n\frac{v_\parallel}{R}-l\frac{v_\parallel}{Rq\left(r\right)}=0 \tag{B.48}$$

and the expression for toroidal angular momentum

$$P_\phi=-\frac{e}{c}\psi\left(r\right)+m_0Rv_\parallel \tag{B.49}$$

where ψ is the poloidal flux function and $v_{\|} \approx v$. For the TAE frequency $\omega_{\mathrm{TAE}} = v_{\mathrm{A}}/2qR$ and $q \approx (m + 1/2)/n$, the landau resonance condition $v = v_{\mathrm{A}}$ is satisfied when $l = -m$, where m is the poloidal mode number. Hence

$$\frac{\partial \Omega}{\partial P_\phi} = \frac{\partial \Omega}{\partial r} \cdot \left(\frac{\partial P_\phi}{\partial r} \right)^{-1} \simeq m \frac{v}{Rq(r)} \cdot \frac{dq\,(r)}{dr} \cdot \frac{c}{eB_0 r} = \frac{m}{r} S \frac{vc}{eB_0 r R} \tag{B.50}$$

where $S = (r/q)\,(dq/dr)$ is the magnetic shear. The projection of the collision operators onto the P_ϕ direction can then be expressed as

$$\left\langle \frac{\partial P_\phi}{\partial \mathbf{v}} \cdot \mathbf{D} \cdot \frac{\partial P_\phi}{\partial \mathbf{v}} \right\rangle \sim \frac{V_0^5}{v^3} \frac{1}{\tau} (m_0 R)^2 a(v) + V_0^2 \frac{1}{\tau} (m_0 R \theta_b)^2 c(v) \tag{B.51}$$

and

$$\left\langle \frac{\partial P_\phi}{\partial \mathbf{v}} \cdot \mathbf{b} \right\rangle \sim \frac{b(v)}{\tau} \frac{V_0^3}{v^2} \frac{\partial P_\phi}{\partial v_{\|}} = \frac{b(v)}{\tau} \frac{V_0^3}{v^2} m_0 R. \tag{B.52}$$

Upon substitution into

$$\frac{(\Delta\Omega_{\mathrm{Diff}})^6}{(\Delta\Omega_{\mathrm{Drag}})^6} \approx \left\langle \frac{\partial P_\phi}{\partial \mathbf{v}} \cdot \mathbf{D} \cdot \frac{\partial P_\phi}{\partial \mathbf{v}} \right\rangle^2 \left(\frac{\partial \Omega}{\partial P_\phi} \right) \left\langle \frac{\partial P_\phi}{\partial \mathbf{v}} \cdot \mathbf{b} \right\rangle^{-3} \tag{B.53}$$

the diffusion vs. drag can be expressed as

$$\frac{(\Delta\Omega_{\mathrm{Diff}})^6}{(\Delta\Omega_{\mathrm{Drag}})^6} = mS\tau \frac{m_0 c}{eB_0} \frac{v^2}{r^2} \frac{\left[a(v) + (\theta_b)^2 c(v) \right]^2}{b(v)^3} \tag{B.54}$$

where $V_0 = v$. By substituting $v = v_{\mathrm{A}}$ and noting the typical smallness of T_e compared to E_{A} and v_{A} compared to v_{Te}, then one obtains

$$\frac{(\Delta\Omega_{\mathrm{Diff}})^6}{(\Delta\Omega_{\mathrm{Drag}})^6} \approx mS\tau \frac{c}{eB_0} \frac{E_{\mathrm{A}}}{r^2} \frac{\theta_b^4}{2} \frac{27}{64} \left(\frac{\pi m_b}{m_e} \right)^{3/2} \left(\frac{T_e}{E_{\mathrm{A}}} \right)^{9/2} \tag{B.55}$$

Bibliography

[1] J.Wesson, *Tokamaks*, Oxford Science Publications (2004).

[2] F. Troyon, R. Gruber, H. Saurenmann, S. Semenzato, and S. Succi, *MHD-Limits To Plasma Confinement*, Plasma Physics and Controlled Fusion **26**, 209 (1984).

[3] Y. K. M. Peng and D. J. Strickler, *Features of spherical torus plasmas*, Nuclear Fusion **26**, 769 (1986).

[4] M. Gryaznevich, R. Akers, P. G. Carolan, N. J. Conway, D. Gates, A. R. Field, T. C. Hender, I. Jenkins, R. Martin, M. P. S. Nightingale, C. Ribeiro, D. C. Robinson, A. Sykes, M. Tournianski, M. Valovic, and M. J. Walsh, *Achievement of Record β in the START Spherical Tokamak*, Physical Review Letters **80**, 3972 (1998).

[5] A. Sykes, R. Akers, L. Appel, E. Arends, P. Carolan, N. Conway, G. Counsell, G. Cunningham, A. Dnestrovskij, Y. Dnestrovskij, A. Field, S. Fielding, M. Gryaznevich, S. Korsholm, E. Laird, R. Martin, M. Nightingale, C. Roach, M. Tournianski, M. Walsh, C. Warrick, H. Wilson, S. You, M. Team, and N. Team, *First results from MAST*, Nuclear Fusion **41**, 1423 (2001).

[6] M. O. et. al., *Overview of the initial NSTX experimental results*, Nuclear Fusion **41**, 1435 (2001).

[7] H. R. Wilson, G. Voss, J.-W. Ahn, R. J. Akers, L. Appel, A. Bond, A. Cairns, J. P. Christiansen, G. Counsell, A. Dnestrovskij, M. Hole, A. Kirk, P. K. C. N. Lashmore-Davies, K. G. McClements, M. OBrien, and S. Tsaun, *Integrated*

plasma physics modelling for the Culham steady state spherical tokamak fusion power plant, Nuclear Fusion **44**, 917 (2004).

[8] W. Morris, R. J. Akers, G. Counsell, T. C. Hender, B. Lloyd, A. Sykes, G. M. Voss, and H. R. Wilson, *Spherical tokamaks: present status and role in the development of fusion power*, Venice (2004).

[9] W. W. Heidbrink and G. J. Sadler, *The behaviour of fast ions in tokamak experiments*, Nuclear Fusion **34**, 535 (1994).

[10] B. Lloyd, *Overview of recent experimental results on MAST*, Nuclear Fusion **43**, 1665 (2003).

[11] E. D. Fredrickson, *Wave driven fast ion loss in the National Spherical Torus Experiment*, Physics of Plasmas **10**, 2852 (2003).

[12] E. D. Fredrickson, N. N. Gorelenkov, and J. Menard, *Phenomenology of compressional Alfvén eigenmodes*, Physics of Plasmas **11**, 3653 (2004).

[13] T. Intrator, M. Vukovic, A. Elfimov, P. H. Probert, and G. Winz, *Discrete spectrum of Alfvén ionion hybrid waves*, Physics of Plasmas **3**, 1054 (1996).

[14] S. E. Sharapov, B. Alper, J. Fessey, N. C. Hawkes, N. P. Young, R. Nazikian, G. J. Kramer, D. N. Borba, S. Hacquin, E. De La Luna, S. D. Pinches, J. Rapp, D. Testa, and J.-E. Contributors, *Monitoring Alfvén Cascades with Interferometry on the JET Tokamak*, Physical Reveiew Letters **93**, 165001 (2004).

[15] H. Smith, T. Fülöp, M. Lisak, and D. Anderson, *Localization of compressional Alfvén eigenmodes in spherical tori*, Physics of Plasmas **10**, 1437 (2003).

[16] M. K. Lilley and S. E. Sharapov, *Compressional Alfvén and ion-ion hybrid modes in the deuterium-tritium plasma of a spherical tokamak power plant*, Physics of Plasmas **14**, 082501 (2007).

[17] W. Gekelman, H. Pfister, Z. Lucky, J. Bamber, D. Leneman, and J. Maggs, *Design, construction, and properties of the large plasma research device-The LAPD at UCLA*, Review of Scientific Instruments **62**, 2875 (1991).

[18] L. C. Appel, R. J. Akers, and R. M. T. Pinfold, *Observation of CAEs on MAST*, Vol. 28G, pg. P–4.198 (2004).

[19] M. Gryaznevich, S. Sharapov, M. Lilley, S. Pinches, A. Field, D. Howell, D. Keeling, R. Martin, H. Meyer, H. Smith, R. Vann, P. Denner, E. Verwichte, and the MAST Team, *Recent experiments on Alfvén eigenmodes in MAST*, Nuclear Fusion **48**, 084003 (2008).

[20] V. D. Shafranov, *Electromagnetic waves in a plasma*, Reviews of Plasma Physics **3**, 1 (1967).

[21] M. K. Lilley, S. E. Sharapov, H. M. S. R. J. Akers, D. McCune, and T. M. team, *Modelling of beam-driven high frequency Alfvén eigenmodes in MAST*, Vol. 32, pg. P–1.057, Hersonissos, Greace (June 2008).

[22] S. D. Pinches, H. L. Berk, M. P. Gryaznevich, S. E. Sharapov, and J.-E. Contributors, *Spectroscopic determination of the internal amplitude of frequency sweeping TAE*, Plasma Physics and Controlled Fusion **46**, S47 (2004).

[23] A. Fasoli, B. N. Breizman, D. Borba, R. F. Heeter, M. S. Pekker, and S. E. Sharapov, *Nonlinear Splitting of Fast Particle Driven Waves in a Plasma: Observation and Theory*, Physical Review Letters **81**, 5564 (1998).

[24] R. F. Heeter, A. F. Fasoli, and S. E. Sharapov, *Chaotic Regime of Alfvén Eigenmode Wave-Particle Interaction*, Physical Review Letters **85**, 3177 (2000).

[25] H. L. Berk, B. N. Breizmadn, and M. S. Pekker, *Nonlinear Dynamics of a Driven Mode near Marginal Stability*, Physical Review Letters **76**, 1256 (1996).

[26] B. N. Breizman, H. L. Berk, and M. S. Pekker, *Critical nonlinear phenomena for kinetic instabilities near threshold*, Physics of Plasmas **4**, 1559 (1997).

[27] A. I. Akhiezer, I. A. Akhiezer, R. V. Polovin, A. G. Sitenko, and K. N. Stepanov, *Plasma Electrodynamics Volume 1: Linear Theory*, Pergamon Press (1975), pages 253,212.

[28] T. H. Stix, *Waves in plasmas*, American Institute of Physics (1992).

[29] J. P. Freidburg, *Ideal magnetohydrodynamic theory of magnetic fusion systems*, Reviews of Modern Physics **54**, 801 (1982).

[30] J. P. Goedbloed, *Spectrum of ideal magnetohydrodynamics of axisymmetric systems*, Physics of Fluids **18**, 1258 (1975).

[31] S. J. Buchsbaum, *Resonance in a Plasma with Two Ion Species*, Physics of Fluids **3**, 418 (1960).

[32] V. D. Yegorenkov and K. N. Stepanov, *Alfvén and fast magnetosonic wave excitation by high energy ion beam in tokamak plasma*, EPS 1898, Venice, Italy (1989), Volume 3, page 1207.

[33] M. V. Gorelenkova and N. N. Gorelenkov, *Magnetosonic eigenmodes near the magnetic field well in a spherical torus*, Physics of Plasmas **5**, 4104 (1998).

[34] L. D. Landau and E. M. Lifshitz, *Quantum Mechanics (Non-relativistic Theory)*, Elsevier (2005).

[35] S. C. Hsu, M. Artun, and S. C. Cowley, *Calculation and interpretation of analytic high-beta poloidal equilibria in finite aspect ratio tokamaks*, Physics of Plasmas **3**, 266 (1996).

[36] See AIP Document No. PAPS PHPAEN-04-3667-29 for 29 pages of UKAEA Government Division Report UKAEA FUS 271, SCENE - simulation of self-consistent equilibria with neoclassical effects, by H. R. Wilson.

[37] D. G. Swanson, *Mode Conversion and Tunnelling at the Two-Ion Hybrid Resonance*, Physical Review Letters **36**, 316 (1976).

[38] I. Monakhov, A. Bcoulet, D. Fraboulet, and F. Nguyen, *One-dimensional full wave treatment of mode conversion process at the ion-ion hybrid resonance in a bounded tokamak plasma*, Physics of Plasmas **6**, 885 (1999).

[39] A. Fasoli, D. Testa, S. Sharapov, H. L. Berk, B. Breizman, A. Gondhalekar, R. F. Heeter, M. Mantsinen, and contributors to the EFDA-JET Workpro-

gramme, *MHD spectroscopy*, Plasma Physics and Controlled Fusion **44**, B159 (2002).

[40] G. W. Watson, W. W. Heidbrink, K. H. Burrell, and G. J. Kramer, *Plasma species mix diagnostic using ion-ion hybrid layer reflectometry*, Plasma Physics and Controlled Fusion **46**, 471 (2004).

[41] A. V. Timofeev, *Cyclotron oscillations of an equilibrium plasma*, Reviews of Plasma Physics **14**, 63 (1989).

[42] A. B. Mikhailovskii, *Thermonuclear drift instabilities*, Soviet Journal of Experimental and Theoretical Physics **41**, 890 (1975).

[43] Y. Zhang, W. W. Heidbrink, H. Boehmer, R. McWilliams, S. Vincena, T. A. Carter, W. Gekelman, D. Leneman, and P. Pribyl, *Observation of fast-ion Doppler-shifted cyclotron resonance with shear Alfvén waves*, Physics of Plasmas **15**, 102112 (2008).

[44] R. Cross, *An introduction to Alfvén waves*, Institute of Physics (1988).

[45] G. Duesling, Fusion Technology **3**, 1 (1967).

[46] C. E. Shannon, *Communication in the presence of noise*, Proc. Institute of Radio Engineers **37**, 10 (1949).

[47] M. K. Lilley, S. E. Sharapov, S. D. Pinches, M. Gryaznevich, and T. M. team, *Modelling of high frequency Alfvén eigenmodes in MAST and in a spherical tokamak power plant*, Vol. P-6, Kloster Seeon, Germany (October 2007).

[48] A. V. Timofeev and V. I. Pistunovich, *Cyclotron instabilities in an anisotropic plasma*, Reviews of Plasma Physics **5**, 401 (1970).

[49] R. Z. Sagdeev and V. D. Shafranov, *On the instability of a plasma with an anisotropic distribution of velocities in a magnetic field*, Soviet Physics JETP **12**, 130 (1961).

[50] H. L. Berk, B. N. Breizman, and Y. Haunchun, *Finite orbit energetic particle linear response to toroidal Alfvén eigenmodes*, Physics Letters A **162**, 475 (2003).

[51] R. Budny, M. Bell, H. Biglari, M. Bitter, C. Bush, C. Cheng, E. Fredrickson, B. Grek, K. Hill, H. Hsuan, A. Janos, D. Jassby, D. Johnson, L. Johnson, B. LeBlanc, D. McCune, D. Mikkelsen, H. Park, A. Ramsey, S. Sabbagh, S. Scott, J. Schivell, J. Strachan, B. Stratton, E. Synakowski, G. Taylor, M. Zarnstorff, and S. Zweben, *Simulations of deuterium-tritium experiments in TFTR*, Nuclear Fusion **32**, 429 (1992).

[52] N. Gorelenkov, C. Cheng, E. Fredrickson, E. Belova, D. Gates, S. Kaye, G. Kramer, R. Nazikian, and R. White, *Compressional Alfvén eigenmode instability in NSTX*, Nuclear Fusion **42**, 977 (2002).

[53] B. Coppi, *High-energy components an collective modes in thermonuclear plasmas*, Physics of Fluids **12**, 4060 (1986).

[54] D. G. Swanson, *Plasma Waves, Second Edition*, Institute of Physics (2003).

[55] I. P. E. G. on Energetic Particles, Heating, C. Drive, and I. P. B. Editors, *Chapter 5: Physics of energetic ions*, Nuclear Fusion **39**, 2471 (1999).

[56] P. L. Bhatnager, E. P. Gross, and M. Krook, *A Model for Collision Processes in Gases. I. Small Amplitude Processes in Charged and Neutral One-Component Systems*, Physical Review **94**, 511 (1954).

[57] L. Spitzer, *The physics of fully ionized gases*, New York (1962).

[58] D. V. Sivukhin, *Coulomb collisions in a fully ionized plasma*, Reviews of Plasma Physics **4**, 93 (1966).

[59] S. Chandrasekar, *Stochastic problems in physics and astronomy*, Reviews of modern physics **15** (1943).

[60] H. L. Berk and et.al, *Spontaneous hole-clump pair creation in weakly unstable plasmas*, Physics Letters A **234**, 213 (1997).

[61] H. L. Berk, B. N. Breizman, and H. Ye, *Scenarios for the nonlinear evolution of alpha-particle-induced Alfvén wave instability*, Physical Review Letters **68**, 3563 (1992).

[62] E. Fredrickson, N. Gorelenkov, R. Bell, J. Menard, A. Roquemore, S. Kubota, N. Crocker, and W. Peebles, *Fast ion loss in a 'sea-of-TAE'*, Nuclear Fusion **46**, S926 (2006).

[63] K. L. Wong, R. J. Fonck, S. F. Paul, D. R. Roberts, E. D. Fredrickson, R. Nazikian, H. K. Park, M. Bell, N. L. Bretz, R. Budny, S. Cohen, G. W. Hammett, F. C. Jobes, D. M. Meade, S. S. Medley, D. Mueller, Y. Nagayama, D. K. Owens, and E. J. Synakowski, *Excitation of toroidal Alfvén eigenmodes in TFTR*, Physical Review Letters **66**, 1874 (1991).

[64] W. W. Heidbrink, E. J. Strait, E. Doyle, G. Sager, and R. T. Sinder, *An investigation of beam driven Alfvén instabilities in the DII-D tokamak*, Nuclear Fusion **31**, 1635 (1991).

[65] K. Shinohara, Y. Kusama, M. Takechi, A. Morioka, M. Ishikawa, N. Oyama, K. Tobita, T. Ozeki, S. Takeji, S. Moriyama, T. Fujita, T. Oikawa, T. Suzuki, T. Nishitani, T. Kondoh, S. Lee, M. Kuriyama, J.-. Team, G. Kramer, N. Gorelenkov, R. Nazikian, C. Cheng, G. Fu, and A. Fukuyama, *Alfvén eigenmodes driven by Alfvénic beam ions in JT-60U*, Nuclear Fusion **41**, 603 (2001).

[66] K. L. Wong, J. R. Wilson, Z. Y. Chang, G. Y. Fu, E. Fredrickson, G. W. Hammett, C. Bush, C. K. Phillips, J. Snipes, and G. Taylor, *Expansion of parameter space for toroidal Alfvén eigenmode experiments in TFTR*, Plasma Physics and Controlled Fusion **36**, 879 (1994).

[67] M. Saigusa, H. Kimura, S. Moriyama, Y. Neyatani, T. Fujii, Y. Koide, T. Kondoh, M. Sato, M. Nemoto, and Y. Kamada, *Investigation of high-n TAE modes excited by minority-ion cyclotron heating in JT-60U*, Plasma Physics and Controlled Fusion **37**, 295 (1995).

[68] S. Bernabei, R. Budny, E. Fredrickson, N. Gorelenkov, J. Hosea, C. Phillips, R. White, J. Wilson, C. Petty, R. Pinsker, R. Harvey, and A. Smirnov, *The combined effect of EPMs and TAEs on energetic ion confinement and sawtooth stabilization*, Nuclear Fusion **41**, 513 (2001).

[69] J. A. Snipes, N. Basse, C. Boswell, E. Edlund, A. Fasoli, N. N. Gorelenkov, R. S. Granetz, L. Lin, Y. Lin, R. Parker, M. Porkolab, J. Sears, S. Sharapov, V. Tang, and S. Wukitch, *Active and fast particle driven Alfvén eigenmodes in Alcator C-Mod*, Physics of Plasmas **12**, 056102 (2005).

[70] H. L. Berk, W. H. Jr., M. N. Rosenbluth, and P. H. Rutherford, *Microinstability theory of two-energy component toroidal systems*, Nuclear Fusion **15**, 819 (1975).

[71] T. H. Stix, *Fast wave heating of a two component plasma*, Nuclear Fusion **15**, 737 (1975).

[72] L. D. Landau, *On the vibrations of the electronic plasma*, Journal of Physics (USSR) **10** (1946).

[73] A. A. Vedenov, *Theory of a weakly turbulent plasma*, Reviews of plasma physics **3**, 229 (1967).

[74] R. F. Heeter, *Alfvén Eigenmode and Ion Bernstein Wave Studies for Controlling Fusion Alpha Particles*, Ph.D. Thesis, Princeton University (November 1999).

[75] L. D. Landau and E. M. Lifshitz, *Mechanics*, Elsevier (1976).

[76] A. I. Morozov and L. S. Solovev, *Motion of charged particles in electromagnetic fields*, Reviews of plasma physics **2**, 201 (1966).

[77] B. A. Trubnikov, *Particle interactions in a fully ionized plasma*, Reviews of plasma physics **1**, 105 (1965).